Colloidal architectures

Atom-like assembly of patchy particles

Swinkels, P.J.M.

Publication date
2022

Document Version
Final published version

Colloidal Architectures

Atom-like Assembly of Patchy Particles

P.J.M. Swinkels

Colloidal Architectures: Atom-like Assembly of Patchy Particles P.J.M. Swinkels

Colloidal Architectures

Atom-like Assembly of Patchy Particles

P.J.M. Swinkels

Colloidal Architectures
Atom-like Assembly of Patchy Particles

ACADEMISCH PROEFSCHRIFT

ter verkrijging van de graad van doctor
aan de Universiteit van Amsterdam
op gezag van de Rector Magnificus
prof. dr. K. I. J. Maex
en overstaan van een door het College voor Promoties ingestelde
commissie, in het openbaar te verdedigen in de Agnietenkapel
op vrijdag 8 juli 2022, te 10.00 uur

door

Petrus Johannes Maria Swinkels

geboren te Tilburg

Promotiecommissie:

Promotor:	prof. dr. P. Schall	Universiteit van Amsterdam
Copromotor:	dr. C.J.M. Coulais	Universiteit van Amsterdam
Overige leden:	dr. M. Jalaal	Universiteit van Amsterdam
	prof. dr. S. Woutersen	Universiteit van Amsterdam
	prof. dr. P.G. Bolhuis	Universiteit van Amsterdam
	prof. dr. ir. J. van der Gucht	Wageningen University & Research
	dr. D. Chakrabarti	University of Birmingham

Faculteit der Natuurwetenschappen, Wiskunde en Informatica

UNIVERSITEIT VAN AMSTERDAM

Het hier beschreven onderzoek is uitgevoerd binnen de groep van prof. dr. Peter Schall aan het Institute of Physics van de Universiteit van Amsterdam (gevestigd te Science Park 904, 1098 XH, Amsterdam). Het onderzoek is gefinancierd met steun van de Nederlandse Organisatie voor Wetenschappelijk Onderzoek (NWO), via een persoonlijke toelage (VICI) toegewezen aan prof. dr. Peter Schall.

ISBN: 978-94-6419-528-6

Cover design by Maaike van den Boogaard

Chapter images design by P.J.M. Swinkels (chapters 1, 2, 4, and 6), Laura Quarto (Chapter 3), and Peter Swinkels (chapter 5).

A digital copy of this thesis can be obtained via `dare.uva.nl`

The author can be reached at: `research@swnkls.nl`

It's still magic, even if you know how it's done.

- Terry Pratchett, A Hat Full of Sky

Contents

1 Introduction

> Defining colloids in the traditional way is a bit like defining puppies as young dogs; though technically accurate, it doesn't quite capture their appeal.
>
> *Vinothan N. Manoharan*
> Colloidal matter: Packing, geometry, and entropy [1]

1.1 Emergence

A common definition of a molecule is the following[2]:

> The smallest particle of a substance that retains all the properties of the substance and is composed of one or more atoms.

However, the physical properties of a material are almost always different from the physical properties of a single molecule - if we can even speak of physical properties in this context. The difference in properties between a material and its constituent molecules is an example of what we call *emergence*: an entity has properties different from (the sum of) its parts, the properties emerge only when parts interact in a larger collection. In this case: an assembly of molecules, like a crystal, shows behaviour that a single molecule does not directly hint at.

Emergence is not just an abstract idea, we can recognize the principle in action in our daily lives. Chess is a simple game which can be explained to an 8-year-old, yet its simple rules lead to a complex strategic game that has remained interesting for the past 1500 years. The intricate patterns formed by wind on a sand-dune are hard to predict if one only knows about sand and wind. Life in particular is full of emergent properties. The archetypical example of emergence is consciousness: it still puzzles us how electrochemical potentials along cell membranes can lead to sentience. There are many more examples of emergence in biology, and in the context of this thesis, proteins make for an excellent example.

Proteins have many biological functions, ranging from 'simple' catalytic activity (Figure 1.1a) to sophisticated tasks like causing muscles contractions or assembling large superstructures, like viruses (Figure 1.1b). Each protein has a unique complex structure: a protein is a long chain molecule that twists and folds in very specific ways, see for example Figure 1.1c. The chemical groups these folds expose are responsible for the behaviour of the protein; it may attract other proteins to form specific assemblies, such as in Figure 1.1b, or it may stabilize certain reaction intermediates, catalysing reactions (Figure 1.1a). When we zoom in, however, we see that all proteins are chemically very similar: a protein chain always consists of just twenty different building blocks (*amino acids*) combined and repeated in

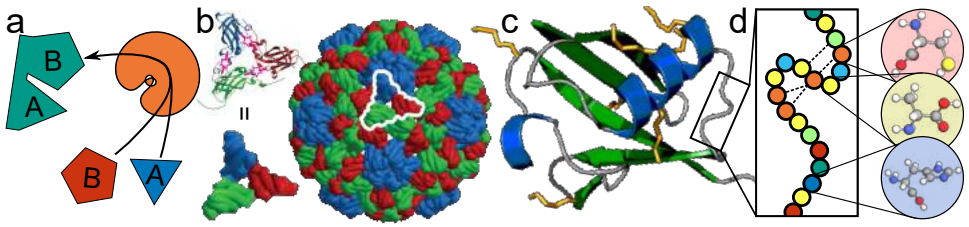

Figure 1.1 : Emergence. Proteins have a wide range of biological functions ranging from catalytic activity (a) to the assembly of complex structures, like viruses (b) [4]. Individual proteins are big chain-like molecule that twists and folds in specific ways to achieve a specific biological function (c). A protein is actually build up from a linear chain of amino acids (b), which interact with each other (shown as dotted lines), leading to the complicated protein structure.

different ways, Figure 1.1d. The order of these amino acids determines the folding of the protein, and in turn its properties. Even with a near-complete understanding of these building blocks, predicting the function of a protein based on its amino-acid sequence is extremely challenging. The complex interplay between building blocks is very hard to predict; a small change could make no difference, but could also have extremely far-reaching effects: for example, changing a single glutamic acid to a valine in the protein hemoglobin causes it to assemble in the wrong way, leading to sickle-cell disease [3].

Science is often reductionist, meaning that we try to explain a system by understanding its components. The well-known 'theory of everything' is the exponent of this view: intuitively, if we understand all the exact fundamental laws governing the smallest particles, we should understand everything that consist of them; everything. Unfortunately, in real life such a reductionist view will reveal almost nothing about the behaviour of everyday objects; in practice it is simply not very likely that we can ever use the theory to understand life and its chemical intricacies, let alone mundane phenomena such as bird flocking. The emergence of unexpected phenomena from well-understood building blocks is responsible for this disconnect, and its study is therefore necessary if we want to understand the world around us.

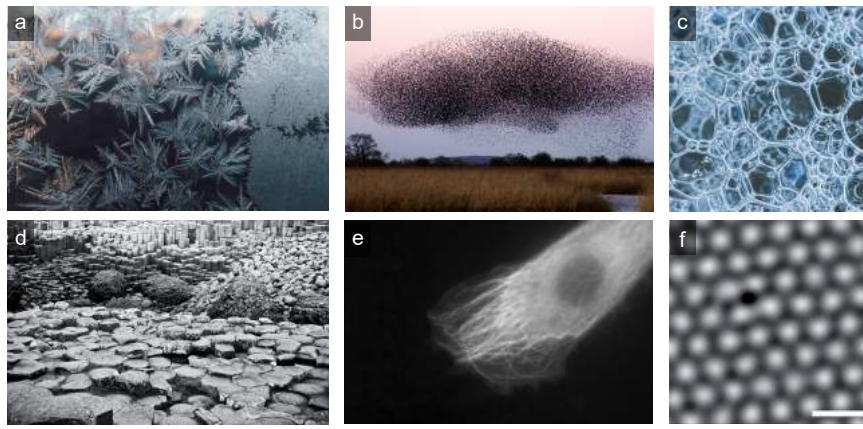

Figure 1.2 : Self-organizing systems are all around us. (a) Ice crystals forming on a window. (b) A flock of birds does not have a clear leader, but acts like a single entity. (c) Bubbles are formed as a result of relatively simple molecular interactions. (d) Cooling lava sometimes develops into hexagonal basalt columns as a result of crack propagation [5]. (e) Microtubule, the 'skeleton' of a cell, grow where they are needed, and break down where they are not [6]. (f) Graphene, carbon atoms ordered hexagonally [7].

1.2 Organization

A typical emergent process is *self-organization*, the formation of patterns and structure, without an external template or guiding force, see Figure 1.2. This universal tendency to self-organize is encountered in all domains of science, from astronomy - where stars cluster into galaxies - to ecology - where individuals form ecosystems. It is therefore of fundamental interest to understand what common principles underlie these phenomena. Furthermore, self-organization has the tendency to manifest in similar ways across seemingly unrelated systems: the shape of basalt columns in Figure 1.2d for example is extremely common in nature - hexagons are found in materials ranging from soap bubbles (Figure 1.2c) to graphene (Figure 1.2f).

A useful distinction can be made between *self-organization*, in which a system organizes under an energy input, and *self-assembly*, in which a system organizes in equilibrium: bird flocking (Figure 1.2b) is self-organization, while the formation of ice crystals (Figure 1.2a) is self-assembly. In this thesis, we deal with self-assembly. Self-assembly always has three basic ingredients: (i) building blocks, (ii) an interaction between those blocks, and (iii) a source of movement which can bring the

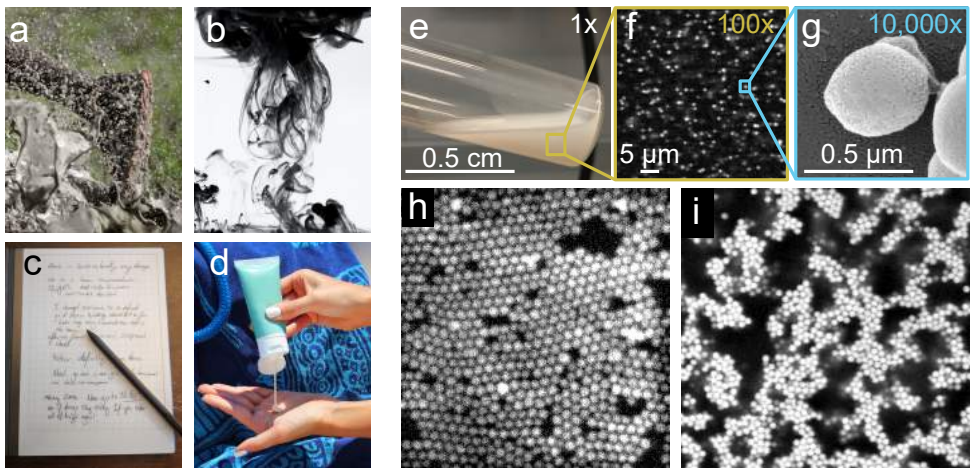

Figure 1.3 : Colloids. Mud (a), ink (b), my digital labjournal (c), and sunscreen (d), are just a few places where we find colloidal particles in our everyday lives. In the lab, colloids are typically stored dispersed in a solution which looks a boring milky white (e). Using fluorescence microscopy, we can distinguish individual particles floating in the suspension (f). SEM microscopy reveals the true nature of the colloidal particle: a homogenous polymer blob (g). Colloidal particles can assemble into colloidal crystals (h), colloidal gels (i) [8], and many other structures.

blocks together and makes them organize. In a self-assembled system, the interaction between building blocks is always local, meaning that there is no awareness of the larger structure; a building block is simply following its local interactions. The three ingredients can easily be identified in our examples: the protein in Figure 1.1c (i) consist of amino acids, which (ii) interact via inter- and intramolecular forces and (iii) move around via Brownian motion, the random jiggling of molecules.

1.3 Colloidal Particles

An intuitive, simple system for studying self-assembly and emergent properties are colloidal particles. Colloidal particles are small particles with a size between roughly 1 nm and 1 μm, suspended in a solvent, moving by Brownian motion*.

*This is a rather narrow, and arguably incorrect definition of a colloid, for a comprehensive discussion about what is and what is not a colloid, see for instance the field-defining works of Lyklema [9].

Examples of colloids in our day-to-day live include foodstuff (whipped cream, mayonnaise), soap, some gems (pearls, opals), and ink (including e-ink displays) among many other things (see Figure 1.3a-d).

Using colloidal particles as building blocks in self-assembly is compelling, because they are simple and easy to control: colloidal particles are typically spherical uniform blobs (see Figure 1.3e-g), without complex internal workings as opposed to molecules. On top of that, colloids can interact with each other via a myriad of different driving forces over which we can exert good control. Finally, colloids are small enough that thermal motion provides movement 'for free' due to the constant random wiggling of molecules.

Even the simplest colloidal particles can self-assemble into a fascinating range of structures. Depending on the system conditions, particles can assemble into highly ordered structures, like hexagonal crystals (Figure 1.3h), or into disordered assemblies like gels and glasses (Figure 1.3i). By making precise changes to the building blocks and their interactions, like adjusting attractive strength or size dispersity, we can influence the assembly of colloids. Furthermore, colloids are relatively straightforward to investigate experimentally due to their simple preparation and easy-to-vary properties like charge. On top of that, their size is convenient: colloidal particles are large enough to be visible under a regular optical microscope, and assemblies can easily be characterized by light scattering experiments.

Interestingly, many of the phases colloidal particles assemble into are reminiscent of atomic states of matter (gas, liquid, solid crystals, etc.) [9]. This may not be so surprising when we consider that the 3 components of self-assembly are actually quite similar in atomic and colloidal phases. Atoms, for all their complexity, often behave as simple uniform spheres, just like simple colloidal particles. Interactions between atoms and colloidal particles have different origins, but are of similar relative range and strength, and both atoms and colloids jiggle around due to thermal motion. This has earned colloidal particles the name of *big atoms* [10]. Although atoms are of course very different from colloidal particles, their collective properties are surprisingly similar. This is not a recent realization; the similarity in behaviour of atoms and colloids led to the experimental conformation of molecules in the first place in 1909 [11].

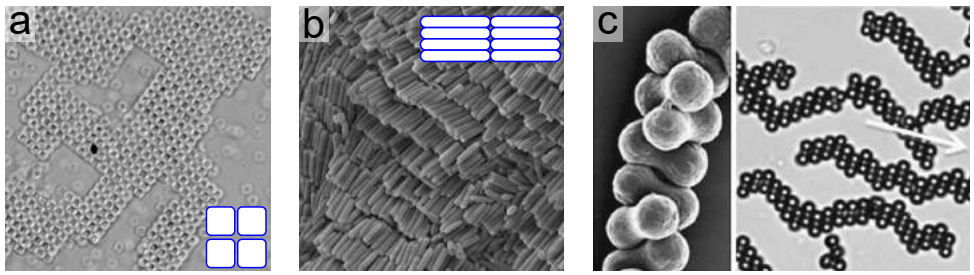

Figure 1.4 : The assembly of non-spherical colloids is not always intuitive. (a) Cubic colloids assembling into cubic crystals [12]. (b) Colloidal rods tend to align when they assemble, in this case forming a smectic phase [13]. (c) Dumbbell-shaped particles assemble into one-dimensional zigzagging chains [14].

1.3.1 Anisotropy

Although colloidal assembly of spherical particles is already intriguing, one cannot help but wonder: what happens in more complex systems? What kind of structures can be created if we deviate from uniform spheres? Apart from simple human curiosity, these questions have scientific relevance as well: modified building blocks can lead to new emergent material properties. Understanding the interplay between building block and the material they assemble into has intriguing prospects: one of the paradigms of soft matter is that the microstructure of a material controls its macroscopic properties. With absolute control over material microstructure, we could engineer interesting material properties that are hard to obtain in conventional bulk materials. Examples of such traits range from mechanical properties, such as a negative Poisson's ratio [15] and other properties sought after in the field of metamaterials [16], to opto-electronic properties, like a photonic band-gap [17].

What do we mean by more complexity? The most obvious change one can make to a particle is to go beyond a simple spherical shape: the behaviour of a perfectly symmetrical spherical particle is generally well understood, so studying the effect of different shapes is a natural step to take [18, 19]. For instance, cubic colloids (maybe unsurprisingly) tend to assemble into cubic crystals, as shown in Figure 1.4a, but can also assemble into a range of slightly shifted lattices, depending on the assembly conditions [12, 20]. Rod-like colloids display a rich phase behaviour not seen in spherical particles. Aside from the usual liquid and crystalline phases, liquid crystal phases such as the nematic phase, in which particles have no positional

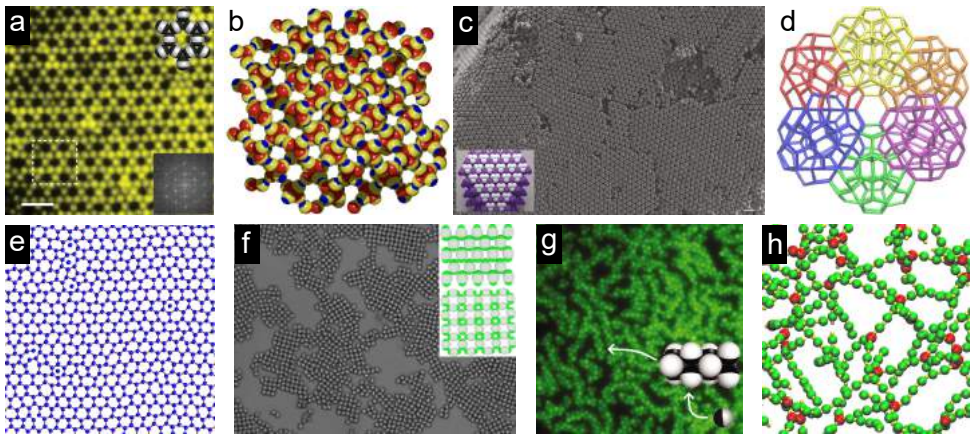

Figure 1.5 : Large colloidal superstructures. (a) The famous kagome lattice, a repeated star-like geometry formed by dipatch particles, where every patch is in contact with two other particles [22]. (b) A diamond lattice formed by tetrahedral particles, as predicted by numerical simulations [23]. (c) An experimentally realized diamond lattice, assembled from tetrahedral particles with strongly bulging patches [24]. (d) A model prediction of clathrates, buckyball-like structures formed by tetrahedral particles [25]. (e) A model prediction of the honeycomb lattice formed by trivalent particles confined to a monolayer [26]. (f) Dipatch particles assembled into square packing and open brick-wall structures [27]. (g) Worm-like structures composed of janus particles can form a gel-like morphology [28] (h) A prediction for an equilibrium gel network composed of dipatch (in green) and tetrapatch (in red) particles [29].

order but are all rotated in the same direction [21], and the smectic phase, in which rods form aligned layers (shown in Figure 1.4b) [13], are observed. These phases are highly relevant to technological applications, and are found in liquid-crystal displays (LCDs). More exotic particle shapes, like the magnetic dumbbells in Figure 1.4c, can assemble into complex structures which are not always easy to intuitively predict. At low density, the particles assemble into one-dimensional chains, which start interlocking if the density is increased, leading to a lattice consisting of ordered chains [14].

Another, more controlled way of introducing complexity to a colloidal system is to make use of inhomogeneous particles; instead of a single component, a particle is composed of two or more different materials. The most basic example of this is the so-called Janus particle, named after the two-faced Roman god of duality. Two halves of the particle consist of a different material, which react differently to

the environment and/or other particles, see Figure 1.6a, where half the particle is orange, and the other half is grey. With the improvement of synthetic methods in the past decade, even more sophisticated particles can be engineered, so-called *patchy particles*. Patchy particles have a surface with well-defined patches of a different material, see Figure 1.6b. The patches are typically designed to attract each other, and their placement is chosen such that a particle has limited valency and directional bonding, meaning that we control exactly where particles will attach and assemble. Essentially, patchy particles are microscopic lego-bricks: by controlling how two particles fit together, we aim to control the superstructure they assemble into, and thus engineer material properties.

1.3.2 Patchy Particle Assembly

Simulations and experiments of patchy particles have yielded a huge variety of interesting self-assembled structures and phases. Colloidal assemblies typically fall into one of two categories: periodic superstructures or finite assemblies. In this section I will highlight the importance of each category, and give a short overview of published work on these structures.

Periodic Superstructures

Large colloidal superstructures consist of many particles, typically, but not necessarily, with a certain repeating motif or long-range order. Non-patchy colloidal particles have been assembled into large superstructures for decades, initially mainly as a model system for atomic phases [9, 30, 31]. As the field matured, assemblies came to be regarded as more than just a model system: they are self-assembling materials with their own interesting mechanical [32, 33], electronic [34–36] and optical [37] emergent properties.

When the idea first developed to use patchy particles to further explore the engineering of colloidal materials, their preparation in the lab was not experimentally feasible [38, 39]. However, patchy particles are relatively easy to model *in silico*, so experimental limitations did not stop theorists from producing many models and simulations for a range of patchy particle models. Early examples of such predictions include the diamond lattice [39] and empty liquids [40]. It took years before improvements in synthetic production of patchy particles lead to the first example of an assembled patchy particle periodic superstructure: the kagome

lattice. The kagome lattice, shown in Figure 1.5a, consists of dipatch particles, where each patch binds two other patches, leading to the formation of a star-like pattern [22]. Although this structure is not of any particular practical use, it did demonstrate that patchy particles can be used for experimental assembly of large non-trivial superstructures; it was the first step on the path to controlled microscopic engineering of large superstructures using patchy particles.

Despite this success in generating a patchy-particle superstructure over a decade ago, other experimental examples remain rare; the reliable assembly into large superstructures remains very challenging. An illustrative example is the diamond lattice, formed by tetrahedral particles ordered into repeating 6-membered rings, see Figure 1.5b&c. Colloidal diamond is one of the earlier predictions for a possible phase built from tetrahedral particles* [39]. The lattice is of particular interest because it has a photonic band gap, which allows precise manipulation of light [41, 42]. Unfortunately, reaching this state experimentally remained impossible for a long time, mainly due to two problems: spherical tetrapatch particles have no intrinsic preference for staggered or eclipsed bonding conformation [24], and the formation of 5-membered rings is kinetically preferred and stabilized [25]. These 5-membered rings can then form energetically stable buckyball-like clathrates, see Figure 1.5d. Recently, these challenges have finally been overcome experimentally, 15 years after its theoretical description, by combining a geometrically controlled bonding valency with a specific shape, as shown in Figure 1.5c [24].

The field remains in a state where experimental results are highly sought after. Simulation results are often hard to confirm experimentally because they underestimate or ignore the importance of kinetic pathways toward predicted structures, or use particle designs that are experimentally not feasible. Although this is a known issue, and significant effort is expanded to take it into account, it remains challenging to translate results from simulations to experiment [25, 43, 44]. Despite these difficulties, simulations and the few experimental examples that currently exist in literature give us a glimpse of the microscopic architecture that surely will become more prevalent in the future of designing smart materials.

Two more examples of highly ordered periodic superstructures shall be briefly addressed here to highlight the rich morphological variation patchy particle structures can display. Figure 1.5e shows a honeycomb lattice, formed by trivalent

*Although one could make the argument that this is not so much a prediction as looking at the crystallization of carbon atoms.

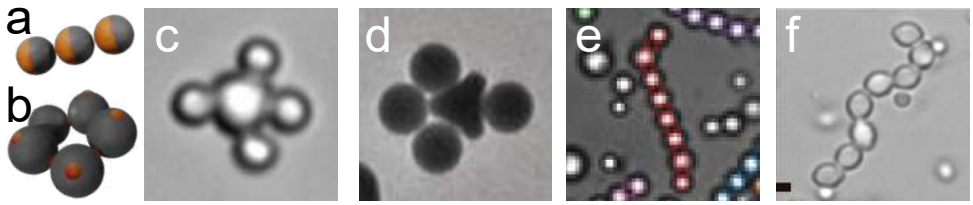

Figure 1.6 : Small colloidal assemblies. (a) Janus particles and (b) tetrahedral patchy particles are both examples of anisotropic colloids, where the orange and black are different materials. (c) A colloidal molecule, formed by a central tetrahedral particle with 4 smaller particles attached. The cluster mimics a molecule like CH_4 [50]. (d) A planar colloidal molecule consisting of a central trivalent particle and three smaller outer particles. In this case, particles are assembled through the use of dimples in the central particle [51]. (e) A 'polymer' chain of divalent colloidal particles [52]. (f) A chain of colloids [53].

particles confined to a plane, similar to how graphene is formed by trivalent carbon atoms. *Colloidal graphene* is expected to display some interesting properties which graphene also exhibits: a photonic and phononic bandgap [15, 45–47], and topologically protected states. Another example is shown in Figure 1.5f, where dipatch particles form two structurally distinct square phases. By changing the patch-to-bulk size ratio, the system can be tuned to assemble into a wide variety of different periodic structures [27]. This rich variation in structural morphology from simple di- and trivalent particles highlights once more the potential for complex microscopic architecture resulting from assembly of patchy particles.

Not all large superstructures are ordered or crystalline; some are fundamentally unordered, even in equilibrium. For instance, simple janus particles can be assembled into highly structured worms, Figure 1.5g. These worms themselves however, do not have a clear order with regard to each other, and assemble into a gel-like structure. An even more exciting example is the hub-and-spoke network we obtain by mixing di- and tetravalent particles. Simulations show the formation of central hubs of tetravalent particles connecting chains of divalent particles; a snapshot of such a network is shown in Figure 1.5h. A network formed by patchy particles is predicted to be a so-called *equilibrium gel* [48, 49], a state which is of fundamental interest to our understanding of gelling, a ubiquitous process in the natural world.

Finite Assemblies

Besides the more traditional large superstructures, there has been an increased interest in smaller finite-sized assemblies of colloids in the past decade. Colloidal clusters of isotropic particles are interesting because their limited size makes the self-assembly easier to study and understand quantitatively [54, 55]. Furthermore, these clusters can display exotic optical properties [56, 57].

Small clusters of patchy particles are well studied compared to large superstructures, because smaller assemblies are simply easier to control and understand. As we discussed, the assembly of patchy particles is not a trivial matter, so achieving directed self-assembly in small cluster is reason enough to celebrate [58–60]. That is not to say that these clusters are not useful: as isotropic particles can serve as a model for atoms, small colloidal assemblies can serve as a model for a molecule, and the study of so-called *colloidal molecules* has become a fashionable use of these clusters [61]. In a colloidal molecule, colloids act as big atoms, mimicking the bonding arrangements of their atomic counterparts, see Figure 1.6c&d for examples. Because colloids can be directly observed, their behaviour is much easier to study than those of atoms. For instance, studies into the reaction kinetics of colloidal molecules show interesting similarities with 'regular' atomic reactions [50]. Colloidal polymers, consisting of identical repeating particles (examples shown in Figure 1.6e&f), are another clear example. The growth and dynamics of such chains is surprisingly similar to that of atomic polymers [51, 62].

Finally, a strong motivation for the study of finite-sized particle assemblies is that these clusters are often the basic motifs of any larger superstructures that these particles could assemble into [63]. Much like molecules are studied because they are the smallest unit of the materials around us, it is appealing to study small colloidal assemblies as the building block for larger superstructures. An example is the structure shown in Figure 1.5f: the dipatch particles form colloidal polymers with specific geometries that are also found in the larger assembled superstructure [27].

1.4 Thesis Outlook

This thesis aims to experimentally address the self-assembly of patchy colloids. Although I treat a few specific cases of colloidal assembly here, this work should be seen in the larger context of understanding and controlling microscopic assembly.

Chapter 2 deals with the experimental methods and core concepts that are used in this thesis. I briefly discuss the properties and synthesis of the colloidal particles used in this thesis. I then quickly give a practical guide to the critical Casimir force, the driving force for colloidal assembly. Finally, I describe how we proceed from sample preparation to experiments and conclusions, and which techniques and analysis steps this involves.

In Chapter 3, we dive into the physics of small patchy particle assemblies in seriousness, looking at a small colloidal ring made up of five tetrahedral patchy particles. I discuss how these *colloidal cyclopentane* rings can undergo the same chemical transformations as their atomic counterparts. Transitions between chair and twist conformations in colloidal cyclopentane are observed directly, and we elucidate the interplay of bond bending strain and entropy in the molecular transition states and ring-opening reactions.

Chapter 4 explores *colloidal graphene*, the analogue of atomic graphene assembled using pseudo-trivalent patchy particles confined to a plane. Direct observation of the formation and healing of common defects, like grain boundaries and vacancies, grants us insight into what may occur during the growth process of atomic graphene, normally hidden due to the extreme conditions in which it takes place. These direct observations reveal that the origins of the most common defects lie in the early stages of graphene assembly, where pentagons are kinetically favoured over the equilibrium hexagons of the honeycomb lattice, subsequently stabilized during further growth.

In Chapter 5, we dive deeper into the system of pseudo-trivalent patchy particles confined to a plane and map the full phase diagram of the system. Apart from the colloidal graphene described in Chapter 4, we observe regions in the phase diagram where a triangular lattice and amorphous network are formed. We investigate these unexpected condensed phases, revealing their shared structural motifs. Combining results from model and experiment, we elucidate the energetics of the three condensed phases and construct the phase diagram of the system. This chapter illustrates the rich phase behaviour a relatively simple patchy particle system can display.

Finally, Chapter 6 treats an unordered patchy particle superstructure: networks constructed from a mixture of di- and pseudo-trivalent patchy particles. This network is a so-called equilibrium gel, and has some very counterintuitive properties: while the properties of a 'regular' colloidal gel strongly depend on the conditions of its formation, the history of an equilibrium network does not influence its even-

tual properties. On top of that, we can use a corrected Flory-Stockmayer theory to accurately describe and predict the behaviour of the system as a function of the normalized number of bonds.

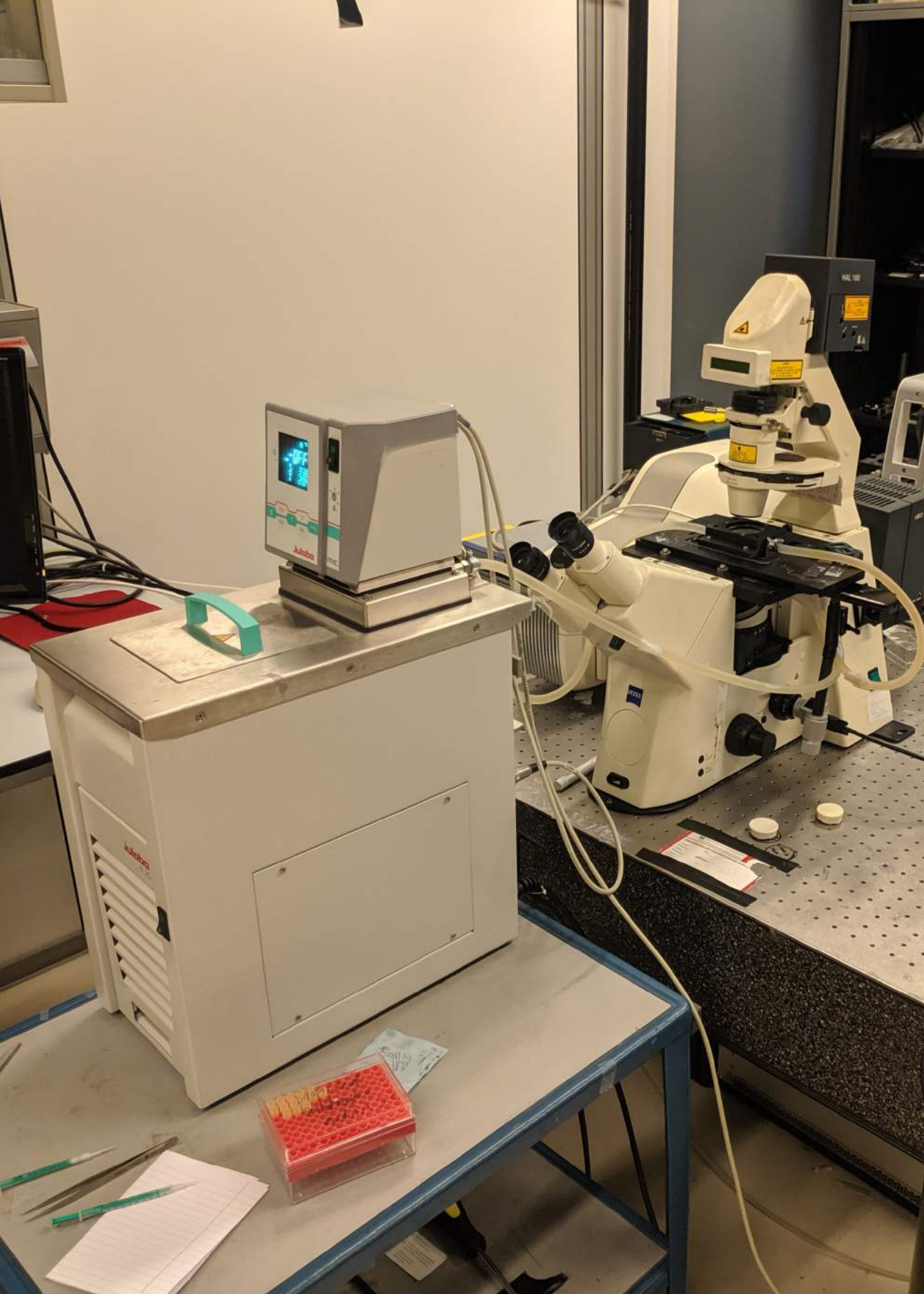
Julabo
HAL 100

2 Concepts and Methods

> When you got right down to it, humans were still just curious monkeys. They still had to poke everything they found with a stick to see what it did.
>
> *James S.A. Correy*
> Leviathan Wakes

In published articles, the details of experimental work tend to be swept under the rug somewhat, not because they are unimportant or trivial, but because experiments are, after all, a means to an end. Nonetheless, the experimental process has its own challenges, distinct from the physics we generally try to understand through them, and therefore deserves a closer look. There is a reason the results presented in this thesis are new, and it is not due to freely available low-hanging fruit in the field, nor the lack of imagination from colleagues: it is because the results are very challenging to obtain experimentally. In this chapter, I will try to convey what practical methods I have developed and applied in the past few years, with the sincere hope that it may help any successor(s).

2.1 Colloids

In this thesis, I explore the assembly of diverse structures assembled from simple di-, pseudo-tri-, and tetravalent patchy particles. Recent breakthroughs in particle synthesis have provided strategies to fabricate anisotropic particles, micrometer-size building blocks, which has been a challenge for a long time.

Regular isotropic colloids are often produced using dispersion polymerization [64]. Briefly, in this technique a polymerization reaction takes place in which the polymers are immiscible with the solvent, so that the produced polymers form small precipitates which can grow into colloids. One can vary the exact parameters (solvent, temperature, etc.), but the acting mechanism, the precipitation, will never yield anisotropic particles. Other methods of generating conventional colloids, like emulsion polymerization [65], or the reduction of salts [66], suffer from the same fundamental problem: the nucleation and growth mechanism of these reactions tend to result in spherical particles. Therefore, a fundamentally different synthesis route is needed. In the past decade or so, synthesis routes to increasingly complex patchy particles have become more commonplace. Of specific interest in this thesis is the particle synthesis developed in the group of Sacanna [67]. This method, which will be described in detail below, allows for the production of linear dipatch and tetrahedral tetrapatch particles with high specificity and monodispersity. The strategy is to cluster isotropic colloids, which will later form the patches of the particle. Not only the Sacanna-particles described in this thesis are based on this principle, but many successful patchy particle synthesis routes make use of a variation of this principle [58, 68–71], although different approaches are also viable [72–76].

2.1.1 Colloidal Synthesis

The patchy particles used in this thesis are synthesized via colloidal fusion [67] with a modified recipe. Negatively charged polystyrene particles are synthesized by seeded emulsion polymerization using potassium persulfate ($> 99.0\%$, Sigma-Aldrich) as initiator. After repeated seeded emulsion polymerization, negatively charged PS particles are resuspended into $12.5\ \mathrm{mM}\ \mathrm{NaCl}$ solution. Silicone emulsion droplets are made by hydrolysis and condensation of 3-(trimethoxysilyl) propyl methacrylate (TPM, 98%, Sigma-Aldrich) catalysed by ammonium hydroxide (28 wt.%, Sigma-Aldrich). The droplets are later fluorescently labelled with

3-aminopropyl trimethoxysilane coupled rhodamine-B isothiocyanate. Pluronic F108 triblock copolymer (average Mn 14 600, Sigma-Aldrich) is added into the silicone emulsion to a final concentration of 0.05 wt.% to further stabilize the droplets. The F108-TPM emulsion is gently washed by two cycles of centrifugation/resuspension to remove free F108 polymer in emulsion, and later resuspended into 12.5 mM NaCl solution. Tetrahedral colloidal clusters are made by mixing the prepared negatively charged PS particles and F108-TPM droplets at a number ratio around 100:1. To screen the negative charge on both particle surfaces and thus allow for polymer bridging between the two, 12.5 mM NaCl is necessary. These clusters are then separated from excess PS singlets by centrifugation in a glycerol/water mixture (approximately 22 wt.% glycerol). The purified clusters are resuspended into aqueous solution containing 0.05 wt.% F108 copolymer and 0.5 wt.% dodecyl-trimethylammonium bromide (DTAB, $\geq$ 98%, Sigma-Aldrich), to prevent aggregation, and to facilitate core-extrusion during colloidal fusion, respectively. Pure tetrahydrofuran is then added to the cluster suspension to reach a final concentration of 30% $V_{\mathrm{THF}}/V_{\mathrm{cluster}}$. The fusion is allowed to proceed for 3 minutes before being quenched by deionized water. The resulting patchy particles with liquid patches are then resuspended into deionized water, followed by its polymerization in a 80 °C oven for 2 hours. After polymerization, patchy particles typically undergo three centrifugation/resuspension cycles and are transferred back into deionized water for further experiments.

The diameter ratio TPM:PS determines whether a dipatch or tetrapatch particle is obtained - a ratio of 1:3 yields dipatch particles, a ratio of 1:2 yields tetrapatch particles. We have received several batches of di- and tetrapatch particles from the Sacanna group, synthesized by Zhe Gong, each with their own diameter, patch size, and degree of extrusion. The properties of these particles are determined using a variety of techniques (see below), and given in Table 2.1. Each chapter of this thesis makes use of one or more of these particle batches.

2.1.2 Characterization

Each particle batch is characterized carefully to determine the particle size, patch diameter, and other relevant particle properties. We use three different techniques to characterize particles: scanning electron microscopy (SEM), atomic force microscopy (AFM), and optical microscopy.

Table 2.1 : Particle stocks. Most important properties of patchy particle stocks used in this thesis. The patch diameter and patch radius are determined using scanning electron microscopy (SEM), the inter-particle distance is the distance between particles in an assembled structure and is determined using optical microscopy. Values are given with their standard deviations.

Label	Type	Particle diameter (μm)	Patch radius (μm)	Inter-particle distance (μm)
A	Tetrapatch	3.7 ± 0.2	0.54 ± 0.05	3.80 ± 0.11
B	Dipatch	3.2 ± 0.1	0.58 ± 0.05	
C	Tetrapatch	1.8 ± 0.07	0.51 ± 0.05	2.00 ± 0.05

For the SEM measurements, we dilute a particle stock in water, and dry the suspension on a silica surface. Figure 2.1b shows a typical SEM image of tetrapatch particles. From SEM, we can determine the particle diameter and the patch radius given in Table 2.1.

AFM can be used for a more accurate estimation of the patch topology. AFM samples are prepared by drying a particle dispersion on a glass microscopy slide. Particles which have a patch oriented upwards are selected for AFM scans. A resulting scan with a clearly visible patch is shown in Figure 2.1d. By taking a cut through the patch, we obtain the line scan as shown in Figure 2.1e, which yields the particle and patch radius by simple fitting of the respective curvatures, as well as the patch height and patch radius of curvature.

Finally, effective particle dimensions can be determined directly from optical microscopy images of assembled particles. In an assembled structure, the inter-particle distances of bonded patchy particles should correspond to the effective particle sizes, consisting of the particle diameter, patch height and interaction range. To illustrate this, I perform the analysis for particles of batch A (Table 2.1). Very good consistency is observed between this measure and AFM/SEM measurements: the distribution of particle-particle distances of assembled particles of batch A is shown in Figure 2.1f. The mean distance between particle centres is $3.8\,\mu\text{m}$ reflecting the SEM-determined particle size (particle diameter $\sigma = 3.7\,\mu\text{m}$) plus twice the AFM-determined patch height ($2 \times 48\,\text{nm} = 96\,\text{nm}$), plus the (short) critical Casimir interaction range, while the standard deviation of $\sigma = 0.11\,\mu\text{m}$ reflects the estimated particle size variation ($100\,\text{nm}$) and twice the variation of the patch height ($2 \times 5\,\text{nm} = 10\,\text{nm}$). Although this method

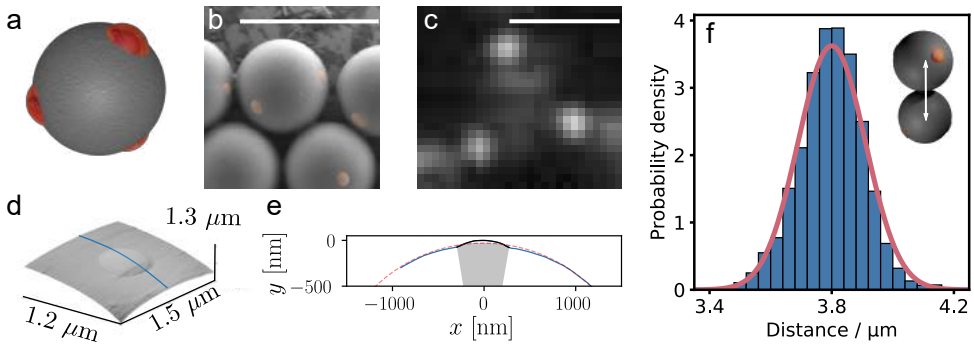

Figure 2.1 : Characterization of patchy particles. (a) Schematic of tetrapatch particle. (b) Scanning electron microscopy image of a tetrahedral patchy particle (batch A in Table 2.1). The patches are given a false colour. The scalebar indicates 5 μm. (c) Confocal image of a tetrahedral patchy particle (batch C in Table 2.1). The scalebar indicates 2 μm. (d) Atomic force microscopy image of a tetrapatch particle (batch A in Table 2.1). (e) 2D cuttrough of the AFM image along the blue line in (d). The blue line shows the bulk, the black line the patch. The dashed red line is the projected particle diameter σ. Patch diameter, patch height, and patch radius of curvature can be determined from this image. (f) Distribution of inter-particle distances in a structure assembled of particles from batch A in Table 2.1 (in blue). A normal distribution is fitted to the data (red line), resulting in an average inter-particle distance of 3.80 μm with a standard deviation of 0.11 μm.

is rather indirect, it is arguably preferable to AFM or SEM because it measures the relevant parameters *in situ*. Parameters can be directly related to experiments, while in the case of SEM and AFM measurements, it is not always obvious how the determined parameters correspond to the particles dispersed in solution.

2.2 Self-assembly: The Critical Casimir Force

2.2.1 Assembling Particles

Now that we have discussed the building blocks to assemble, let us discuss the force bringing and keeping assemblies together. Over the years, different methods for colloidal assembly have been developed. At the time of writing, the popular ways of enticing assembly in the lab are DNA-linkers [77], depletion attraction [78], or the use of an external force, like a magnetic or electronic field [79]. However,

in our lab, we are specialized in the less common *critical Casimir force* (CCF) for colloidal assembly [80]. The critical Casimir force is a specific, tunable interaction that arises in binary solvents close to their critical temperature. It results from the confinement of solvent fluctuations between two immersed surfaces, and can be precisely tuned by varying temperature and absorption preference of the confining surfaces.

Casimir versus the Rest

What does the critical Casimir force offer us that other, more conventional forces for assembly lack? Firstly, the critical Casimir effect is universal: if a binary solvent with an accessible critical point is chosen, interaction between particles will always occur, meaning particles do not need to be made of a specific material to work (like when using magnetic particles). A specific surface is also not necessary; no surface treatment needs to be performed for particles to become attractive (like when using DNA linkers). Secondly, the critical Casimir force can easily be tuned in strength by varying the temperature, giving excellent control over the interaction strength between particles. Finally, by controlling the ratio of the solvents in the binary solvent, the critical Casimir force can be made selective for a specific boundary condition set by surface chemistry. This final point is of critical importance for patch-patch assembly: we can make patches attract only other patches and ignore the bulk, simply by making sure the patch and the bulk have a different affinity for the solvent components.

As a drawback of using the critical Casimir force, we are usually strongly tied to the solvent composition; even small changes can severely influence the behaviour of the system. From a practical perspective, there are experimental designs in which changing the density and refractive index of the solvent is useful or even necessary, specifically when a density match or index match of the solvent to the particles is required. A more application-based problem is the toxicity of the required solvents: the binary solvents typically used to induce critical Casimir forces are all somewhat toxic (they are typically pyridine-derivatives, see below), which excludes practical applications in a larger or commercial setting that requires direct human interaction, like biomedical applications.

2.2.2 Critical Casimir: Coercing Criticality

In this thesis, we use critical Casimir interactions to assemble patchy colloidal particles. An exhaustive theoretical treatment of the critical Casimir effect is available in literature [81, 82], and only a brief introduction into the basic concepts will be provided here, which should give the reader a solid background to navigate the remainder of this thesis.

The critical Casimir force (CCF) arises in a so called 'binary solvent', a solvent consisting of two components. A binary solvent will demix into two separate phases when the demixing line is crossed, see the schematic in Figure 2.2a. The critical point on this phase diagram, which is situated at a critical temperature T_c and a critical composition C_c, plays a crucial role in the critical Casimir force. When the system approaches the critical point from the one-phase region, phase separation does not take place, but there will be increasing composition fluctuations: locally one of the solvent components has a higher concentration than the other. The correlation length of these fluctuations, ξ, diverges as we approach the critical point with $\xi = \xi_0 \left(\frac{T_c - T}{T_c} \right)^{-\nu}$, where ξ_0 is a system-specific parameter set by molecular pair potentials, and ν is the universal Ising exponent* [81, 84, 85]. Two surfaces close to each other can confine these composition fluctuations, causing an effective attractive force between them: the critical Casimir force [84]. The exact interaction between surfaces is set by experimental parameters which are fixed for a particular system: the solvent and the geometry and wetting properties of the confining objects. Because the correlation length of the critical fluctuations ξ grows as T approaches T_c, the attractive strength of the CCF grows as well. The latter is only set by $T_c - T = \Delta T$, the distance of the current temperature to the critical temperature, see Figure 2.2d.

In this thesis, we typically work at slightly off-critical solvent compositions. Say we approach the coexistence temperature T_{cx} at a concentration C_2, left of C_c in Figure 2.2a. At this composition, we are still close to C_c, so composition fluctuations increase as we approach the critical temperature. The fluctuations will predominantly consist of the component which is in shortage in the bulk, e.g., at concentration C_2 we have a 'shortage' of lutidine in the bulk, so any fluctuations

*To be more precise, $\nu \approx 0.63$ is the universal critical exponent of the three-dimensional Ising universality class for binary mixtures, and is part of the reason for the universality of the critical Casimir effect [83].

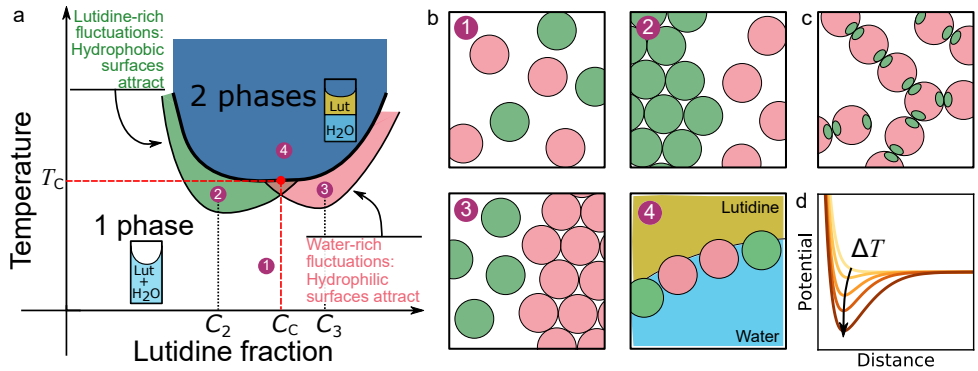

Figure 2.2 : The critical Casimir effect. (a) The phase diagram of a water-lutidine binary mixture. At temperatures below the critical temperature T_c, there is only one phase, above T_c the solvent phase separates into a water-rich and a lutidine-rich phase (dark blue region). Close to T_c, there are composition fluctuations. On the left side of C_c, fluctuations are lutidine-rich, and this cause hydrophobic surfaces to attract (green region). On the right side of C_c, fluctuations are water rich, and this cause hydrophilic surfaces to attract (red region). (b) Particle behaviour at different spots in the phase diagram. At spot 1, the critical Casimir force cannot overcome electrostatic repulsion: particles remain dispersed. At spot 2, in the green region, hydrophobic (green) particles attract, while hydrophilic (red) particles remain dispersed. At spot 3, visa versa: hydrophobic particles remain dispersed, while hydrophilic particles assemble. Finally, at spot 4, in the 2-phase region, phase separation occurs and the critical Casimir force is no longer relevant. (c) Assembly of patchy particles with hydrophobic patches and a hydrophilic bulk, in the green region of the phase diagram of panel (a). (d) The inter-particle attraction potential, composed of electrostatic repulsion and critical Casimir attraction, increases as a function of ΔT, the distance to T_c.

are lutidine-rich. This is crucial, because if a surface has a preference for one of the species in the binary mixture, they are sensitive to the composition of the fluctuations. In Figure 2.2a, left of C_c there are lutidine-rich fluctuations, which induces attraction between hydrophobic surfaces, while right of C_c there are water-rich fluctuations, which induces attraction between hydrophilic surfaces.

Selective particle assembly could thus proceed as follows: consider a mixture of hydrophilic and hydrophobic particles, both with a small electrostatic charge for stabilization and a solvent composition C_2, to the left of C_c, along which we slowly increase temperature, lowering ΔT, and approaching T_c. Initially, at large ΔT, there are only very small composition fluctuations, which cause only

minor attraction between particles, not enough to overcome their stabilizing repulsive electrostatic interactions (Figure 2.2b1). As ΔT decreases, the attractive strength between particles grows, and we reach a point where the hydrophobic particles start aggregating, T_{a} (Figure 2.2b2). Hydrophilic particles do not attract in this situation, and remain suspended. On the other hand, if we had chosen a lutidine fraction right of C_{c}, such as C_3, hydrophilic particles would assemble, and hydrophobic particles would not (Figure 2.2b3). In both cases, the attractive strength increases until finally, we cross T_{cx} and the binary solvent phase separates, rendering the critical Casimir force irrelevant (Figure 2.2b4).

Patchy Particle Assembly

Patchy particles combine the properties of the hydrophilic and hydrophobic particles described above. The particles employed here consist of a hydrophilic bulk and hydrophobic patches. This means that by selecting the solvent composition, we determine which part of the particle becomes attractive upon approaching T_{c}. Typically, we want the patches to be attractive, which means that we choose a composition left of C_{c} in Figure 2.2a, for instance C_2. When we approach T_{c} at this composition, the hydrophobic patches become attractive, while the hydrophilic bulk experiences only negligible attraction. This should lead to patch-to-patch assembly, indicated in Figure 2.2c. The behaviour can be easily inverted by taking a composition on the other side of C_{c}, making the bulk attractive and leaving patches neutral.

2.2.3 Critical Casimir in Real Life

As discussed above, this thesis will focus on the practical aspect of the critical Casimir effect rather than its theoretical underpinning. Therefore, the next few paragraphs will discuss practical problems, pitfalls and procedures involved in making the critical Casimir force work in real life.

Embracing Relativity

The equipment typically used for temperature control (see section 2.3.2) has excellent relative accuracy: deviation around a set temperature can be kept within a $0.02\,^{\circ}\mathrm{C}$ range. However, the absolute temperature will not be accurate at this very fine scale: not only is careful calibration necessary to achieve this precision,

but reported and actual temperatures will vary day-to-day due to environmental conditions, like seasonal variation in room temperature and the thermal contact of a sample with its heating elements. Since the strength of the CCF is very sensitive to small changes in ΔT (see for example Figure 4.10a), we cannot make use of the fluctuating absolute temperature, but must instead rely on an internal temperature calibration: the coexistence temperature T_{cx}. T_{cx} is easily found in experiments (it is the temperature at which phase separation takes place), and temperatures can be defined relative this point. Conveniently, since the coexistence line of the phase diagram is flat close to the critical concentration (see Figure 2.2a), $T_{\mathrm{cx}} \approx T_{\mathrm{c}}$ in most experiments, meaning that $T_{\mathrm{cx}} - T \approx T_{\mathrm{c}} - T = \Delta T$; the distance to T_{cx} is directly related to the strength of the critical Casimir forces. This assumption does not hold very close to T_{cx}, but this is rarely the case in practice.

Using T_{cx} as internal temperature control also solves another problem: variation between samples and measurements. Even when working extremely carefully, small differences in binary composition, salt concentrations, etc. will exist between individual samples and stocks. All these hard-to-quantify parameters, as well as environmental effects, are reflected in T_{cx}, which can vary up to a few tenths of a degree between samples. However, the behaviour relative to T_{cx} will hardly change, conveniently catching most of these minute variations.

The Water-Lutidine System

In this thesis, we make use of a binary solvent of 2,6-lutidine (commonly referred to as lutidine) and water. As mentioned, the critical Casimir effect is universal and arises in any binary solvent, however the water-lutidine system has some significant practical advantages. Crucially, the system has a lower critical solution temperature (LCST) just above room temperature at a very convenient temperature of approximately $34\,^{\circ}\mathrm{C}$ [86]. In a binary system with an LCST at or below room temperature, the sample would need to be cooled when not performing experiments, which is very inconvenient. A system with an upper critical solution temperature (UCST), like most binary solvents, is also not ideal: if the UCST is below room temperature, it requires accurate cooling below room temperature, which is more challenging than heating, and if the UCST is above room temperature, the sample would need to be heated when not performing experiments - also not ideal. On top of that, the lutidine-water mixture is well studied, and its phase diagram and critical behaviour, like viscosity and refractive index, have

been well known for decades [86–92]. Finally, lutidine is a bit less toxic and easier to work with then some of its commonly used alternatives, like 3-picoline and (heavy) water [93–95]. However, several other binary solvents with suitable properties are available over which the water-lutidine system does not offer significant benefits. Examples include 2-butoxyethanol and water [96, 97], and 1-propoxy-2-propanol and water [98]. Even solvents with micelles can and have been used to induce critical Casimir forces, although micelles will typically also cause depletion interactions as a side effect, making them less convenient [99, 100].

Salts

Apart from lutidine, water and particles, a typical sample also contains salt. Salt screens the charges on the particles so that the critical Casimir force can overcome the electrostatic repulsion. Besides suppressing electrostatic interactions, salts can also influence the critical Casimir force: preliminary tests with a few common salts ($MgSO_4$, KCl, and $CaCl_2$) reveal that magnesium sulfate enhances the attraction contrast between the particle patches and matrix [101]. This is important, because selective patch-to-patch assembly of patchy particles can only take place when there is sufficient contrast between patch and bulk. Ideally, the particle bulk behaves as a hard-sphere particle, while the patches are attractive.

Though only partially understood, ions have been shown to effectively shift the adsorption preference of colloidal particles in binary mixtures, thereby strongly changing their critical Casimir interaction [102–104]. The underlying reason may be in the special interactions between water and ions, the so-called *specific ion effects*. These effects are ubiquitous, especially in biochemistry, where it was first remarked upon over a century ago [105]. Despite the knowledge of the existence of specific ion effects, its origin is poorly understood, and only empirical descriptions exist, like the famous Hoffmeister series [106, 107]. The origin seems to lie in the different solvation energies surrounding certain ions [108], causing a range of secondary effects: different surface tension and different protein solubility among others.

Another salt-induced effect that could play a role in our particle systems is the solvent preference for individual ions. Some salts are *antagonistic*: they consist of a hydrophobic and a hydrophilic ion. It is known that the preference of these ions for either component of the binary solvent can influence the phase diagram of

water-lutidine significantly [109]. In the 'simple' magnesium sulfate salt we use, this effect is likely small, but it could play a role.

It is not clear that either specific ion effects or antagonistic salts are at play in increasing patch-to-bulk attraction contrast, but it does illustrate that there is more to salt ions than just their charge, especially in a system close to the critical point of demixing, where such effects may be amplified. Careful screening and selection of the salt in a system is required to optimize the patch-to-patch attraction.

Optimizing the Critical Casimir Force

To investigate the properties of particle bulk and patches separately, and find the optimal conditions for the patchy particle assembly, we first focus on the assembly behaviour of the two particle components of the patchy particle, polystyrene (PS) and 3-(trimethoxysilyl) propyl methacrylate (TPM). We use the precursor PS spheres of the colloidal fusion synthesis of particle batch A (Table 2.1), and TPM droplets polymerized under the same conditions as the patches. This results in solid TPM particles of diameter $\sigma = 1\ \mu\mathrm{m}$ that have the same surface properties as patches in the final composite patchy particle.

We vary the composition and salt concentration of the binary solvent to determine the optimal selective TPM-TPM (and thus patch-to-patch) attraction. For this purpose, TPM and PS particles are dispersed in binary mixtures of varying lutidine concentration for microscopic characterization. Samples are imaged while the temperature is slowly increased towards T_c using a temperature-controlled stage (see section 2.3.2). An oil-immersion objective with 63x magnification is used for bright-field imaging. By increasing the temperature slowly we identify the aggregation temperature T_a, at which clear cluster formation occurs (as shown in Figure 2.3a) and the coexistence temperature T_cx, at which bubbles form. From this, we construct aggregation lines with respect to the solvent phase-separation line as a function of lutidine concentration as shown in Figure 2.3b.

The aggregation lines in Figure 2.3b show that without $\mathrm{MgSO_4}$, PS particles (blue line) and TPM particles (red line) aggregate stronger for lutidine concentrations right of the critical composition, meaning that they both show the same water-philic affinity and thus no selective patch-to-patch attraction. However, by adding 0.5 mM of magnesium sulfate, the aggregation behaviour of TPM particles changes completely: a strong critical Casimir attraction is observed to the left of the critical composition, green line in Figure 2.3b. This indicates that the

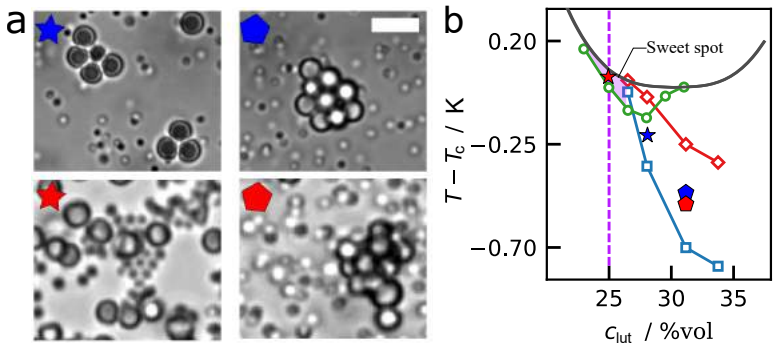

Figure 2.3 : Enhancing the contrast for critical Casimir patch-to-patch binding. (a) Bright field images showing aggregation contrast of PS particles (big dots) and TPM particles (small dots). The former make the bulk, the latter the patch of the composite patchy particle. Clockwise, starting top left, conditions are: c_{lut} = 28%vol, [$MgSO_4$] =0 mM; c_{lut} = 32%vol, [$MgSO_4$] = 0 mM; c_{lut} = 25%vol, [$MgSO_4$] = 0.5 mM; and c_{lut} = 32%vol, [$MgSO_4$] = 0.5 mM. Scale bar is 3 µm. (b) Aggregation diagram showing the shifted aggregation lines of TPM without salt (red diamonds), with [$MgSO_4$] = 0.5mM (green circles), and PS without salt (blue squares). Black continuous line shows theoretical coexistence temperature of the binary mixture close to the critical point. Coloured stars and pentagons indicate corresponding measurement condition of (a). Purple dotted line indicates a good lutidine concentration for patchy assembly $c_{\mathrm{lut}} = 0.25$.

adsorption preference of TPM switches to lutidine-philic when adding $MgSO_4$, while the aggregation temperature of PS particles is little affected and remains water-philic as can be seen from the snapshots that show cluster formation of PS still happens on the right side of the critical temperature, Figure 2.3a (bottom right). Using the aggregation curves, we pinpoint a sweet spot where only TPM particles are expected to attract (small violet-shaded region in Figure 2.3b).

After determining the best solvent composition, all our experiments are performed in the region where we obtain the strongest selective patch-to-patch attraction: we use an optimal lutidine concentration $c_{\mathrm{lut}} = 25\%$vol., with 1 mM $MgSO_4$ that shows the largest range of TPM-TPM (and thus path-to-patch) attraction while PS is not attractive.

2.3 From Sample to Data

The vast majority of the experiments performed in the context of this thesis relies on optical microscopy to observe the assembly process and resulting structure - specifically laser scanning confocal microscopy. All experiments are performed under accurate temperature control, as to control the strength of the critical Casimir force. Microscopy can yield rich and insightful information on a local level - one can literally see what happens at the microscopic level, but the technique is less suited for bulk behaviour and averages, because it only catches a relatively small area of the sample at a time. Scattering techniques (SAXS, SANS, SLS, etc.) are more suitable for bulk characterization, and are therefore also the more traditional techniques for probing colloidal length scales. However, microscopy is the method of choice for the study of patchy particle assemblies. Not only do patchy particles typically have interesting local behaviour, but, as highlighted in section 1.3, patchy particle assemblies typically are very small, rendering scattering experiments meaningless.

A widely-recognized problem with microscopy data analysis is the risk of (unconscious) bias. Therefore, it is of particular importance to go from images to usable data in a reproducible and objective way. In this section, I will set out to explain the process of preparing the sample, briefly describe the microscopy setup, and finally describe the analysis of the microscopy data, specifically with regard to (patchy) particle tracking.

2.3.1 Sample Preparation and Glass Silanization

The patchy particles are stored dispersed in water with a small amount of F108 copolymer as stabilizer ($< 0.05\%$wt). To prepare a sample stock, particles are transferred to the binary solvent by washing them at least 4 times in the desired binary mixture. This mixture can be stored in small centrifugation tubes for a few weeks. To prepare a sample for microscopy, a small amount of the sample is injected into a glass capillary (Vitrotubes, Rectangle Boro Tubing $0.20 \times 2.00\mathrm{mm}$) and sealed with teflon grease (Krytox GPL-205), see Figure 2.4.

In some cases, we use hydrophobic silanized glass capillaries. The hydrophobic treatment for capillaries is a simple gas silanization reaction. The capillaries are cleaned thoroughly using a piranha treatment, or alternatively using Hellmanex III and plasma treatment. Capillaries are then placed in a vacuum desiccator

together with approx. 1 ml of hexamethyldisilazane (HMDS) ($\geq 99.0\%$, Sigma-Aldrich). Pressure is lowered to below 200 mbar using a pump, and kept low for at least 2 hours. The capillaries are then baked in an oven at 120 °C for circa 1 hour. Microscopy samples can then be prepared as usual with these capillaries [110–112].

Samples that are properly sealed with teflon grease will remain stable for approximately 1 month. If the ends are properly sealed with an extra layer of glue (Norland Optical Adhesive, nr. 81), samples can be stable without significant change in function for over a year.

2.3.2 Optical Microscopy and its Temperature Control

All samples are imaged on a Zeiss Axiovert 200M inverted optical microscope, either in bright field, fluorescence (532 nm laser) or confocal (LSM 5 Live line-scanning confocal microscope module with 532 nm laser) mode. The microscope is equipped with a well-controlled temperature stage in combination with an objective heating element, as fine temperature control is indispensable to make use of the critical Casimir force. Relative temperature accuracy far below a tenth of a degree, needed to have meaningful control over patch-to-patch attraction in our system, is achieved using a home-built closed loop water system.

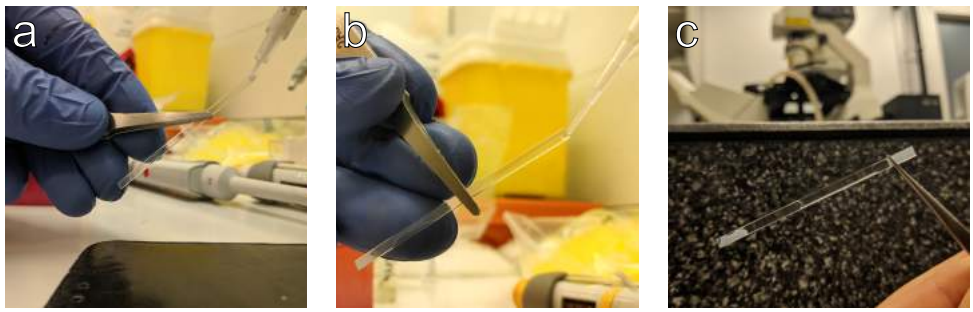

Figure 2.4 : Sample preparation. After a particle dispersion with the right concentration has been prepared, the dispersion is injected into capillaries to be able to observe the sample under a microscope. To prepare a sample, (a) teflon grease is injected into one end of a capillary. (b) The particle dispersion is then very carefully injected into the capillary from the non-sealed opening using a 10 µL micropipette. (c) The open end of the capillary is now also injected with teflon grease, closing off the mixture from the environment. We now have a capillary ready for microscopy.

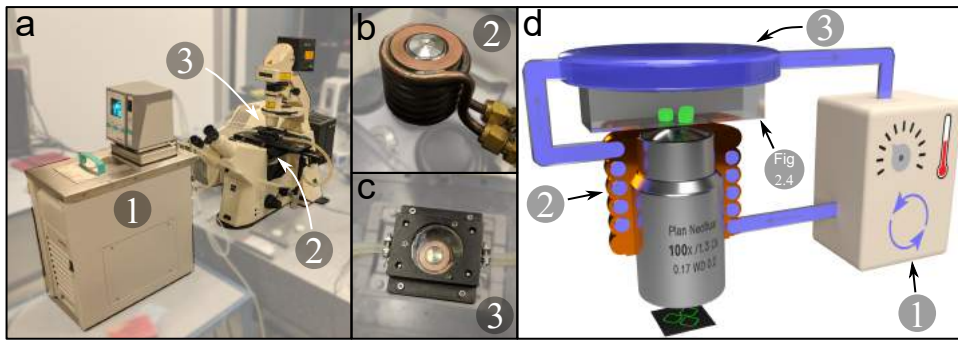

Figure 2.5 : The microscope and its temperature control. An overview of the microscopy setup is shown in (a). The waterbath controlling the temperature is labelled 1. The coil heating the objective is labelled 2, and is highlighted in (b). The sample holder is labelled 3, and is highlighted in (c). In (d), the heating system is shown schematically, with the water flow between elements indicated, adapted from [113].

The temperature control is based on water flowing through the components of the microscope that are in contact with the sample, see Figure 2.5: the sample stage on which the sample is mounted, and the objective, which can act as a heat sink by proximity or direct contact (in case of an air or oil objective respectively). Accurate control of the water temperature thus leads to accurate control over the sample temperature. We use a Julabo D25 ME waterbath to pump temperature-controlled water through the sample stage and objective. The sample stage consists of a glass cell trough which water can flow. The transparent glass stage allows bright-field microscopy to be performed with the illumination from the top, a significant advantage over available commercial solutions. The objective is heated by the temperature-controlled water flowing through a brass tube coiled around it.

This setup allows for a relative temperature accuracy of about $0.01\,^{\circ}\mathrm{C}$ with minimal temperature gradients while performing microscopy. This is easily verified by looking at the data gathered in this thesis, much of which would be impossible without very accurate and stable temperature control.

2.3.3 Particle Tracking

To extract useful data from the microscopy images, we track all particles in the field of view, meaning we determine their x, y, and possibly z coordinates. In

fluorescence microscopy, fluorescent colloidal particles manifest as Gaussian peaks in intensity. The most common way to locate these peaks is by using the algorithm proposed by Crocker and Grier in the 90s [114]. Not only does the algorithm find fluorescent features, it finds them with sub-pixel accuracy by fitting to a Gaussian distribution instead of simply finding the centre [115]. This means that, even though a pixel size is typically not much smaller than the feature of interest, locations can be determined with an accuracy of up to 0.2% of the feature radius.

Recently, machine learning has started to become more common in scientific image analysis. Especially complicated environments with a lot of background and noise (e.g., biological samples) benefit from improvements in noise reduction and detection optimization [116–119]. However, to my knowledge, machine learning algorithms are currently not matured enough to outperform the classical Crocker-and-Grier algorithm in relatively simple colloidal systems.

The specific software we use for particle tracking is Trackpy, a modern Python implementation of the Crocker-and-Grier algorithm [120]. After loading an image and optimizing parameters, it can accurately determine patch locations in two or three dimensions. However, in this thesis, simply finding the bright spots in an image is only the first step in determining particle locations. Patchy particles are synthesized such that the patches are fluorescent (see section 2.1). A tetrameric patchy particle will thus not have one bright spot, but four, each of which are at a different x, y, and z-position. On top of that, if particles are bonded patch-to-patch we observe just one fluorescent dot which represents two bonded patches, belonging to different particles. To accurately track particle centre, orientation, and bonding, different algorithms were designed and implemented, depending on the details of the system and the information available.

Double Channel Tracking

In Chapter 3, we discuss the formation of clusters of five particles, each bonded with two other particles. Accurate three-dimensional tracking of the particles is achieved by overlaying bright field and confocal microscopy channels, shown in Figure 2.6a. Figure 2.6b shows the full three-dimensional representation of the ring. We determine the particle location and orientation in five steps:

1. Determine the two-dimensional centre of particles from the bright-field channel.

2. Determine the three-dimensional centre fluorescent patches from an entire confocal image stack.

3. Using the estimated particle and patch centres from steps 1 and 2, determine which patches (potentially) belong to the same particle.

4. Draw a tetrahedron for all possible combinations of 4 patches that could belong to the same particle, as shown in Figures 2.6c& d.

5. Determine the angular tetrahedrality order parameter S_{g} [121] and the distance order parameter S_{d},

$$S_{\mathrm{g}} = \sum_{i=1}^{4} \sum_{j=1, j\neq i}^{4} \left(\mathbf{r}_i \cdot \mathbf{r}_j + \frac{1}{3} \right)^2 \tag{2.1}$$

$$S_{\mathrm{d}} = \sum_{i=1}^{4} \frac{\left(d_i - \overline{d}\right)^2}{\overline{d}^2} \tag{2.2}$$

with i and j patch indices, $\mathbf{r}$ the unit vector pointing from the centre of the 4 patches to a patch, and d the length of $\mathbf{r}$. If these order parameters are below a threshold (typically $S_{\mathrm{g}} < 0.25$, $S_{\mathrm{d}} < 0.20$), the group of patches forms a regular tetrahedron of the right size; we assume these are patches that make up a particle, see Figure 2.6c. If the threshold is not reached, we are observing a false positive, see Figure 2.6d.

We have thus determined 4 patches belonging to the same particle, the average location of which is the particle centre. We can determine whether particles are bonded by simply checking which particles share a patch.

Network-based Tracking

Unfortunately, the double channel approach is not always feasible because it requires double channel microscopy: the switching between channels makes the measurement slow. Therefore, in Chapters 4&5, we employ a slightly different approach. In this situation, particles are all at the same height, with one patch bound to the surface and the other three available for bonding. Although this particular conformation is not strictly necessary for this tracking approach to succeed,

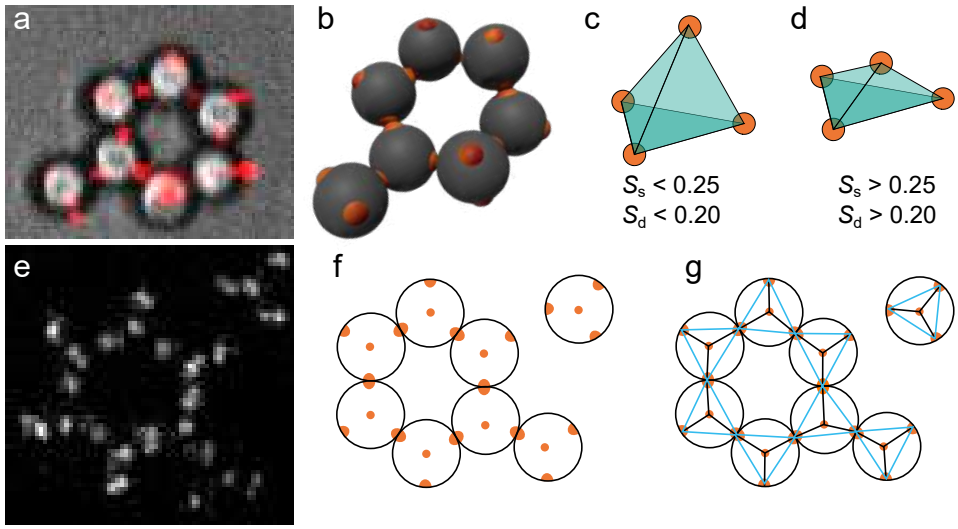

Figure 2.6 : Overview of tracking procedures developed in this thesis. (a) Representative microscopy image of particles as taken in Chapter 3, where we use confocal images (in red) superimposed onto bright-field microscope image. Note that because we project a 3D image onto a 2D image, most particles seem to have only 3 patches per particles, while they have 4. (b) 3D representation of situation shown in (a). (c) A group of 4 patches belonging to the same particle, forming a regular tetrahedron, which has an S_g and S_d below the threshold value. (d) A group of 4 fluorescent features, forming an irregular tetrahedron, which has an S_g and S_d above the threshold value. One or more of the features is likely a false positive. (e) Representative z-projected confocal microscopy image of particles as taken in Chapter 4. (f) Representation of situation shown in (e). Particles have a black outline, patches are shown in orange. The central patch is slightly out of focus, and will thus be less bright in (e). (g) The network formed by connecting all patches within a particle radius of each other. Regular triangles, and thus the groups of connected outer patches are shown in cyan.

it does simplify tracking significantly. In Figure 2.6e, a typical microscopy image is shown, with in Figure 2.6f a schematic representation of the situation. Each particle has one central patch in the centre of the particle, and 3 patches at the edge of the particle. To find particle positions, we perform the following actions:

1. Determine the location of each fluorescent patch.
2. Find all other patches within approximately one particle radius, by using a kd-tree (implemented in SciPy) [122], and connect those into a network.
3. Find all triangles in the resulting network (Figure 2.6g).
4. For each triangle, we determine the mean edge length and the variation of this value. We only select triangles where the mean edge length d is close to the expected value based on radius r ($d = \frac{4}{\sqrt{3}}r$), and where the edge length variation is small. This means we effectively select the blue triangles in Figure 2.6g.

We are left with a triangle with 3 vertices corresponding to the outer patches. In the centre of the triangle is the patch bound to the surface. Particle bonds are easily determined by checking which patches are shared between particles.

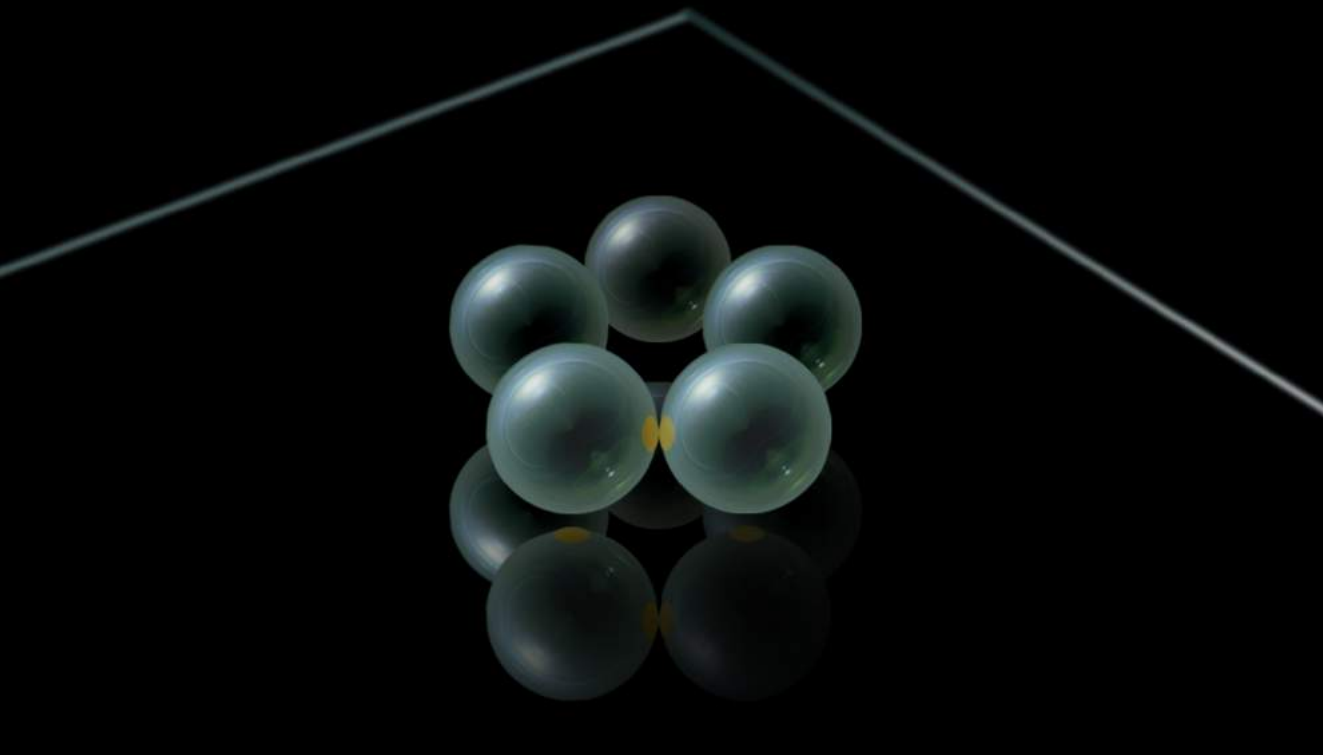

3 Mimicking Molecules: Pickering Particles and Catalytic Colloidal Conversion

Do not disturb my rings!

Archimedes of Syracuse
Last words (supposedly)

Colloids have a rich history of being used as *big atoms* mimicking real atoms to study crystallization, gelation and the glass transition of condensed matter. Emulating the dynamics of molecules, however, has remained elusive. Recent advances in colloid chemistry allow patchy particles to be synthesized with accurate control over shape, functionality and coordination number. In this chapter, I discuss how colloidal alkanes, specifically colloidal cyclopentane, assembled from tetrameric patchy particles by critical Casimir forces undergo the same chemical transformations as their atomic counterparts, allowing their dynamics to be studied in real time. Transitions between chair and twist conformations in colloidal cyclopentane are observed directly, and we elucidate the interplay of bond bending strain and entropy in the molecular transition states and ring-opening reactions. These results open the door to investigate complex molecular kinetics and molecular reactions in the high-temperature classical limit, in which the colloidal analogue becomes a good model.

3.1 Introduction

Colloidal particles have been much used to study phase transitions such as crystallization, gelation and the glass transition of condensed matter at experimentally accessible length and time scales [1]. In this analogy, atoms are represented by homogeneous colloidal spheres with tunable interactions between them. This approach has been successful, and many of the lessons learnt are directly applicable to fields such as photonics [123], opto-electronics [124], and bio-materials [125].

Compared to these crystalline systems, molecules typically have a much richer structure: atoms are generally bonded directionally into molecules via valence. For example, in aliphatic organic compounds in which a carbon atom has four bonds, such as methane (CH_4), the carbon atom is in an sp^3 hybridized state, binding ligands in a tetrahedral arrangement at approx. $109.5°$ bond angles. However, although many theoretical and simulation studies exist, achieving directional bonding in colloidal systems is challenging, and reliable experimental systems are scarce [25, 43, 126]. Recently developed patchy particles, decorated with patches of specific surface chemistry, with well-defined symmetry, allow reproducing the geometry of valence bonds [50, 59, 60, 67, 127, 128]. While these particles mimic the rigid shape of small molecules, emulating molecular reactions and conformational dynamics would require degrees of freedom similar to that of organic molecules, through reversible, specific patch-patch interactions, tunable on the scale of k_BT, the thermal energy [128]. Such interactions would open the door to colloidal molecular chemistry: molecules that consist of colloidal particles instead of atoms, reacting at the nano and micrometer scale, directly observable by microscopy. This in turn could unlock design paths for nanostructured materials [129].

Specific, adjustable colloidal interactions arise in binary solvents close to their critical point. This *critical Casimir force* results from the confinement of solvent fluctuations between particle surfaces in a near-critical mixture, giving rise to an effective interaction that is precisely tunable with temperature and the adsorption preferences of the confining surfaces, see section 2.2. For isotropic particles, these interactions have provided insight into gas-liquid and liquid-solid phase transitions [130, 131] as well as gelation [132]. Combined with *patchy particles* exhibiting surface patches of specific solvent affinity, the interactions become directed, and may allow the reversible assembly of more complex, molecule-like structures, and their direct particle-scale observation.

In this chapter, we show that patchy particles bonded via critical Casimir forces allow direct-space investigation of molecular dynamics, providing insight into thermally activated molecular transition states. We bind dimer and tetramer particles into colloidal alkanes, resembling alkane molecules, such as colloidal (cyclo)butane, butyne, cyclopentane, and cyclohexane, and investigate their dynamics directly in real space using confocal microscopy. We find that just as molecular cyclopentane, colloidal cyclopentane exhibits envelope and twist conformations that interconvert in time, and we follow the kinetic pathway in great detail. Furthermore, we measure the free energy and corresponding bending energy directly from the observed molecular trajectory; this allows us to elucidate the interplay of bond strain and entropy in thermal and catalytic dissociation reactions of colloidal cyclopentane. These results open up directions for studying the dynamics of molecules using precisely coordinated patchy particles, and for building complex nano- and micrometer-scale materials [1].

3.2 Results

3.2.1 Colloid Fabrication

We use patchy particles described in section 2.1.1, particle batch A&B from Table 2.1. To quickly recap: patchy particles are polystyrene (PS) and 3-(trimethoxysilyl)propyl methacrylate (TPM) spheres produced by colloidal fusion [67]. The synthesis yields particles with precisely linearly and tetrahedrally coordinated, fluorescently labelled TPM patches in a PS matrix (Figure 3.1a). The tetrapatch particles have a diameter of $\sigma_{\mathrm{tetra}} = 3.7\,\mu\mathrm{m}$, dipatch particles $\sigma_{\mathrm{di}} = 3.2\,\mu\mathrm{m}$ and both have a patch diameter $0.5\,\mu\mathrm{m} > d_{\mathrm{p}} > 0.4\,\mu\mathrm{m}$; sufficiently small to allow only a single other patch to bind. Di- and tetrapatch particles with number ratio $1:3$ are dispersed at a volume fraction of $\phi = 0.01$ in a binary mixture of lutidine and water close to its critical point. We also add $1\,\mathrm{mM}$ $\mathrm{MgSO_4}$ to screen the electrostatic repulsion and enhance the lutidine adsorption of the patches, see section 2.2.3. Upon approaching the solvent demixing temperature $T_{\mathrm{cx}} = 33.8\,^{\circ}\mathrm{C}$, lutidine-rich fluctuations arise between the patches, binding them into a covalent bond analogue by critical Casimir interactions as illustrated in Figure 3.1b. To assemble colloidal molecules, we heat the sample to $\Delta T = 0.04\,\mathrm{K}$ below T_{cx},

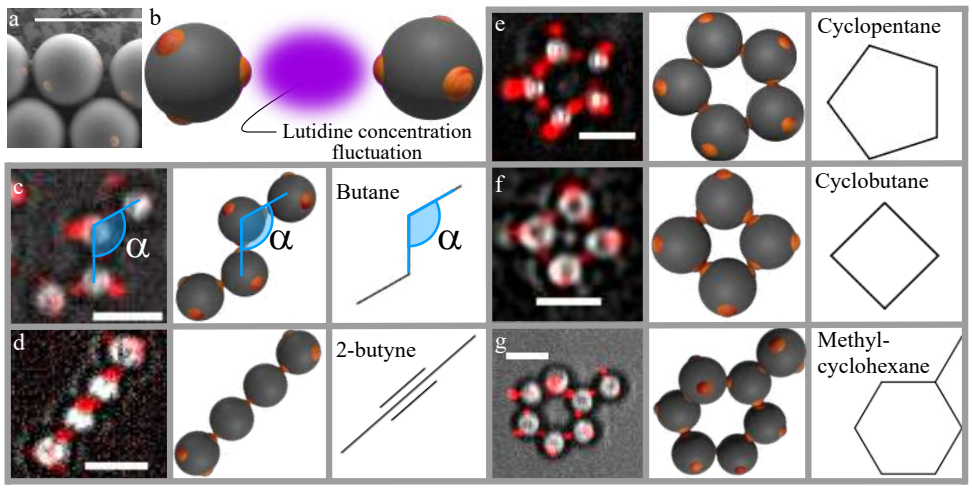

Figure 3.1 : Colloidal molecules assembled by critical Casimir forces. (a) Scanning electron microscope (SEM) image of tetramer patchy particle with patches coloured yellow. Scale bar corresponds to 5 μm. (b) Schematic of the directed critical Casimir interaction: lutidine fluctuations confined between hydrophobic patches cause patch-to-patch attraction. (c-g) Examples of colloidal molecules: colloidal butane (c), 2-butyne (d), cyclopentane (e), cyclobutane (f) and methylcyclohexane (g), confocal superimposed onto bright-field microscope images highlighting patches in red (left), schematic reconstruction (middle) and chemical representation (right). In (c), the characteristic tetrahedral bond angle $\alpha = 109.5°$ is indicated. In (d), the linearly connecting dipatch particles mimic *sp* hybridized carbon atoms, which in the colloidal analogue link both dipatch and tetrapatch particles.

resulting in a predicted binding energy of the patches of approximately $15k_{\mathrm{B}}T$ (see section 3.4.4) [82, 133].

3.2.2 Colloidal Alkanes

After a few hours, we observe bonded structures exhibiting the coordination and bond angles of carbon atoms in organic molecules, as shown in Figure 3.1c to g (see section 3.4.5 for assembly details). A zigzag chain of four tetrapatch particles exhibiting the carbon backbone structure of butane is shown in Figure 3.1d. A colloidal analogue of 2-butyne, consisting of 2 central dipatch particles with 2 tetrapatch particles capping both ends, is shown in Figure 3.1e. Analogues of cyclic alkanes, ubiquitous in carbon chemistry, are shown in Figure 3.1e-g. Rings consisting of four, five, and six tetrapatch particles are observed, which we identify as colloidal cyclobutane, cyclopentane and cyclohexane. We note that unlike their atomic counterpart, these colloidal molecules have unsaturated patches, lacking their 'hydrogen atoms', which may lead to some difference in their reactivity and conformations.

We show size distributions of colloidal molecules in Figure 3.2. Clearly, smaller structures are in the majority, but a significant population of larger structures is present in the sample. The population decreases exponentially with size, as predicted for patchy particle systems [134]. Cyclic molecules, however, show a clear preference for a certain number of particles, reflecting their compatibility with the tetrahedral bond angle. Colloidal cyclobutane (Figure 3.1f) is rarely encountered in our samples. This is not surprising considering its highly strained bond angles. In this configuration, two bonded neighbours make an angle of $90°$, far from the ideal angle of $109.5°$, causing high bond strain. For atomic cyclobutane, this high bond strain is known to cause the enhanced reactivity of cyclobutane compared to butane, making it much less stable than cyclopentane and cyclohexane that exhibit bond angles much closer to $109.5°$. Indeed, we find that colloidal cyclopentane (Figure 3.1e) is much more ubiquitous in the sample, and by far the most observed colloidal ring structure. Its bonds are much closer to the ideal $109.5°$ tetrahedral bond angle, compared to cyclobutane. Curiously, six-membered rings - cyclohexanes - are much less frequently observed, even though they have a lower bond angle strain, probably due to kinetic effects [25].

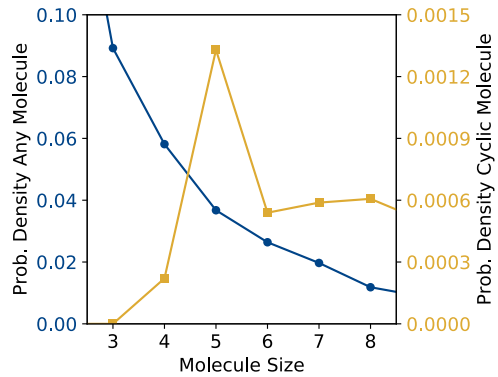

Figure 3.2 : Size distribution of colloidal molecules. Probability of occurrence of colloidal molecules as a function of their size. Blue dots (left axis) show all molecules, while yellow squares (right axis) show cyclic molecules only. Clearly, larger molecules are increasingly rare, while among the cyclic structures, 5-particle compounds such as cyclopentane are most frequently observed.

3.2.3 Conformations of Colloidal Cyclopentane

We focus on the most frequently observed cyclic structure, colloidal cyclopentane, and image its three-dimensional bonding arrangement using confocal microscopy. The three-dimensional reconstructions reveal three basic conformations (Figure 3.3a): a planar conformation with all particles in the same plane, an 'envelope' conformation, with one particle sticking out, and a 'twist' conformation with one particle sticking out above, and an adjacent particle sticking out below the plane. Just as its colloidal counterpart, atomic cyclopentane also shows these conformations; like most cyclic molecules, the internal angles of the ring are not compatible with the 109.5° bonding angle of the tetrahedral symmetry. In planar cyclopentane, the angles are only slightly lower, at 108°; nevertheless, due to energetic considerations - the steric hindrance of hydrogen atoms and torsional strain - atomic cyclopentane is virtually always puckered out of plane [135].

Conversely, colloidal cyclobutane shows virtually no puckering, as shown by the significantly narrower bond angle distributions in Figure 3.3b. Cyclobutane shows a much narrower bond angle distribution, in particular lacking the tail towards larger angles as observed for cyclopentane, which is a signature of its puckering configurations (see section 3.4.6 for a comparison of bond angle distributions of different colloidal molecules). Hence, while there is a driving force for out of plane movement of cyclopentane, and thus a relatively wide angular

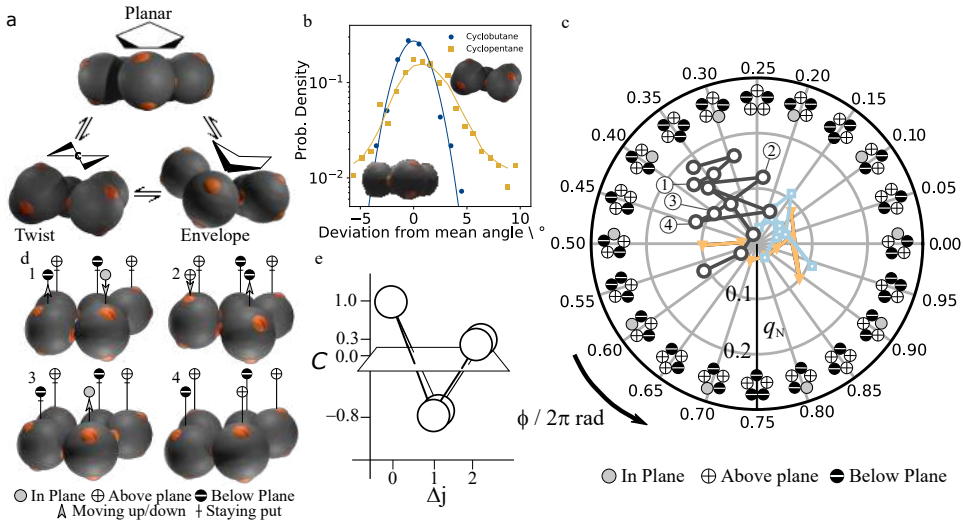

Figure 3.3 : Conformations and pseudorotation of colloidal cyclopentane. (a) Three-dimensional reconstructions of typical conformations of colloidal cyclopentane: *planar* conformation (top), *twist* (or *half-chair*) conformation (left), and *envelope* (or *bend*) conformation (right). (b) The distribution of inter-particle angles in cyclobutane (blue dots) and cyclopentane (yellow squares). The solid lines are a guide to the eye. (c) Representation of cyclopentane conformations in polar q-ϕ space. At each $0.05 \cdot 2\pi$ interval, a 2D representation of the ring is shown. The three paths (grey circles, orange triangles and blue squares) show typical puckering routes of a thermally activated ring through q-ϕ space. The four labelled subsequent points along the grey circle path correspond to the snapshots in panel (d). (d) Time series of three-dimensional configurations showing pseudorotation of colloidal cyclopentane. Snapshots are $\Delta t = 12$s apart, while the typical relaxation time of a conformation is 24s, see section 3.4.7. Symbols + and - indicate particles above and below the average plane, respectively, and arrows indicate particle movement towards the next time step. (e) Correlation function of out-of-plane displacements $C(\Delta j) = \langle z_j \cdot z_{j+\Delta j} \rangle / \left\langle z_j^2 \right\rangle$ in a perspective view, illustrating average puckered configuration of the ring.

distribution, cyclobutane bonds are stiffer, forcing the highly strained ring into a narrowly confined configuration (video available online [231]).

3.2.4 Pseudorotation

For each particle in cyclopentane, there are two envelope and two twist conformations, as shown in Figure 3.3c. In molecular cyclopentane, these conformations are thought to interconvert continuously. This process is known as pseudo-rotation, and has been suggested as early as the 40s, but so far has only been confirmed by indirect spectroscopic evidence [136–139]. Likewise, we find that in colloidal cyclopentane, envelope and twist conformations interconvert continuously. To follow the pseudorotation directly in real space, we rapidly acquire image stacks every twelve seconds, roughly 2 times faster than the typical relaxation time of a configuration, see section 3.4.7. Three-dimensional reconstructions reveal the pseudorotation of colloidal cyclopentane in Figure 3.3d and online videos[231, 232]. From frame 1 to 2, a particle (left) flips from below to above the plane, while its in-plane neighbour moves down out of plane. From frame 3 to 4 a characteristic change from envelope to a neighbouring twist conformation occurs, corresponding to the upward motion of the (central) in-plane particle. Remarkably, during these transition states, the ring always remains highly puckered. To show this, we correlate the vertical displacements, z_i, of nearest and second-nearest neighbour particles and find that they are strongly anticorrelated, as shown in Figure 3.3e: the upward movement of a particle typically results in the downward movement of the neighbouring particle, followed by an upward movement of the next nearest neighbour. These correlations highlight the strongly correlated nature of the pseudorotation of colloidal cyclopentane, and suggest that interesting collective behaviour is to be expected in larger colloidal molecules.

To analyse the pseudorotation in detail, we determine the puckering amplitude q and phase ϕ from the out-of-plane displacements z_i of the particles. Together, q and ϕ form a polar phase space describing all possible puckering conformations. Given an average plane through the ring, q is a measure of the resulting amplitude of the out-of-plane displacements, while ϕ tells us in what conformation the ring is, as indicated schematically in Figure 3.3c [140] (see section 3.4.3 for formal definition of q and ϕ). A polar plot of the pseudorotation trajectory in (q, ϕ) space is shown in Figure 3.3c (see online videos for animations [233, 234]). The coordinated up and down motion leads to pronounced changes in the puckering phase (phase change from frame 1 to 2 to 3 to 4). For example, the large phase change from 2 to 3 corresponds to a change from twist to a next-nearest envelope conformation, while that from 3 to 4 corresponds to a transition from twist to en-

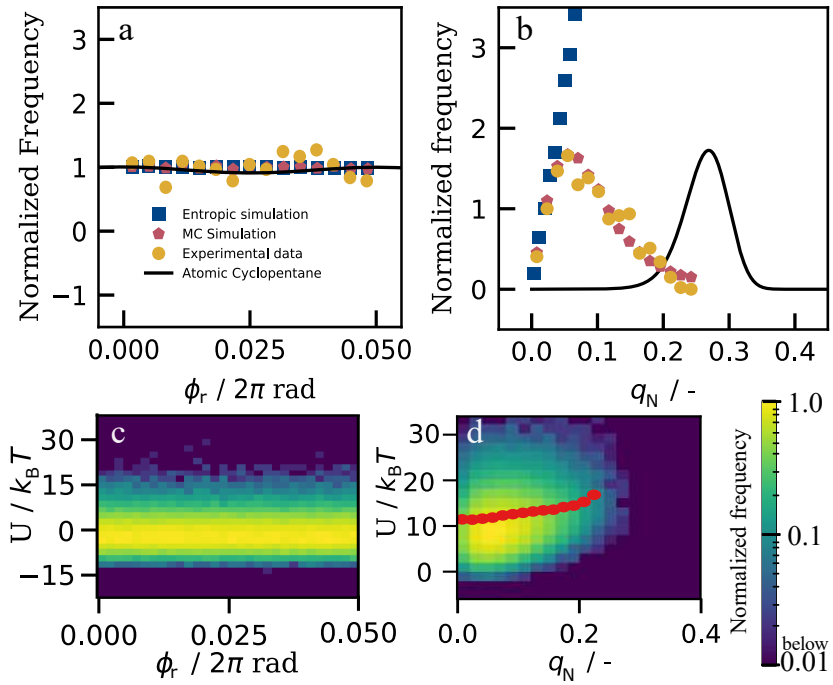

Figure 3.4 : Distributions of puckering configurations. (a) Normalized frequency of the reduced puckering phase angle, ϕ_r from envelope ($\phi_r = 0$) to twist conformation ($\phi_r = 0.05 \cdot 2\pi$rad). The flat distribution reveals no preference for a particular conformation. (b) Frequency $f(q_N)$ of the normalized puckering amplitude q_N: experimental data (yellow dots), Monte Carlo simulations of freely joint particles (blue squares), and particles interacting with an effective critical Casimir potential (red pentagons), and expected values for atomic cyclopentane as given in [138], assuming the largest reasonable envelope-to-twist energy barrier (solid black line). Frequency is normalized to result in identical initial slopes. (c) and (d) show probability density maps of total bending energy as a function of ϕ_r and q_N, respectively, for the simulated patchy particle rings. The logarithmic colour map indicates the normalized frequency of observation from below 0.01 (blue) to 1.0 (yellow). Red circles indicate the average bending energy as determined from the measured distribution of q_N.

velope, as shown by comparison of the trace in Figure 3.3c with the corresponding 2D representations.

To explore the full statistics, we follow more rings, and determine distributions of the reduced puckering phase ϕ_r and amplitude q as shown in Figure 3.4a&b. The reduced puckering phase indicates how far a particular configuration is be-

tween an envelope (ϕ_r = 0) and a twist (ϕ_r = 0.05) conformation. The flat distribution of ϕ_r indicates that, just like in atomic cyclopentane, there is no preference for either envelope or twist conformation, nor any conformation in between. This is different for the puckering amplitude q (Figure 3.4b): Planar conformations with $q \approx 0$ are almost never observed, while mildly puckered configurations with $q \approx 0.06$ are most prevalent. As shown by simulations in section 3.4.4, the peak position depends on the presence of gravity: without gravity, the maximum of the probability density is shifted towards larger values ($q_N \approx 0.15$) compared to the experimental measurement, meaning that the colloidal cyclopentane ring is more puckered in a system without gravity, as expected. Nevertheless, the presence of a finite puckering amplitude is surprising from an energetic point of view, as the flat ring ($q = 0$) has both the lowest bending and gravitational energy.

However, the entropy of this state is also the lowest: there is only one way to place the particles into a flat ring; even a small amount of puckering will unlock many configurational microstates, thus increasing the entropy.

To estimate the entropic contribution, we consider a ring of five freely joint particles moving up and down independently. The corresponding probability distribution $P(q)$ increases linearly with q (Figure 3.4b), reflecting the increasing number of configurations. The experimental distribution initially follows this trend, but then peaks and diminishes. We associate this decrease with the increasing bending energy cost $U(q)$ suppressing high-puckering amplitude configurations.

Together, entropic and bending energy contributions give rise to the free energy $F(q) = U(q) - TS(q)$, where $S(q) = k_B T \ln P(q)$ is the entropy associated with the ring configurations. In thermal equilibrium, puckering amplitudes follow a Boltzmann distribution $f(q) \propto \exp(-F(q)/k_B T)$. We invert this relation to determine the average bending energy from the measured distribution $f(q)$ using

$$U(q) = k_B T \ln \frac{P(q)}{f(q)} + U_0, \tag{3.1}$$

where U_0 is an arbitrary reference energy, see section 3.4.8. The resultant $U(q)$ indeed reveals an increasing bending energy with puckering amplitude, as shown in Figure 3.4d (red circles).

These trends are confirmed in Monte Carlo (MC) simulations of five tetrapatch particles interacting with effective critical Casimir potentials as detailed in section

3.4.4. Their puckering distributions are in excellent agreement with the experimental data, as shown in Figure 3.4. Furthermore, we compute the total bending energy U directly from the strained bonds for each observed configuration; the resulting probability contour plot shows good agreement with the experimental data (Figure 3.4d).

Interestingly, atomic cyclopentane shows a distribution peaked at much higher values of q. Contrary to colloidal cyclopentane, the molecule experiences additional H-H steric repulsions as well as torsional strain, leading to a stronger degree of puckering. Nevertheless, the subsequent decline indicates occurrence of additional bending energy, similar to the colloidal analogue.

3.2.5 Ring Breaking and Catalytic Reactions

We fully exploit the direct observation of colloidal cyclopentane by studying ring--opening reactions. Rings occasionally break up as shown in Figure 3.5a and online video [235]; this breakup is the thermal ring-opening reaction of colloidal cyclopentane to pentane (formally a pentane bi-radical). Interestingly, we find that just before breaking, rings always exhibit a high puckering amplitude, as shown in Figure 3.5b. Moreover, the bond breaking occurs at a particle strongly involved in the puckering, as shown by comparing the puckering phase just before bond breaking with the breaking point in Figure 3.5b. Because a high puckering amplitude corresponds to high bond strain, a large energy gain is made by breaking the bond. These results highlight the importance of bond-bending strain in the thermal dissociation of colloidal cyclopentane. Furthermore, the high q values just before breaking suggest that the reactivity of cyclopentane is highest for extreme puckering amplitudes, in the far high-q tail of the distribution in Figure 3.4b. We speculate that a similar mechanism may apply to atomic cyclopentane. Indeed, thermal ring-breaking reactions typically occur in cyclopentane and methyl-cyclopentane [141], which unlike higher-symmetry cyclic compounds like cyclohexane exhibit significant bond strain.

For atomic cyclopentane, a catalyst can greatly accelerate the ring opening reaction by offering attractive binding sites. For example, noble metal surfaces and mesoporous materials can achieve some selectivity in the ring opening reaction [142–145], but the mechanism is complex and poorly understood. To investigate such catalytic reactions in colloidal cyclopentane, we assemble rings in the bulk and sediment them onto a hydrophobic surface to which the particle

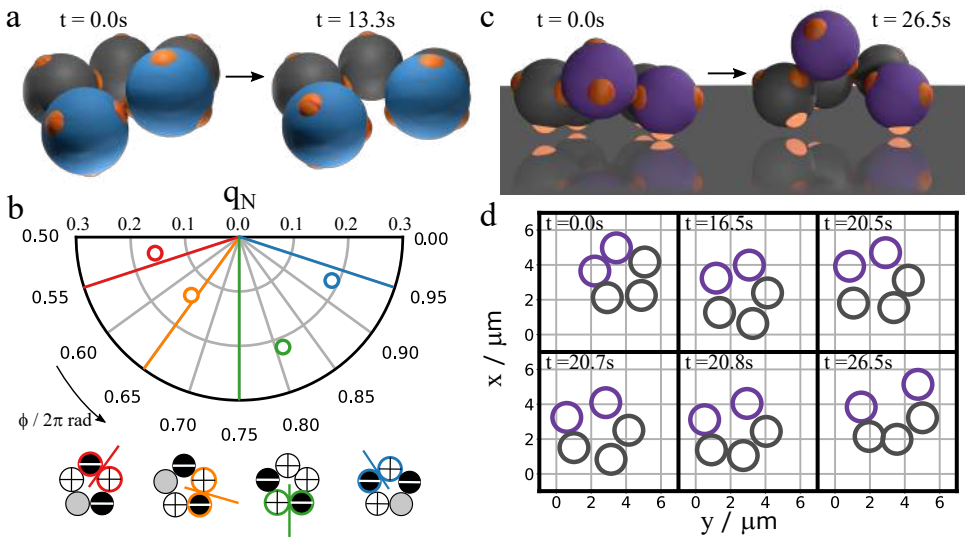

Figure 3.5 : Colloidal cyclopentane ring-opening reaction. (a, b) Thermal ring-opening of free colloidal cyclopentane. (a) Three-dimensional reconstruction of a dissociating ring just before (left) and just after breaking the bond between the blue particles (right). (b) Top: Examples of ring configurations just before breaking (circles) and corresponding breaking points (radial lines) in q-ϕ space. Bottom: Breaking points in schematic representation, with colours indicating braking position. Colour coding matches the q-ϕ coordinates above. (c, d) Catalytic ring-opening of colloidal cyclopentane on an attractive (hydrophobic) surface. (c) Three-dimensional reconstruction of the ring shown before (left) and after breaking the bond between the purple particles (right). The bright patches are attached to the surface. (d) Time sequence of the surface diffusion and eventual breaking of the bond between the purple particles of the surface-bound ring.

patches bind. We find that this greatly speeds up the ring dissociation: a few minutes after surface adsorption, a ring breaks and opens, as shown in Fig 3.5c&d. Upon adsorption, 3 to 4 particle patches bind to the substrate (highlighted in Figure 3.5c), confining the ring to the surface, and effectively freezing it in a single envelope conformation. At the same time, the ring can still move laterally and diffuse along the substrate, before it opens (Figure 3.5d). The binding-induced angular strain, together with the entropically unfavourable locking of configurations, causes the ring to break easily. The hydrophobically treated substrate serving as a catalyst thus allows direct observation of the interplay of conformations, bond geometry and surface interaction in the catalytic dissociation process. This makes our colloidal model very suitable for the study of geometric effects of catalysts, in absence of any electronic or support effects, using designed colloidal crystal surfaces or templates with defined symmetry, lattice constant and domain size. Fast confocal microscopy imaging can then give detailed insight into energies along the reaction coordinate, identifying the transition states in these catalytic processes.

3.3 Discussion

The direct observation of pseudorotation and catalytic reactions of colloidal cyclopentane offers insight into transition states in a molecular dissociation reaction. As the thermal energy $k_{\mathrm{B}}T$ is of the same order as the bond energy, the colloidal molecule corresponds to its high-temperature molecular counterpart. The ratio of 15 for the bond energy to $k_{\mathrm{B}}T$ in our experiments would correspond to a temperature of $\sim 640\,\mathrm{K}$ for atomic cyclopentane, as can be estimated from its C-C bond energy of $\sim 80\,\mathrm{kJ/mol}$. In this limit, the quantum mechanical energy spectrum of the low-frequency modes of the molecule becomes quasi-continuous, and classical behaviour is expected to emerge, suggesting that the colloidal analogue becomes a good model.

Our results highlight the importance of bond strain in the dissociation process, and suggest specific catalyst design that takes advantage of the puckering amplitude in the ring breaking process. These results pave the way to the investigation of molecular kinetics by detailed direct observation of colloidal analogues, elucidating transition states, kinetic pathways and correlations in molecular reactions [146]. The exquisite temperature control afforded by the critical Casimir

interaction creates opportunities for molecular and supramolecular colloidal design following equilibrium and non-equilibrium routes, and the investigation of dynamic assembly pathways. The demonstrated accurate binding control opens up pathways to *colloidal molecular chemistry*, in which bond-stretch and -bend potential-energy functions can be tuned by the experimentalist, and all the reactions, not only ring opening but also synthesis, homogeneous catalysis, and polymerization can be followed in real time using a conventional microscope to observe the reacting colloidal atoms.

3.4 Appendix

3.4.1 Sample Preparation and History

Particles are left to sediment to the bottom of the sample at room temperature before measurements. We choose a particle concentration such that the surface coverage is between $\phi = 0.10$ and $\phi = 0.15$ after sedimentation. We then start increasing temperature to switch on the critical Casimir attraction and assemble the structures.

In an experiment, we heat the sample to $0.04\,^{\circ}\mathrm{C}$ below the phase separation temperature of the lutidine-water mixture, inducing critical Casimir attraction between patches. The structures then grow by two-dimensional diffusion in the plane. No mixing is necessary. After several hours of equilibration, we investigate the structures using a 63x oil-immersion objective. Further details on sample preparation can be found in section 2.3.

Catalytic Conversion

For the catalytic experiments, the samples are prepared in capillaries which have been made hydrophobic using the gas silanization reaction described in section 2.3.1. In the catalytic experiments, we use patchy particle batch C in Table 2.1 because those particles sediment slower and have a larger attractive temperature range between T_{a} and T_{cx} of approximately $0.20\,^{\circ}\mathrm{C}$. Particles are left to sediment on one side of the capillaries. Then, we raise the temperature to $\Delta T = 0.10\,^{\circ}\mathrm{C}$ and flip the sample over so the particles are in free fall. In this free fall, the particles assemble into (among other things) cyclopentane. When the ring is almost at the bottom of the sample, we lower the temperature to $\Delta T = 0.17\,^{\circ}\mathrm{C}$, and observe the adsorption of the ring to the surface and its subsequent breakup using a 100x oil-immersion objective.

3.4.2 Confocal Microscopy and Particle Tracking

We image the assembled structures using confocal microscope image stacks, alternating with bright field images. To follow a colloidal molecule in time, we acquire around 100 image stacks and bright field images during a time interval of 12 minutes. The particles and patch positions are then determined using the

algorithms described in section 2.3.3. This yields an accurate 3D position vector $\mathbf{R}_j$ of each particle j of a ring.

Finally, we use an algorithm which eliminates all rings which have unrealistically high or low angles between particles to further eliminate any data with particles placed on the wrong positions, which is confirmed by manual inspection of the video

3.4.3 Pseudorotation in Polar Coordinates

We use the method by Cremer and Pople [140] to find the ring puckering coordinates for each particle configuration. This is done by expressing the positions $\mathbf{R}_j$ of the particles in a new coordinate system. In this new coordinate system, the average plane through all particles forms the xy-plane, and the z-displacement z_j is the distance of a particle from this plane.

This new coordinate system must satisfy

$$\sum_{j=1}^{5} \mathbf{R}_j = \mathbf{0} \text{ (origin set to centre of mass)} \tag{3.2}$$

meaning that the origin of the system is at the centre of mass of the five particles. We further enforce

$$\sum_{j=1}^{5} z_j = 0 \text{ (mean plane through origin)} \tag{3.3}$$

which means all z-displacement z_j in the new coordinate systems average out to zero: the mean plane must be the average of the particles. We choose the unit vector $\mathbf{l}$ going through any of the five particles as a convenient x-axis. Unfortunately, Eq. 3.2 and 3.3 do not yet yield a unique average plane through the five particles:

multiple planes can be drawn that will all satisfy the above conditions. Therefore, we further impose the conditions

$$\sum_{j=1}^{5} z_j \cos[2\pi(j-1)/N] = 0 \tag{3.4}$$

$$\sum_{j=1}^{5} z_j \sin[2\pi(j-1)/N] = 0 \tag{3.5}$$

which will fix the plane uniquely. In the case of a regular planar polygon, Eq. 3.4 and 3.5 correspond to the condition that a small displacement z_j will not lead to angular momentum. The same conditions may be used more generally for bigger displacements, and any bond lengths or angles. Also, this condition will yield the same plane irrespective of which particle is chosen as $j = 1$. Combining all these conditions, we can now determine the orientation of the mean plane for the position vectors $\mathbf{R}_j$:

$$\mathbf{R}' = \sum_{j=1}^{5} \mathbf{R}_j \sin(2\pi(j-1)/N) \tag{3.6}$$

$$\mathbf{R}'' = \sum_{j=1}^{5} \mathbf{R}_j \cos(2\pi(j-1)/N) \tag{3.7}$$

then the unit vector

$$\mathbf{n} = \mathbf{R}' \times \mathbf{R}''/|\mathbf{R}' \times \mathbf{R}''| \tag{3.8}$$

is perpendicular to $\mathbf{R}'$ and $\mathbf{R}''$. Thus, we can use $\mathbf{n}$ to define the new z-axis. Finally, the y-axis, defined by unit vector $\mathbf{m}$, can now be found by simply taking the crossproduct of $\mathbf{l}$ and $\mathbf{n}$. By linearly displacing coordinates to this new coordinate system, we can determine the ring's puckering coordinates.

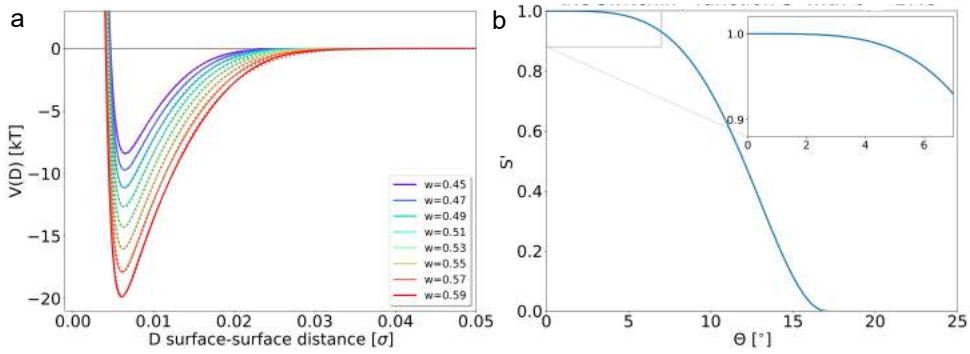

Figure 3.6 : Pair potential and switching function. (a) Pair potential of a hydrophobic isotropic particle with a radius of $0.5\,\mu\mathrm{m}$, immersed in a water/lutidine (75%vol/25%vol) solution with $1.0\,\mathrm{mM}\ MgSO_4$ is illustrated at various wetting scaling parameters w (in colour) with the fitted functions (grey dotted line). (b) The switching functions S' (Eq. 3.13) of a particle with $\Theta_p = 17.0°$.

The ring puckering amplitude q and phase ϕ for a ring of 5 particles are defined as

$$q\cos\phi = \sqrt{2/5}\sum z_j \cos 4\pi j/5 \tag{3.9}$$

$$q\sin\phi = \sqrt{2/5}\sum z_j \sin 4\pi j/5 \tag{3.10}$$

We can simply calculate the puckering coordinates from the transformed coordinates for every snapshot.

3.4.4 Simulations

The structural distribution of colloidal cyclopentane is sampled with the computational model described in Ref. [133] which is based on critical Casimir potentials [82] benchmarked onto experimentally measured chain length distributions and the bending rigidities of a dipatch particle system at various temperatures.

Here the computational model for tetrapatch particles interacting via critical Casimir interactions is presented at an off-critical binary mixture and the simulations of the conformational distribution of colloidal cyclopentane is discussed.

The Potential of the Tetrapatch Particle

The potential of the patchy particle system (Eq. 3.11) has two contributions: the pair potential V_{pair} (Eq. 3.12) acting between the colloidal particles and a gravitational potential V_{gravity}. The total interaction is a summation over the pair potentials and the gravity over N particles.

$$V = \sum_{i,j}^{N} V_{\text{pair}}(i,j) + \sum_{i}^{N} V_{\text{gravity}}(z_i) \tag{3.11}$$

$$V_{\text{pair}}(i,j) = \begin{cases} \infty, & D = r - \sigma \leq 0 \\ V_{\text{rep}}(D_{ij}) + V_{\text{C}}(D_{ij}) S'(\Theta_i) S'(\Theta_j), & D > 0 \end{cases} \tag{3.12}$$

The pair potential is composed out of an isotropic repulsion V_{rep} plus a critical Casimir attraction V_{C} only effective at the patches via a switching function S' of both particles i and j. The repulsion and attraction are only a function of the radial surface-surface distance D_{ij} between two particles with diameter σ and centre-to-centre distance r, while the switching function S' is dependent on the patch orientation with respect to the inter-particle vector.

In experiment, the tetrapatch particles and dipatch particles are synthesized from the same materials and assembled into various architectures in the same solvent: a water/lutidine (75/25%vol) binary liquid with 1.0 mM $MgSO_4$. Only the physical dimensions of the dipatch and tetrapatch particles differ. Thus, one expects that the potential of the tetrapatch particles uses the benchmarked parameters of the dipatch system, i.e. surface charge $\Upsilon = -0.10\, e\, \text{nm}^{-2}$ and scaling wetting parameter $w = 0.47$, which are material properties.

However, significant bonding of the tetrapatch particles is only observed at temperatures of $\text{d}T = T_{\text{cx}} - T \leq 0.04$ where T_{cx} is the phase separation temperature. This indicates that upon increasing the temperature and approaching $\text{d}T = 0.04$ in experiment, the potential gets stronger and the critical temperature T_{c} has not been crossed yet. This is in contrast to the theoretically predicted criti-

cal temperature at $\mathrm{d}T = 0.08^{*}$. The addition of salt to the solvent may affect the phase separation curve which leads to a shift of T_{cx}.

With the non-universal scaling constant $B = 0.765$ and wetting scaling parameter $w = 0.47$, patches of tetrapatch particles do not show significant binding at $\mathrm{d}T = 0.04$ [147]. Therefore, w is increased to ensure spontaneous formation of bonds. From an interaction strength with $w \geq 0.55$, there are colloidal cyclopentanes observed in an MC simulation at 15%area coverage including gravity. Figure 3.6a shows the pair potentials and their fit at various scaling wetting parameters w of a hydrophobic isotropic colloidal particle with $\Upsilon = -0.10\, e\,\mathrm{nm}^{-2}$, $R_p = 0.5\,\mu\mathrm{m}$, and $\mathrm{d}T = 0.04\,\mathrm{K}$ immersed in the binary liquid.

The angular dependence of the interaction strength is captured by the switching function S which is a smoothly decaying function from 1 to 0 as shown in Figure 3.6b. As the patch geometry of the tetrapatch is similar to the particles from Ref [148], we use the switching function

$$S'(\Theta_i) = \begin{cases} \frac{1}{2}\left[1 - \cos\left(\frac{\pi(\cos\Theta_i - \cos\Theta_{\mathrm{p}})}{1-\cos\Theta_{\mathrm{p}}}\right)\right] & \cos\Theta_i \geq \cos\Theta_{\mathrm{p}} \\ 0 & \cos\Theta_i < \cos\Theta_{\mathrm{p}} \end{cases} \tag{3.13}$$

where Θ_{p} is the patch arc-angle and $\cos\Theta_i = \mathbf{r_{ij}}\cdot\mathbf{p}_i/|\mathbf{r}_{ij}\cdot\mathbf{p}_i|$ is the angle between the patch vector $\mathbf{p}_i$ and the interparticle vector $\mathbf{r}_{ij}$.

The gravitational potential is a function of the mass difference between the colloidal particle and the solvent. Tetrapatch particles are synthesized from four equal spheres of polystyrene (PS) surrounding one sphere of TPM with an ideal ratio $r_{\mathrm{TPM}}{:}r_{\mathrm{PS}} = (\sqrt{8}-2)/2$ which translates into a fractional volume $\phi_{\mathrm{PS}} = 1 - \phi_{\mathrm{TPM}} \approx 0.9825$.

---

*The location of T_{cx} with respect to T_{c} calculated via $\frac{T_{\mathrm{cx}}-T_{\mathrm{c}}}{T_{\mathrm{cx}}} = \left(\frac{|c_{\mathrm{c}}-c|}{B}\right)^{1/\beta}$ where $T_{\mathrm{c}} = 33.86\,^{\circ}\mathrm{C}$ is the critical temperature, $c_{\mathrm{c}} = 0.287$ the critical (lutidine mass) fraction, $B = 0.765$ a non-universal scaling constant of the water lutidine solution without salt measured in Ref. [147], and $\beta = 0.3265$ a universal scaling constant.

Monte Carlo sampling of the Colloidal Cyclopentane Conformations

The computational system is composed of N=5 particles in a cyclopentane conformation. We sample the conformational distribution of the colloidal cyclopentane by performing 60 000 cycles of 500 000 single particle Monte Carlo steps. Bond breakage, if the critical Casimir interaction $E_{\mathrm{C}} = 0$, is not allowed as we are only interested in the conformational distribution of cyclopentane. Additionally, to mimic the experimental measurement accuracy, we add a Gaussian noise with zero mean and standard deviation of $0.1\ \mu\mathrm{m} = 0.03\sigma$ in the direction perpendicular to the wall.

The Conformational Distribution of the Colloidal Cyclopentane

Figure 3.7 shows the probability density of colloidal cyclopentane with the potential with $w = 0.55$ as function of puckering phase ϕ and amplitude q_{N} of system with and without gravity and the Gaussian noise. As observed in experiment, there is no preference for the envelope or twist conformation in any of the simulations. Thus, the puckering phase is not affected by the gravitational force acting on the colloidal particles and the measurement inaccuracy in the z-direction.

The puckering amplitude does depend on the presence of gravity and the measurement inaccuracy in the z-direction. Without gravity the maximum of the probability density $q_{\mathrm{N,max}}$ is shifted toward larger q_{N} values of approx. 0.15 compared to the experimental measurement. This means that the colloidal cyclopentane is more bend in a system without gravity. With gravity the colloidal cyclopentane is flattened and the maximum of the probability density is close to experiment $q_{\mathrm{N}} = 0.06$. The effect of the Gaussian noise is making the colloidal cyclopentane appear more bend than it actually does. This effect is mainly observed in the system without gravity. An increase of density at q_{N} values larger that $q_{\mathrm{N,max}}$ is observed which shift the complete curve.

3.4.5 Patchy Particle Assembly

We typically leave the particles to assemble at constant temperature for several hours. In Figure 3.8, we show the typical process of assembly in a sample with a mix of di- and tetra-patch particles, here at $\Delta T = 0.05$℃ and number density

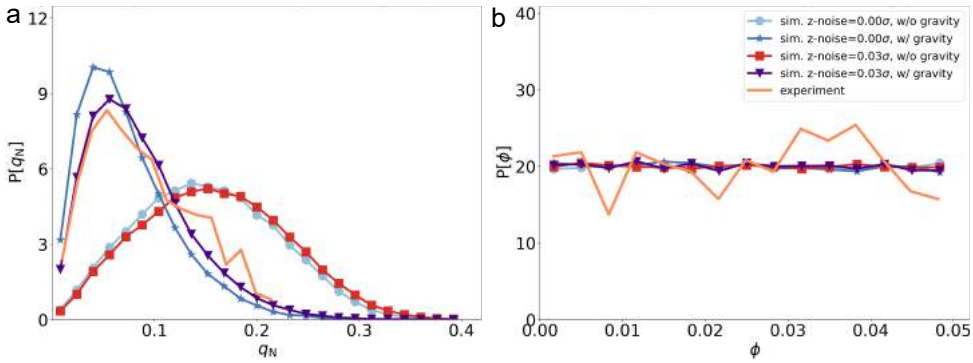

Figure 3.7 : Puckering amplitude and phase in experiments and simulations. Probability distributions of puckering amplitude q_N (a) and phase ϕ (b) in simulation and experiment. The simulations are conducted with and without adding Gaussian noise with a standard deviation of 0.03σ in the z-direction and gravity. The colour coding is equal in both graphs.

$\rho = 0.015\,\mu m^{-2}$. A bright-field microscope image of the assembled structures after 2 hours of assembly is shown in Figure 3.8a. A zoo of colloidal molecules is observed, from butanes and propanes to longer, polymer-like chains.

In Figure 3.8b we show a few snapshots revealing the assembly of colloidal methyl-cyclopentane. This process begins with butane and propane, which react to form hexane. This longer chain is now in a conformation in which it can easily form methyl-cyclopentane by reacting its first atom with the fifth atom in the chain. The molecule can also change to a conformation that reacts to cyclohexane by flipping atom 6 from the eclipsed to the staggered position. However, due to the quasi-2D nature of our system there is an energy penalty associated with this conformational change, making the formation of methyl-cyclopentane more likely.

Figure 3.8c and d show the growth of the mean cluster size and cluster size distributions. Initially, at the start of the measurement ($\Delta T = 0.26$°C), there is no clustering. As soon as we increase the temperature to $\Delta T = 0.05$°C, particles start assembling, and clusters start to grow. Figure 3.8c shows the growing average cluster size as a function of time. After 2 hours, when the measurement is stopped, an equilibrium cluster size has not been reached yet. The cluster mass distribution at different times is shown in Figure 3.8d. After 2 minutes several structures have already formed. As time continues, the slope of the distribution becomes less steep, indicating large structures start forming, although singlets are still the major

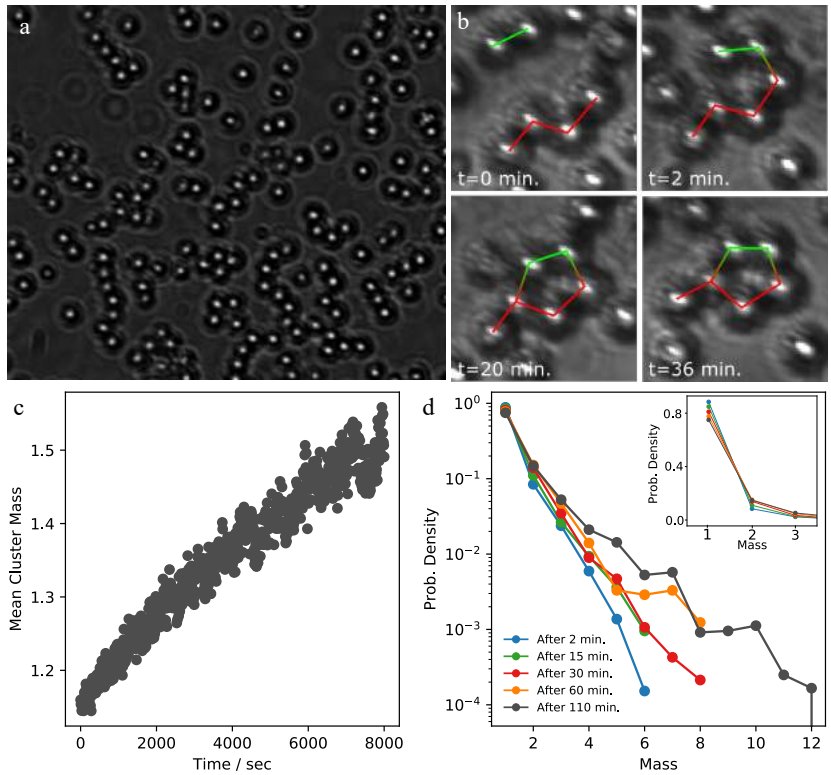

Figure 3.8 : Patchy Particle Assembly. We show a typical assembly experiment, where we set the temperature of the sample to $\Delta T = 0.05$°C. (a) Bright-field microscope image of tetra- and dipatch particles after two hours of assembly. The dimensions of the image are 97 μm × 83 μm. (b) Four bright-field microscope images showing the typical assembly of a colloidal (methyl-)cyclopentane molecule. In this particular case, we start with butane and ethane, which react to form hexane. The molecule then reacts with itself to form methyl-cyclobutane. (c) Growth of the average cluster mass with time. (d) Cluster mass distributions of the sample after 2, 10, 30, 60, and 110 minutes. The inset shows the first three data points plotted in a double-linear representation.

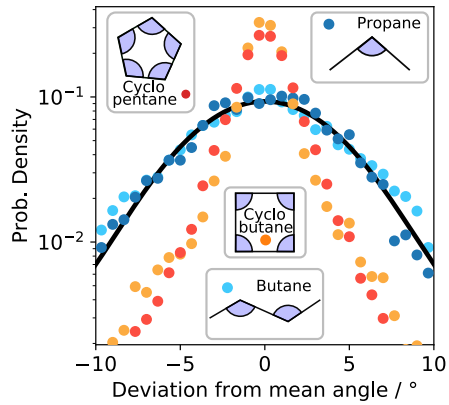

Figure 3.9 : Bond stiffness of linear and cyclic colloidal molecules. Distributions of the 2D-projected angles between the particles in different colloidal molecules: propane (navy), butane (turquoise), and cyclic compounds cyclobutane (orange) and cyclopentane (red). Note that the x-axis shows the deviation from the mean angle, $\theta_{\text{deviation}} = \theta - \langle\theta\rangle$. The insets show which angles we used to build the angle distributions shown here. The black solid line shows a Hookean fit of the angles with a spring constant of $k_{\text{bend}} = 3.4 k_{\text{B}} T \text{rad}^{-2}$.

component. This behaviour is qualitatively in line with what we expect for a growing network according to Wertheim theory [134], and will be discussed in depth in Chapter 6. Also, it appears that at later times, structures with certain number n of particles are clearly preferred, such as $n = 5$, 7, and 10. We note that here, however, cyclic and linear structures are both counted; for a distinction of cyclic structures alone, see Figure 3.2.

3.4.6 Conformations of Different Colloidal Molecules

Apart from cyclopentane, which is treated quite thoroughly in the main text, we observe many other structures. To better understand the puckering of cyclic molecules, we investigated the bond angle distributions of a range of structures, from linear to cyclic compounds, as shown in Figure 3.9. We imaged propane, butane, cyclobutane and cyclopentane using bright-field microscopy in the same sample at constant temperature ($\Delta T = 0.05$°C), and measured their 2D-projected bond angles. From repeated fast imaging, we then determined bond angle distributions for all structures, as shown in the figure. We note that this projected 2D

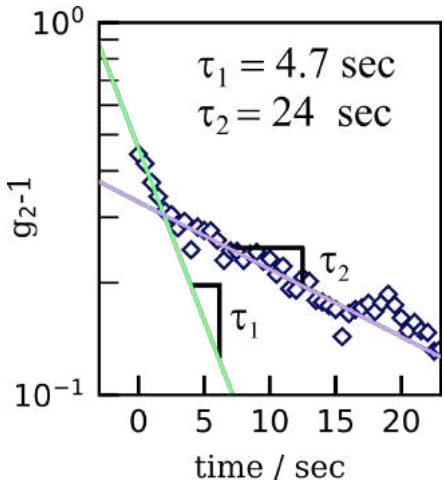

Figure 3.10 : Timescale of dynamics. Autocorrelation function of the inter-particle angles of the 2D projection of colloidal cyclopentane as a function of time in half-logarithmic representation (see Equation 3.14). Two characteristic timescales are observed: a fast one, of around 4.7 seconds, and a slower timescale of around 24 seconds.

angle differs from the 3D angles explored in the main text, but does allow us to obtain significant statistics to compare the different linear and cyclic structures in terms of their bond stiffness.

Interestingly, propane and butane, both linear structures, one with three, one with four particles, show very similar angle distributions. Both species are free to move around their preferred angle: there is no steric hindrance or confinement effect from being in a ring. In fact, by treating the particle bond as a simple spring, we can determine a spring constant from the probability distributions in Figure 3.9. The unconstrained spring constant of propane and cyclobutane is $k_{\mathrm{bend}} = 3.4 k_{\mathrm{B}} T / \mathrm{rad}^{-2}$, shown as the solid black line. In contrast, the cyclic molecules (cyclobutane and cyclopentane) show much narrower angle distributions, which we associate with the constraint of the cyclic structure. The resulting 'spring constant' of the cyclic structures is thus much stiffer than the one of the free bond angles of the linear structures.

3.4.7 Timescales

To probe the typical timescale of the ring transitioning between conformations, we acquired bright-field images of rings at a frame rate of 2 s^{-1}. In each frame,

we track the particles in a horizontal plane and determine the angles θ between the projected particle positions. We take these time-dependent angles to calculate the time autocorrelation:

$$g_2(\Delta t) = \frac{\langle \theta_i(t) \times \theta_i(t + \Delta t) \rangle_{i,t}}{\langle \theta_i(t)^2 \rangle_{i,t}}, \tag{3.14}$$

where we average over all five angles and the observation time interval $\Delta t = 0.5$ seconds. We plot a typical example of the autocorrelation of the angles over time in Figure 3.10. Generally, we find there is a fast component, τ_1, of around 9 seconds, and a slower component, τ_2, of around 25 seconds. We associate τ_1 with the diffusion of the particles, as this is approximately the expected timescale for a 3.7 μm particle to diffuse its own radius. Furthermore, we associate τ_2 with the configurational changes, i.e. pseudo-rotation of the ring, which is further confirmed by the anticorrelated motion of neighbouring particles, indicating the characteristic change between conformations while keeping the overall puckered state (see Figure 3.3e).

3.4.8 The Bending Energy of Cyclopentane

In this chapter, we have combined our experimental observations of the puckering ring with simulations for the entropic component to extract the pure bending energy of the ring as a function of q_N. To do this, we start with the free energy as a function of puckering amplitude q, given by

$$F(q) = U(q) - TS(q) \tag{3.15}$$

where U is the Boltzmann averaged energy caused by bending, T the temperature, and S the entropy. Assuming this free energy to exhibit a Boltzmann distribution in thermal equilibrium, the probability of observing a configuration with puckering amplitude q is given by

$$f(q) \sim e^{-F/k_B T} = e^{-U/k_B T} \cdot e^{TS/k_B T}. \tag{3.16}$$

Rewriting this gives:

$$\begin{aligned} ln(f(q)) &= -U(q)/k_{\mathrm{B}}T + S(q)/k_{\mathrm{B}} + C \\ U(q)/k_{\mathrm{B}}T &= -ln(f(q)) + S(q)/k_{\mathrm{B}} + C, \end{aligned} \tag{3.17}$$

with C a constant. The entropic contribution is given by the multiplicity Ω as determined from the simulations of random independent displacements, so:

$$S(q) = k_B \cdot ln(\Omega(q)) \tag{3.18}$$

$$\begin{aligned} U(q)/k_BT &= ln(\Omega(q)) - ln(f(q)) + C \\ &= ln(\Omega(q)/f(q)) + C \\ &= ln(P_0 \cdot P(q)/f(q)) + C \\ &= ln(P(q)/f(q)) + C', \end{aligned} \tag{3.19, 3.20}$$

with Ω the number of microstates, and $P(q)$ the entropic simulation observation frequency.

4 Defects of colloidal graphene

> Such simple instincts as bees making a beehive could be sufficient to overthrow my whole theory.
>
> *Charles Darwin*

Graphene has been under intense scientific interest because of its remarkable optical, mechanical and electronic properties. Its honeycomb structure makes it an archetypical two-dimensional material exhibiting a photonic and phononic band gap with topologically protected states. However, producing large defect-free single-crystal graphene layers remains a great challenge, crucially limiting its applications. Here we assemble colloidal graphene, the analogue of atomic graphene using pseudo-trivalent patchy particles, allowing particle-scale insight into graphene crystal growth and defect dynamics. We directly observe the formation and healing of common defects, like grain boundaries and vacancies. We identify a pentagonal defect motif that is kinetically favoured in the early stages of growth, and acts as seed for more extended defects in the later stages. From the bond saturation and bond angle distortions, we determine the conformational energy of the crystal, and follow its evolution through the energy landscape upon defect rearrangement and healing. These direct observations reveal that the origins of the most common defects lie in the early stages of graphene assembly, where pentagons are kinetically favoured over the equilibrium hexagons of the honeycomb lattice, subsequently stabilized during further growth. Our results open the door to the assembly of complex 2D colloidal materials and investigation of their dynamical, mechanical and optical properties.

4.1 Introduction

Two-dimensional materials have attracted intense scientific interest, both from an application and a fundamental point of view, offering applications from lightweight materials to optoelectronic devices. These materials combine extraordinary mechanical, optical and electronic properties compared to bulk materials [149–151]. The most prominent representative, graphene, consists of a monolayer of carbon atoms bonded in a honeycomb lattice. The strong covalent bonds within the honeycomb lattice make the material particularly strong while being light, while the honeycomb structure gives rise to a photonic and phononic band gap [15, 45]. Structural defects are known to be central to all of graphene's properties, enabling among others band-gap tuning in graphene-based electronic devices. However, while defects are introduced unavoidably during growth or added on purpose to tune mechanical and electronic properties, a comprehensive understanding of their formation is missing: because the sp^2-hybridized carbon atoms can arrange into a variety of polygons and structures, a coherent lattice exists even with defects, and atomic rearrangements can take many paths. Despite recent advances in direct visualization of graphene defects using electron microscopy [152–154], defect kinetics and healing remain poorly understood, and defect-free graphene highly challenging to produce.

Colloids have been used as a model system for crystallization for the better part of a century. Although colloids are several orders of magnitude larger than atoms, their phase behaviour and dynamics is governed by the same thermodynamics principles. Phase behaviour of both atoms and colloids is largely governed by thermal forces, which means we can use colloidal aggregation and crystallization as a simple model for atomic crystallization. This approach has been very successful in the past decades [31, 155, 156]. One advantage of colloidal systems is that defect formation [157] and dynamics [158] can be studied directly in real time with single particle resolution, which remains challenging in atomic systems, especially under the harsh high-temperature atomic deposition used for graphene growth. The recently-gained ability to synthesize anisotropic particles [67, 159–161], in particular colloidal particles with attractive patches that provide specific valency and bond angles, has opened a design space for assembling more complex structures such as molecule analogues [50, 51, 162].

Simulations and experiment have shown that these colloidal molecules can grow into larger assemblies, yielding rich structures ranging from the kagome lattice to

buckyball-like clusters [22, 25]. Experimentally realizing these structures however, remains challenging, as they require fine control over specifically coordinated interactions, or purposeful geometric design to block kinetically favoured nonequilibrium routes, as recently shown for the realization of colloidal diamond [24, 44]. In contrast to tetrahedrally coordinated diamond, atomic graphene relies on the trivalent coordination of carbon atoms due to their sp^2-hybridized state. Patchy particles with patches at 120° angles can mimic these covalent bonds; yet, achieving such valency and controlling these directed bonds on the scale of $k_{\mathrm{B}}T$, the thermal energy, remains challenging, but would open up the assembly of structurally complex 2D materials, and investigation of their structural and mechanical properties.

Here, we assemble colloidal graphene, the colloidal analogue of a monolayer of atomic graphene, and elucidate the kinetic pathways of crystallization and defect formation of this 2D material. We form colloidal graphene using pseudo-trivalent patchy particles adsorbed at a substrate, and directly follow the crystallization, defect formation and healing with great temporal and spatial resolution. Fine control of the patch-patch bond strength allows observation of near-equilibrium assembly in close analogy to high-temperature deposition of atomic graphene. From the number of saturated bonds and the bond strain, we determine the configurational energy of the lattice and follow its evolution during lattice rearrangement and healing. Our results reveal that the most prominent defect motif of colloidal and atomic graphene, a pentagon, is kinetically favoured in the early stages of graphene growth, and acts as seed for extended defects during subsequent growth. These results hint at the importance of the early stages of assembly in generating defect-free graphene.

4.2 Methods

In this chapter, we make use of tetrapatch particles consisting of a polystyrene (PS) bulk and fluorescently labelled 3-(trimethoxysilyl)propyl methacrylate (TPM) patches, synthesized through colloidal fusion as described in section 2.1.1, see Figure 4.1a and b [67]. Specifically, we use particle batch C in Table 2.1, with a diameter of $\sigma = 2.0\ \mu\mathrm{m}$ and a patch diameter $d_{\mathrm{p}} \sim 0.2\ \mu\mathrm{m}$; the latter is sufficiently small to allow only single patches to bind with each other (see sections 4.5.3 & 4.5.4). To induce an effective patch-patch attraction of controllable magnitude,

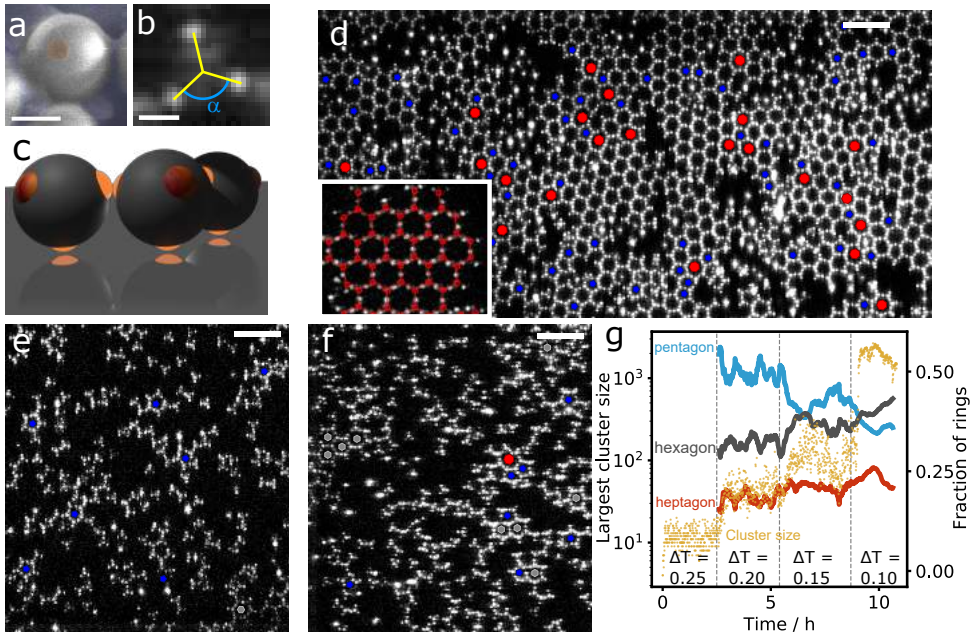

Figure 4.1 : Colloidal graphene flakes formed from trivalently coordinated particles. (a) Scanning electron microscopy (SEM) image of patchy particle, with patch highlighted in orange. (b) Confocal microscope image of patchy particle, highlighting the fluorescently labelled patches (bright spots). The projected angle between the patches is $\alpha = 120°$. Scale bars in (a) and (b) indicate 1 μm. (c) Reconstruction of the surface-bound tetramer patchy particles. One patch is attached to the surface, the remaining three patches available for bonding, making them effectively trivalent. The bonds are tilted slightly out of plane, hence deviating slightly from the ideal in-plane sp^2-like bonding. (d) Confocal microscope image of honeycomb lattice of the pseudo-trivalent particles at $\Delta T = 0.05\,°\mathrm{C}$ after 24h of equilibration. Blue and red symbols indicate pentagon and heptagon defects. Scale bar indicates 10 μm. Inset: enlarged section with particle centres highlighted in red, showing the honeycomb lattice built out of 6-membered rings. (e, f) Confocal microscope images of the pseudo-trivalent particles at $\Delta T = 0.20\,°\mathrm{C}$ (e) and $\Delta T = 0.15\,°\mathrm{C}$ (f). With increasing attractive strength, particles assemble into small clusters preferentially containing pentagons (e), which grow into larger structures, favouring hexagons (f). Scale bar indicates 10 μm. (g) Fraction of pentagons (blue line), hexagons (black line), and heptagons (red line), and largest cluster size (yellow line) as a function of time. Dashed lines delineate temperature changes. Hexagons grow at the expense of the pentagons.

we suspend the particles in a binary solvent close to its critical point. The confinement of solvent fluctuations between the particle surfaces then causes attractive critical Casimir interactions on the order of the thermal energy, $k_{\mathrm{B}}T$, tunable by the temperature offset ΔT from the solvent critical point, T_{c}, see section 2.2.2.

We use a binary mixture of lutidine and water with lutidine volume fraction $c_{\mathrm{L}} = 0.25$ close to the critical volume fraction $c_{\mathrm{L,c}} = 0.27$ [86], and solvent demixing temperature $T_{\mathrm{cx}} = 33.95\,^{\circ}\mathrm{C}$, and add 1 mM of $MgSO_4$ to screen the particles' electrostatic repulsion and enhance the lutidine adsorption of the hydrophobic patches (see section 2.2.3). The suspension is injected into a glass capillary with hydrophobically treated walls to which the particles become adsorbed via one of their patches at $\Delta T \leq 0.6\,^{\circ}\mathrm{C}$. The resulting pseudo-trivalent particles diffuse freely along the surface (see section 4.5.2), until at $\Delta T \leq 0.25\,^{\circ}\mathrm{C}$, the free patches start attracting each other, as illustrated in Figure 4.1 (see section 4.5.6). To observe near-equilibrium assembly, we slowly approach T_c in steps of $0.05\,^{\circ}\mathrm{C}$ starting from $\Delta T = 0.25\,^{\circ}\mathrm{C}$, leaving the sample to equilibrate for four hours at each step. The resulting slowly increasing patch-patch attraction mimics the slow cooling of atomic systems during high-temperature deposition processes, and ensures a near-equilibrium route to crystallization. We follow the structure and defect formation processes at the particle scale using rapid bright-field and confocal microscope imaging to track both the particles' centre of mass and fluorescent patches to determine the bond angles with their neighbours (for tracking details, see section 2.3.3).

4.3 Results and Discussion

The final assembled structure shows large flakes of honeycomb lattice, as shown in Figure 4.1d. In the lattice, each particle has 3 bonds, at 120° angle with respect to each other, resulting in the repeating 6-membered hexagonal ring motif characteristic of the honeycomb lattice of graphene, as clearly shown in the inset. Indeed, the observation of the honeycomb lattice at our colloidal particle densities is in agreement with simulations of surface-confined trivalent particles predicting the honeycomb lattice for intermediate particle densities [26]. Besides the hexagonal honeycomb motif, however, we notice the presence of 5- and 7-membered rings, pentagons and heptagons, often sitting at the boundaries of the honeycomb flakes. The crystal flakes and defects remind of those of atomic graphene grown

by chemical or physical vapour deposition. Furthermore, by analogy with atomic deposition, we observe the formation of an amorphous layer when we quench the trivalent particles to high interaction strength (see section 4.5.5), in line with the amorphous structures observed in low-temperature vapour deposition [163].

To obtain further insight into colloidal graphene growth, we follow the initial stages of assembly at low interaction strength, corresponding to high temperatures in atomic deposition. Surprisingly, many 5-membered rings form initially, as shown in Figure 4.1e, where small, open pentagon clusters are prevalent (blue dots). As the interaction strength increases, particle clusters grow, and more hexagon motifs, accompanied by heptagon motifs are observed (Figure 4.1f, grey and red dots, respectively). The dynamic evolution of the different motifs is clearly shown in Figure 4.1g, where we plot the fraction of pentagons, hexagons, and heptagons, together with the largest cluster size as a function of time. Initially, pentagons are the clear majority, while with increasing attraction, as larger clusters form, the number of hexagons grows at the expense of pentagons until they become the majority and we observe the fully grown flakes in Figure 4.1d.

4.3.1 Defects: Grain Boundaries and Vacancies

We show examples of the most prominent defect types, grain boundaries and vacancies, in Figure 4.2. The grain boundary consists of a line of alternating pentagons and heptagons bounding crystalline regions with different orientation above and below, indicated by the green dotted line in Figure 4.2a. The 'scar' of pentagons and heptagons causes a distinct shift in the orientation of the crystal: the honeycomb grains are rotated by approximately 17°. These grain boundaries are very commonly observed in colloidal graphene: the combination of 5- and 7-membered motifs makes them geometrically most compatible with the honeycomb lattice, as shown schematically in Figure 4.2b. In the ideal lattice, all bond angles are 120°. In contrast, pentagons exhibit internal angles of 108°, incompatible with the honeycomb lattice, making adjacent 6-membered rings unfavourable. Instead, the system typically forms the more favourable combination of alternating pentagons and heptagons, cancelling most of the angular mismatch, see Figure 4.2b. Hence, the presence of a pentagon facilitates neighbouring heptagons, which in turn promote neighbouring pentagons, stabilizing the grain boundary. Indeed, similar grain boundaries of alternating pentagons and heptagons are found in atomic graphene [165, 166]. Although the details

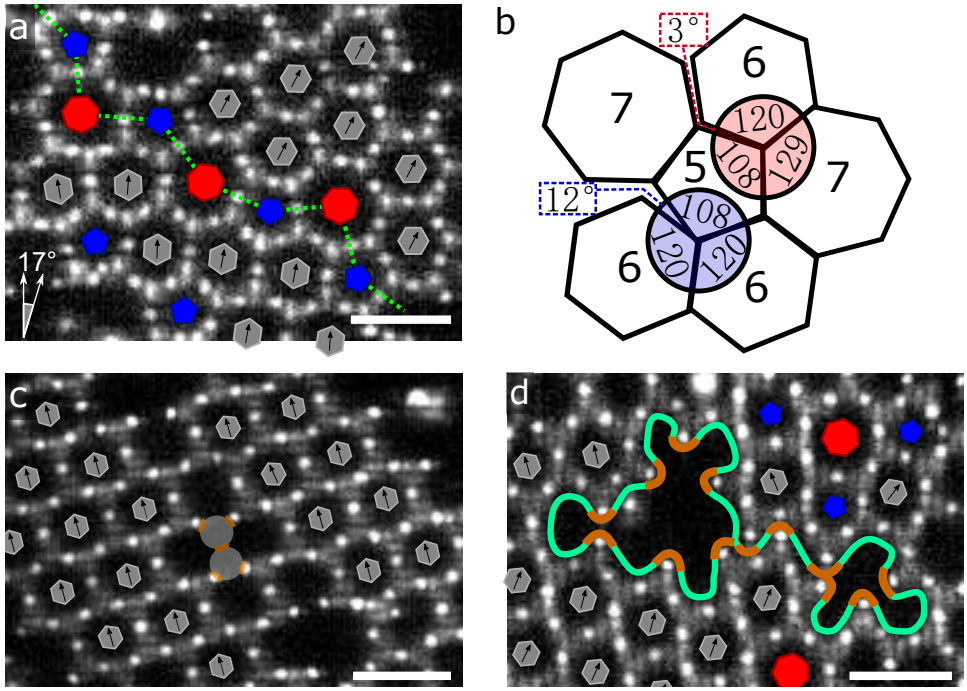

Figure 4.2 : Defects in colloidal graphene. (a) Confocal microscope image of a typical grain boundary consisting of pentagons and heptagons. Green dotted boundary separates grains rotated by $\theta \sim 17°$ with respect to each other (left lower inset), which matches observations in atomic graphene [164]. (b) Schematic indicating the compatibility of 5-, 6- and 7-membered rings. Two 6-membered rings and a 5-membered ring leave a 12° angular mismatch, while a combination of one 5-, one 6-, and one 7-membered ring leaves a mismatch of only 3.4°. (c) Confocal microscope image of a divacancy in colloidal graphene. The missing patchy particles are illustrated in grey with orange patches. (d) Confocal microscope image of a polyvacancy. The boundary of the vacancy is indicated with a green line, and the dangling bonds with an orange line segment. In all panels, 6-membered rings are indicated with grey hexagons, 5-membered rings with blue pentagons, and 7-membered rings with red heptagons. The orientation of 6-membered rings is indicated with a black arrow. All images are taken at $\Delta T = 0.05\,°\mathrm{C}$. Scale bars in (a), (c) and (d) indicate 5 μm.

of the inter-atomic attractions are different from those of the colloidal particles, the same geometric argument underlying the typical pentagonal and heptagonal motifs applies.

Vacancies indicate defects, where one or more particles are missing in the honeycomb lattice. An example of a divacancy, where two particles are missing, is shown in Figure 4.2c, while a bigger poly-vacancy is shown in Figure 4.2d. In the first case, the surrounding honeycomb lattice is not much perturbed: the crystal structure remains intact, and the orientation of the 6-membered rings does not change. In the second case, the vacancy has a large effect on the surrounding lattice; the lattice is deformed and partly collapsed upon itself.

Vacancies are of interest in atomic graphene, as they can unlock desirable material properties, like catalytic activity and improved electronic properties [167–169]. However, CVD-grown atomic graphene does not normally show vacancy defects, even though experiments show that vacancies are generated during the early stages of the CVD process [170]. Unlike the substrate-adsorbed colloidal particles, carbon atoms can approach vacancies from outside the plane during CVD growth, filling the vacancies with feedstock carbon [170]. Hence, unlike vacancies in colloidal graphene, vacancies in atomic graphene anneal in the CVD process, and irradiation or chemical treatment is used to induce them. These generated vacancies typically reconfigure to a (slightly) lower-energy structure that contains fewer dangling bonds. For instance, a divacancy can reconfigure into two 5-membered and one 8-membered ring [171]. In contrast, the divacancy in Figure 4.2c is stable and does not re-configure. We associate this with the more rigid bonds of the short-range critical Casimir interaction potential [82], making reconfigurations in colloidal graphene unlikely due to high energy barrier (see section 4.5.8) [152, 172, 173].

4.3.2 Defect Formation

To obtain insight into the origin of the defects, we follow the defect formation process more closely. Pentagons, generated early in the assembly process, can act as nucleation sites for grain boundaries, as shown in Figure 4.3a-c. The grain boundary grows from a pre-existing pentagon that forms at $\Delta T = 0.10\,^{\circ}\mathrm{C}$ (blue arrow in Figure 4.3a and b), and subsequently 'catalyses' the formation of a heptagon, as shown in Figures 4.3b and c (pink arrow). The heptagon again promotes the formation of a pentagon (orange arrow). Thus, a grain boundary of successive

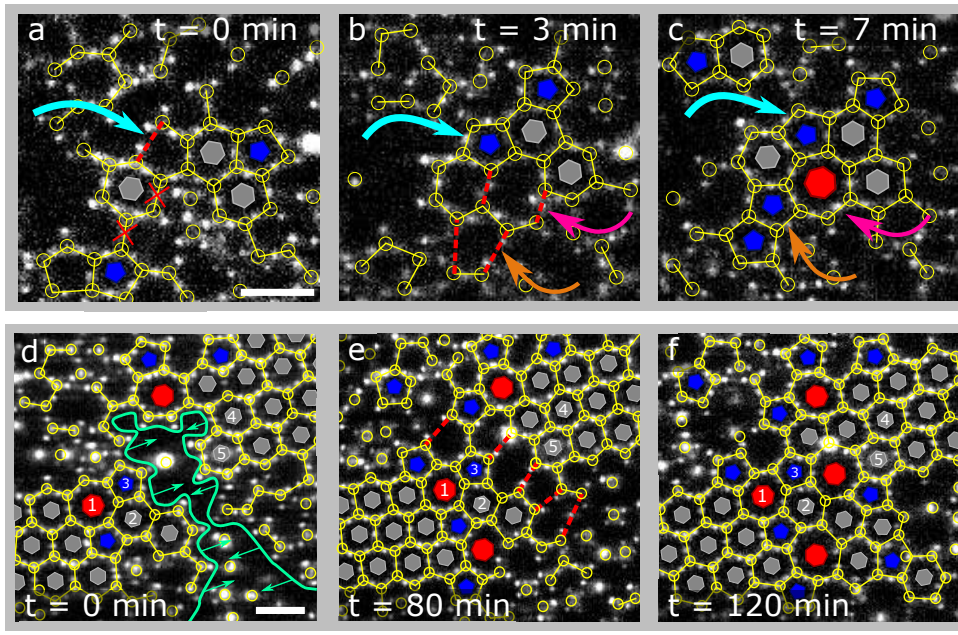

Figure 4.3 : Origin of defects of colloidal graphene. (a) - (c) Annotated confocal microscope images showing the spontaneous formation of a grain boundary. These images are taken at $\Delta T = 0.10\,^{\circ}\mathrm{C}$, where the honeycomb crystals start forming and are still small. In (a), 2 particles are about to bond, leading to the formation of a 5-membered ring at the red dotted line (blue arrow). In (b), the 5-membered ring has formed, and promotes the formation of a neighbouring 7-membered ring, indicated with the pink arrow. The 7-membered ring in turn promotes the formation of a 5-membered ring next to it, indicated with an orange arrow. In (c), we show the final structure with the blue, pink, and orange arrows indicating the *grain-boundary* that has grown spontaneously. (d) - (f) Annotated confocal microscope images showing the formation of a grain boundary through the merging of two grains. These images are taken at $\Delta T = 0.05\,^{\circ}\mathrm{C}$. Two larger grains of colloidal graphene approach each other, indicated with green lines and arrows in (d). In (e), the grains have drifted closer together. The red dashed lines indicate where particle bonds will form. The two grains fit together without leaving empty space. In (f) the two grains have merged into one, and alternating 5- and 7-membered rings form their boundary. The rings numbered 1 to 5 are the same in each frame. Scale bars in (a) and (d) indicate $5\ \mu\mathrm{m}$.

alternating pentagons and heptagons is established after 7 minutes as shown in Figure 4.3c. We hypothesize that a similar mechanism is effective in atomic graphene. While the role of pentagons in the formation of grain boundaries has not yet been reported for atomic graphene, observations of pentagon formation in early growth of atomic graphene support this possibility [174, 175]. The initial prevalence of pentagons (Figure 4.1g) favours the formation of the alternating pentagon-heptagon defect, which then remains stable. Yet, this prevalence is surprising, as it is energetically more favourable to form the equilibrium hexagonal motif. Our observations suggest that this effect is of kinetic origin (see section 4.5.7): a 5-particle ring closes before a sixth particle arrives, and subsequently remains trapped, while continuing to attempt incorporating a sixth particle. A similar kinetically favoured pathway is observed in the assembly of colloidal diamond from tetrahedral particles: 5-membered motifs are kinetically favoured, hindering the formation of the diamond lattice and making it difficult to assemble colloidal diamond [25, 44, 162]. Similarly, our results on colloidal graphene demonstrate that kinetically favoured pentagons hamper the formation of the equilibrium hexagonal motif, leading to grain boundaries that limit the growth of the honeycomb lattice.

Grain boundaries can also emerge from the merging of crystal grains as shown in Figure 4.3d-f. The system minimizes the number of dangling bonds by stitching the two crystal islands together, while reconfigurations of the misaligned grains lead to a 'scar' of pentagons and heptagons after 120 minutes (see Figure 4.3f, online video [236], and section 4.5.9). Similar processes of generating grain boundaries through the merging of crystal grains occur in atomic graphene [164, 176].

4.3.3 Defect Evolution

To elucidate the slow reconfiguration of graphene defects in more detail, we follow the graphene polycrystal over a time interval of nine hours. Snapshots of the initial configuration, and after 4.5 and 9 hours are shown in Figure 4.4a - c. The red and yellow delineated regions show examples of static and highly dynamic grain boundaries, respectively. The former shows no reorganization: any translation or rotation matches the movement of the entire crystal and the grain boundary is completely frozen. In contrast, the yellow delineated region close to the junction of multiple grains shows significant reconfiguration. The initial monovacancy, divacancy, and larger polyvacancy (Figure 4.4a) merge into a bigger polyvacancy

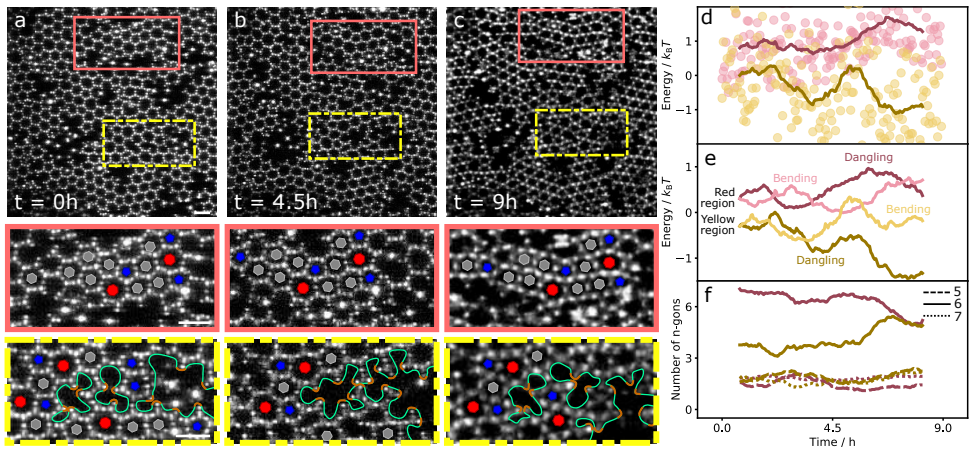

Figure 4.4 : Defect evolution in colloidal graphene (a)-(c) Top: Confocal microscope images showing a colloidal graphene polycrystal in its initial configuration (a) and after 4.5 (b) and 9 hours (c) of equilibration at $\Delta T = 0.05$°C. Red and yellow rectangles demarcate regions with static and highly dynamic grain boundaries, respectively. Bottom: Enlarged sections corresponding to the demarcated regions on top. In these sections, 6-membered rings are indicated with grey hexagons, 5-membered rings with blue pentagons, and 7-membered rings with red heptagons. The green solid lines bound poly-vacancies, the orange line segments indicate dangling bonds. Vacancies with 3 dangling bonds are typically monovacancies, vacancies with 4 dangling bonds divacancies. Scale bars in (a) correspond to 5 μm. (d) Total energy per particle computed from dangling bonds and bond bending as a function of time. Red and yellow dots and lines correspond to red and yellow enclosed regions. Dots represent individual frames, solid lines are running averages over one hour (30 data points). The energy curves are shifted with respect to each other for clarity. (e) Energy contributions from dangling bonds and bond bending to the total energy plotted in (d), running averages of 1 hour. Dark colours indicate dangling bond, and light colours bending contributions. (f) Number of pentagons (dashed lines), hexagons (solid lines), and heptagons (dotted lines) present in the two sections as a function of time. The increasing number of hexagons reflecting the closing of these motifs is in line with the decreasing dangling-bond energy in panel (e).

after $t = 4.5\,\mathrm{h}$ (Figure 4.4b), which upon further reconfiguration evolves into a monovacancy, divacancy, and a bigger polyvacancy after $t = 9\,\mathrm{h}$ (Figure 4.4c, see online video for the full process [237]). To elucidate the underlying driving force, we follow the total bond energy of the lattice over time. We include two energy contributions: energy costs due to unsaturated bonds, and energy costs due to structural distortions, where we consider only contributions from bond bending. The resulting total energy as a function of time (Figure 4.4d) reveals an energy landscape with maxima and minima, which clearly decreases for the yellow region, while it remains fairly constant for the red region. The data suggests that the yellow region slowly transitions towards a more favourable lower-energy state, while moving through the energy landscape, unlike the red region that cannot easily lower its energy.

To further elucidate the reconfiguration process, we plot the two energy contributions separately in Figure 4.4e. Both are of similar order of magnitude, while the dangling bond contribution dominates the total energy drop. Interestingly, bending and dangling-bond contributions show opposite behaviour in the first case, revealing the system's frustration (closing of bonds leads to lattice distortions and vice versa), while in the dynamic case, the two contributions decrease in parallel, leading to energetically more favourable configurations. Apparently, the interplay of lattice distortion and dangling bond saturation determines the reconfiguration process. This is further corroborated in Figure 4.4f, where we show the evolution of the number of hexagons (solid lines), pentagons and heptagons (dashed and dotted lines). The increasing number of hexagons accompanying the decreasing bending and dangling bond energy highlights the system's approach to the energetically most favourable honeycomb lattice, in contrast to the static case. The number of pentagons and heptagons changes only slightly in both cases.

The observed reconfigurations remind of the atomic reconfigurations observed at large holes of graphene using time-resolved high-resolution electron microscopy [177], where individual atoms continuously bind and unbind at the hole edges. Our time and particle-resolved observations of colloidal graphene allow detailed insight into the defect dynamics of this important 2D material, highlighting the strong dynamical nature of large vacancies and the corresponding changes in the energy landscape.

4.4 Conclusion

Trivalent colloidal particles adsorbed at a substrate form the colloidal analogue of graphene, allowing direct observation of its crystallization and defect dynamics. Fine interaction control opens near-equilibrium crystallization pathways in close analogy to atomic deposition processes of atomic graphene. We find that colloidal graphene defects originate in the early stages of crystallization from pentagonal particle motifs that are kinetically favoured over the equilibrium hexagonal motifs, further stabilized by adjacent heptagonal motifs, together forming stable grain boundaries. These results are consistent with high-resolution electron microscopy observations of atomic graphene, which however are limited to fully grown graphene, and cannot access the initial stages of crystallization. Grain boundaries and extended polyvacancies reconfigure towards lower-energy states by an interplay of dangling-bond saturation and lattice distortions, ultimately increasing the number of hexagons. Strategies for synthesizing large atomic graphene crystals tend to circumvent this issue by either generating as few graphene seeds as possible [178], or aligning graphene islands before merging [179]. While crystallization and defect dynamics in atomic graphene are ultimately governed by quantum mechanics, we expect that in the high-temperature limit studied here, where the quantum-mechanical states become quasi-continuous, our colloidal system provides a good model; yet, differences may arise from the different form of the potential and resulting differences in the bending stiffness of the colloidal and atomic bonds.

The assembly of colloidal graphene demonstrates the increasing control over bottom-up assembly of complex materials. The honeycomb lattice is of specific interest because it is the simplest metamaterial exhibiting photonic and phononic bandgap [15, 45–47], and topologically protected states. While achieving the structural complexity of macroscopic mechanical metamaterials remains still a challenge, our results demonstrate that the necessary structural motifs can be assembled using patchy particles, opening the door to microscale mechanical metamaterials [15].

4.5 Appendix

4.5.1 Sample Preparation and Measurements

Tetrapatch particles (diameter of 2.0 µm, patch diameter of approx. 0.5 µm, batch C in Table 2.1, see sections 4.5.3 & 4.5.6) are dispersed in the regular binary solvent of 25% 2,6-lutidine (≥ 99.0%, Sigma Aldrich) and 75% milliQ water with 1 mM $MgSO_4$ (≥ 99.5%, Sigma-Aldrich), as described in section 2.2.3. The particles are washed several times in the water-lutidine mixture. The resulting particle dispersion is injected into a silanized hydrophobic glass capillary and sealed with teflon grease (for full preparation see section 2.3.1).

Particles are left to sediment to the bottom of the sample at room temperature before measurements. We tilt the sample slightly during sedimentation, so a small density gradient is present in the sample. We then heat the sample to approximately 33.35 °C ($\Delta T \approx 0.6$ °C), which causes one of the particle patches to attach to the sample wall. For heating, we use a well-controlled temperature stage in combination with an objective heating element, as described in section 2.3.2.

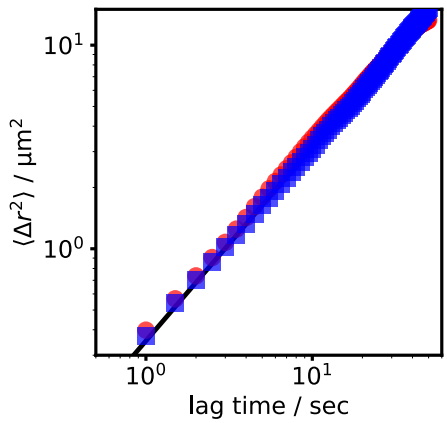

Figure 4.5 : Mean square displacement (MSD) of particles bound to the surface. Red circles indicate $\Delta T = 0.60$ °C, blue squares $\Delta T = 0.05$ °C. The MSD can be fitted using the equation $\langle r^2 \rangle = 4D \cdot t^n$, where D is the diffusion coefficient, t is the lag time, and n is the exponent. In an ideal system of free diffusion, $n = 1$. The black solid line is a fit of our data, yielding a diffusion coefficient $D = 0.88\,\mu m^2\,s^{-1}$ and $n = 0.95 \pm 0.05$.

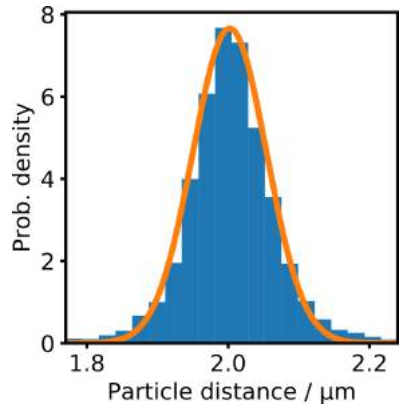

Figure 4.6 : Particle size distribution. Probability distribution of inter-particle distances between our particles. The red line indicates a normal distribution with average particle diameter 2.00 µm and standard deviation $\sigma = 0.05$ µm.

In an experiment, we typically heat a sample to a certain ΔT below the phase separation temperature of the water-lutidine mixture, inducing critical Casimir attraction between patches. The structures then grow by two-dimensional diffusion in the plane. No mixing is necessary. We investigate the structures as they form using a 100x oil-immersion objective, and image the assembled structures using confocal microscope image stacks, sometimes alternating with bright field images. The particle locations are tracked via the network-based approach described in section 2.3.3.

4.5.2 Diffusion of Particles Bonded to the Surface

To check the influence of the surface attraction on the mobility of the particles, we determined the mean square displacement of particles at the glass at $\Delta T = 0.05\,°\mathrm{C}$ and $\Delta T = 0.60\,°\mathrm{C}$, see Figure 4.5. These temperatures correspond to the extreme cases of maximal critical Casimir attraction explored, and minimal Casimir attraction required for the particles to adsorb at the surface. Nevertheless, the mean-square displacement of the particles overlap, suggesting negligible influence of the attraction on the mobility: we observe a power-law behaviour with slope ~ 1, as expected for free diffusion, and with diffusion constant $D = 0.88\,\mu\mathrm{m}^2\,\mathrm{s}^{-1}$. Furthermore, the two different attractions investigated show the same diffusion constant within error bars. Apparently, the stronger

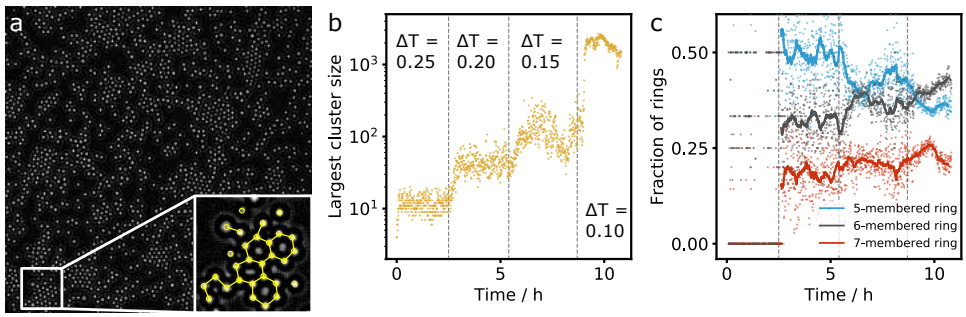

Figure 4.7 : Assembly of patchy particles We assemble particles by performing a step-wise temperature ramp: we start at 33.70 °C ($\Delta T = 0.25\,°\mathrm{C}$). Every 2.6 h, we increase the temperature (equivalent to decreasing ΔT) by 0.05 °C. (a) Bright field microscopy image of assembled particles after approx. 17 hours, at $\Delta T = 0.05\,°\mathrm{C}$. Most particles are part of a small structure. The inset shows that particles are ordered hexagonally. (b) We follow the size of the largest cluster during a temperature ramp. Dashed vertical lines indicate temperature changes. (c) In the same ramp, we track the fraction of rings that are pentagons (blue), hexagons (grey), and heptagons (red) as a function of time. Dots show data for individual frames, and solid lines show the moving average over 10 minutes (20 data points). Initially, there are no/very few rings, but as ΔT becomes smaller, larger structures, including rings are formed. At $\Delta T = 0.20\,°\mathrm{C}$, the majority of rings is pentagons. However, with decreasing ΔT, hexagonal rings take over.

attraction of the particles to the wall does not influence the particles' diffusion through interaction with the wall via hydrodynamic effects or friction.

4.5.3 Particle Size

The effective particle diameter can be determined directly from assembly experiments. We determine the inter-particle distances between particles in the honeycomb lattice. In an assembled structure, the centre-to-centre particle distances of bonded tetramer particles should correspond to twice the particle radius plus twice the patch height plus twice the (short) interaction range, as described in section 2.1.2. The mean of the inter-particle distance distribution at $2.00\,\mu\mathrm{m}$ reflects the effective particle size as estimated from SEM (see Figure 4.1a), and a standard deviation of $\sigma = 0.05\,\mu\mathrm{m}$.

4.5.4 Patchy Particle Assembly

To assemble the particles near-equilibrium, we slowly increase the temperature in steps of $0.05\,^{\circ}\mathrm{C}$ starting from $\Delta T = 0.25\,^{\circ}\mathrm{C}$, waiting at each temperature for 4 hours. This way, the system has time to adjust to the new attractive strength and acquire a near-equilibrium state. In Figure 4.7, we show the typical process of assembly. A bright-field microscope image of the system at a low density after approx. 17 hours of assembly is shown in Figure 4.7a.

To follow network formation, we perform a ramp (increasing temperature by $0.05\,^{\circ}\mathrm{C}$ every $2.6\,\mathrm{h}$) and track the particles as assembly progresses. The size of the largest cluster as a function of time is shown in Figure 4.7b. Clearly, at every temperature jump, the cluster size grows rapidly, and subsequently plateaus at an equilibrium cluster size. At $\Delta T = 0.25$°C, the largest cluster only consists of approx. 10 particles, while after temperature increase to $\Delta T = 0.10$°C, we obtain large clusters of over a thousand particles, containing practically all particles in the field of view.

We compare the relative amounts of ring motifs in Figure 4.7c. Initially, there are no, or very few rings. Starting from $\Delta T = 0.20$°C, pentagons, hexagons and heptagons start to form, with the majority being pentagons. As the attraction increases (ΔT decreases), the number of 5-membered rings drops compared to the number of hexagons. At $\Delta T = 0.10$°C, hexagons become more common than pentagons. The fraction of 7-membered rings remains closely constant over time and temperature.

To study the formation of the patchy particle network in more detail, we determine the equilibrium cluster mass distribution at different ΔT, as shown in Figure 4.8a. At low attraction, the distribution is cut off at small cluster mass. As the attraction increases (ΔT decreases), the mass cut-off moves to the right, indicating formation of larger structures, and eventually, at $\Delta T = 0.1$°C, the distribution assumes a power law, indicating percolation of the assembled structure across the plane. This behaviour is qualitatively in line with what we expect for a growing network of patchy particles [134].

We also determine the diameter of the assembled structures, and show a contour plot of diameter frequency as a function of mass in Figure 4.8b. Initially, at low cluster mass, the diameter increases with a power of 1, indicating growth of linear structures. At higher mass, the diameter increases with the lower power of $1/2$, indicating the growth of two-dimensional structures.

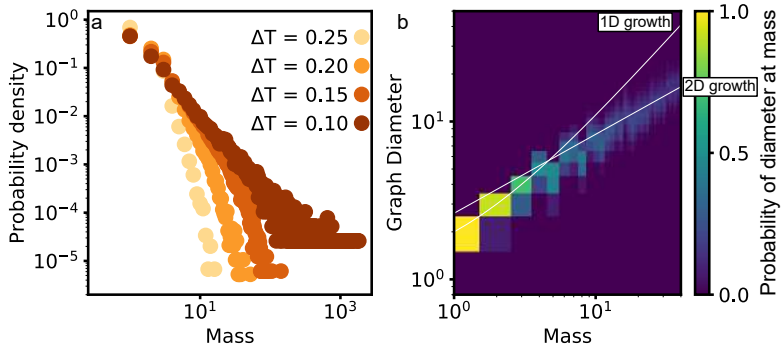

Figure 4.8 : Networking. (a) shows the cluster mass distribution of a structure at four different ΔT. As we increase the attractive strength between patches, the clusters that are formed are typically larger. (b) Probability of finding a graph diameter as a function of mass. Initially, clusters grow linearly, resulting in growth with power 1. As two-dimensional morphologies become available, 2D growth dominates and the power decreases to $1/2$.

The transition to the power-law slope $1/2$ is thus related to the transition from chains to closed clusters: for masses below 4, the 'cluster' grows as a linear chain, whose length grows linearly as particles are added. When the clusters grow larger, 2D morphologies become available, like rings, branched chains, and eventually the colloidal graphene lattice. This leads to a transition towards power-law slope of 2, consistent with regular 2D growth. Interestingly, this general scenario is robust, and the evolution of the diameter-mass distribution is largely independent of the density, attraction, and other experimental details of the experiment.

4.5.5 Fast quenching to Large Attractive Strength

Normally, we slowly increase the temperature of the system in small, slow steps, waiting at each temperature for four hours, to ensure we observe equilibrium conditions. When we do not do this, and instead heat the system from unattractive ($\Delta T = 0.40$℃) to strongly attractive ($\Delta T = 0.05$℃), we obtain an amorphous structure, see Figure 4.9. The formation of such an amorphous structure is in line with our expectations: a very similar process occurs in any other colloidal assembly process, and indeed in atomic systems as well when a fast quench is applied.

Figure 4.9a shows an interesting amorphous structure; although there is no clear order, the structure is still very open, and forms rings. The radial distribution

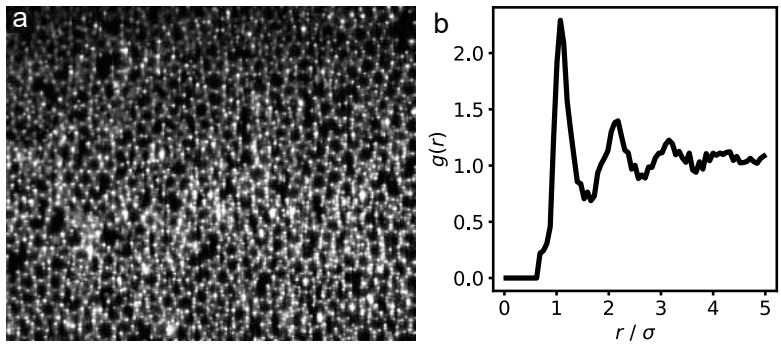

Figure 4.9 : A deep quench leads to an amorphous solid. (a) Confocal snapshot of pseudo-trivalent particles frozen into an amorphous solid state after a quenched to high attractive strength. The radial distribution function of this frozen state is show in (b).

function, plotted in panel b of the same Figure, corroborates this observation: there are clearly distinguishable peaks at short range, but these disappear at longer ranges.

4.5.6 Radial and Bending Potential of a Patchy Particle

The critical Casimir potential is short ranged, its magnitude and range are set by the temperature offset $\Delta T = T - T_c$ to the critical temperature, T_c. Further factors that determine the magnitude of the potential are the absorption preference of the surfaces (particle patches, glass surface), and the composition of the binary solvent, as detailed in section 2.2 [82]. By formulating the critical Casimir potential model presented in [82] for patchy particles and benchmarking it onto our patchy particles as shown in [133], we arrive at the attractive potentials shown in Figure 4.10a. These potentials are valid for ideally opposing patches (no bond bending strain), which is not the case here. Due to the glass-bound patch fixed vertically and the tetragonal patch arrangement, there is always a bonding angle of approximately $60°$ between the patches in the vertical plane (see Figure 4.1c). Since this bonding angle is the same for each particle, it equally reduces the bond energy between all particles. Our experiments mostly take place at $\Delta T = 0.05\,°\mathrm{C}$, which means the bonding energy of particles is approximately $15 k_B T$.

The bond-bending potential is harder to estimate theoretically, but can be determined from experimental measurements. By following three bonded particles

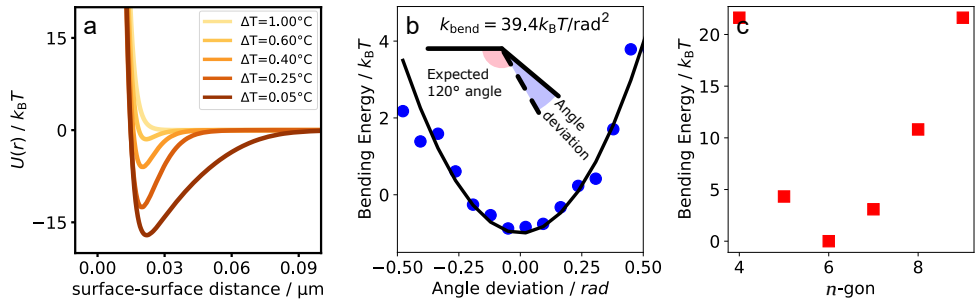

Figure 4.10 : Bond energies of Patchy Particles (a) Approximate radial interaction potentials generated by modelled data benchmarked onto experiments [133]. (b) The experimentally determined bending potential (blue circles) between 3 patchy particles at $\Delta T = 0.05\,^{\circ}\mathrm{C}$. The black solid line is a simple Hookean fit, which assumes a simple spring: $U_{\mathrm{bend}} = \frac{1}{2} k_{\mathrm{bend}} \theta^2$. (c) The bending energy in a regular n-membered ring.

and tracking the fluctuations of their bond angles, we can determine the bending energy by assuming a Boltzmann distribution. The resulting bending energy as a function of angle, determined from the probability distribution of bond angles, is shown in Figure 4.10b. The shape of this potential can be fitted with a parabola assuming a harmonic potential (Hooke's law). This leads to a bending stiffness with a force constant of $39.4 k_{\mathrm{B}} T \mathrm{rad}^{-2}$.

With this bending stiffness, we can now also determine the energy associated with the bending strain of different n-membered rings ('n-gons'), assuming equal distortion of all bond angles, as shown in Figure 4.10c. As expected, the bending energy vanishes for hexagons whose inner bond angles match that of the patchy particle. Rings with more or less particles, however, exhibit significant bond bending energy as the inner bond angle deviates from the ideal one. For pentagons and heptagons, the bending energy is only between 4 and $5 k_{\mathrm{B}} T$; thus, despite the bending energy cost, pentagons and heptagons are likely to form, which is indeed what we observe.

4.5.7 Energy of Ring Formation

To illustrate the kinetic pathway that leads to the formation of pentagons rather than the equilibrium hexagon motif, we follow a chain of five particles as it closes into a pentagon and tries to open again to form the hexagon at $\Delta T = 0.15\,^{\circ}\mathrm{C}$. We track the particles over time and determine the total energy of the particles in the

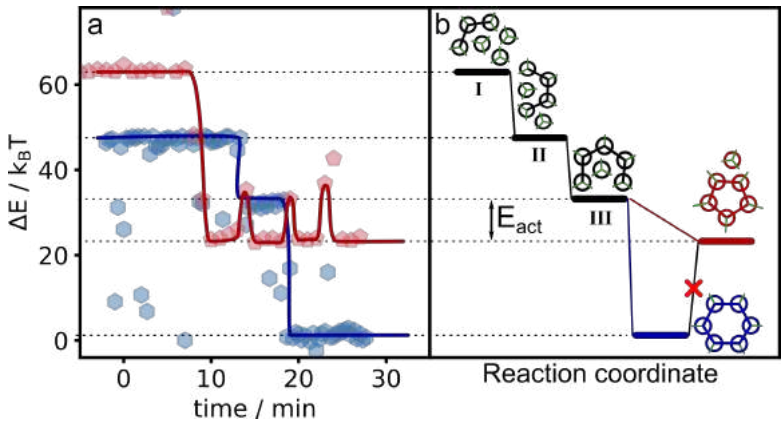

Figure 4.11 : Energy of pentagon and hexagon formation. (a) To illustrate the energetics of a ring closing reaction, we follow two linear chains that will end up as a pentagon (red) and a hexagon (blue) in the assembly process. For each snapshot, we calculate the bending energy and the dangling energy to obtain the total energy and plot it. We set the energy of a closed 6-membered ring to 0, and the other energies relative to that. The solid lines are a guide for the eye. In (b), we show the 5 intermediate structures and their relative energy levels.

pentagon as determined from their bond angles, and saturation of bonds. Hence, the energy is determined in the same way as in Figure 4.4d, that is, we use the sum of the bending energy (using the force constant determined in Figure 4.10) and the dangling bond energy of the particles involved in the assembly. We also determine the corresponding energy for the formation of a hexagon for comparison. We plot both energy traces as a function of time in Figure 4.11a. Here, the energy of the ideal 6-membered ring is set to $0k_{\mathrm{B}}T$ as a convenient orientation point.

In Figure 4.11b we show the expected energy levels of five different structures we observe in the movies: 3 particles bonded in an open chain (labelled I), 4 particles bonded in a chain (II), 5 particles bonded in an open chain (III), and the closed 5-particle (pentagon, red) and 6-particle rings (hexagon, blue).

Initially, the three bonded particles have energy of approximately $62k_{\mathrm{B}}T$ (structure I). The observed small energy fluctuations are the result of bond-bending due to thermal fluctuations. After 8-minutes, first a fourth particle, and subsequently a fifth particle binds, after which the ring almost immediately closes into a pentagon. The energy drops via the corresponding intermediate values to $\sim 23k_{\mathrm{B}}T$, corresponding to the formation of the pentagon. The process is fast, and the

intermediate states II and III are only observed for a single frame each. After the energy drop, the pentagonal ring opens and closes a few times to go back to the open structure III; however, because no sixth particle is in the correct position to bind, the ring closes before a sixth particle can be incorporated. This way, the pentagon remains metastable.

In the case of hexagon formation, the observation starts with structure II. Now, when the fifth particle binds after 15 min, the structure remains in the open state (III); at this point, either a pentagon or a hexagon can form, as is indicated in panel b. This time, another particle is available and binds, and the ring closes into a hexagon after 20 min. This is accompanied by a significant drop in energy to the ground state.

The two examples illustrate in detail the energetic pathway that groups of particles can take to form a ring structure, and are reminiscent of molecular equilibrium reactions. Initially, when structure III is formed, it is very likely that a pentagon forms shortly after, because this path is energetically favourable though it does not lead to the energetic ground state. Formation of the hexagon requires a 6th particle being available for bonding. Once a pentagon has been formed, an activation energy barrier $E_{\mathrm{act}} \sim 10 k_{\mathrm{B}} T$ needs to be overcome to open the ring so that another attempt at reacting to a hexagon can occur. If no particle is available, the ring will close again. Several of these attempts are clearly seen in the energy trace of the pentagon (red) in panel a, where the energy jumps to the level of the open ring, but immediately drops back down to that of the closed ring. In this case of an isolated ring, such attempts occur frequently. However, when the ring is embedded in a larger structure, E_{act} can become much bigger due to multiple bonds that need to be broken, to an extent where it is virtually impossible, and the system freezes.

4.5.8 Energy of Defects in Atomic and Colloidal Graphene

As discussed in the main text, not all defects found in atomic graphene are present in colloidal graphene. In this section, we look at a few common defects in atomic graphene, and calculate how their energies compare to the colloidal analogue, based on the force constants determined in Figure 4.10a and b. Although these force constants will only yield an approximate energy, they illustrate why certain defects are not present in colloidal graphene where we might expect them.

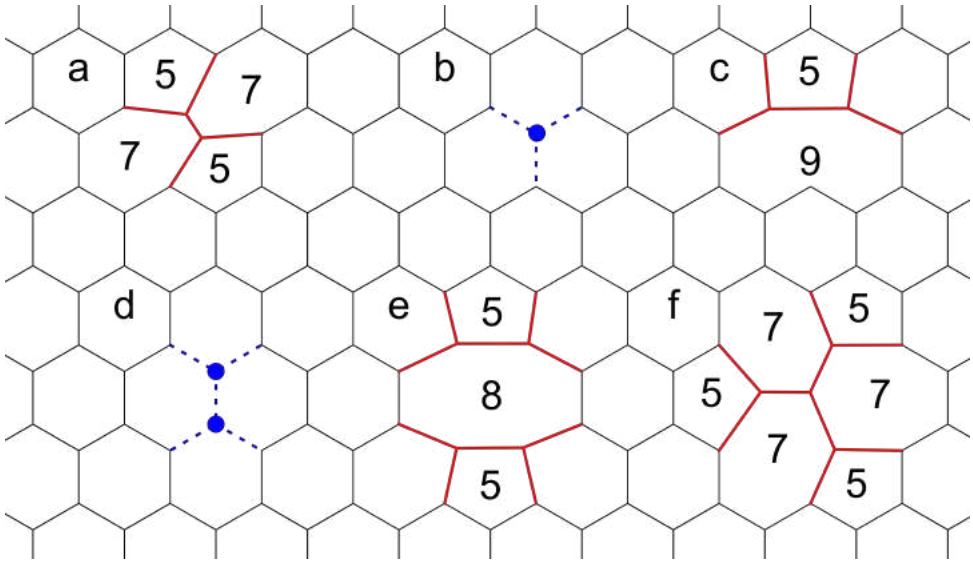

Figure 4.12 : Schematic structure of several defects in the honeycomb lattice. The different defect types are labelled a-f in the lattice. (a) shows a Stone-Wales defect, caused by a particle pair rotating 90°, resulting in two 5-membered rings and two 7-membered rings. (b) a symmetric single vacancy. One particle is missing from the lattice, which means there are 3 dangling bonds. (c) a monovacancy reconfigured into a 59 defect. This reconfiguration leaves only 1 dangling bond, but does have stretched bonds and strained bond angles. (d) a symmetric divacancy. Two particles are missing from the lattice, resulting in four dangling bonds. (e) a divacancy reconfigured into a 585 defect. This results in the elimination of all dangling bonds, in exchange for strained bond angles and stretched bonds. (f) a divacancy reconfigured into a 555-777 defect. Like the 585 defect, all dangling bonds are removed, but in exchange for strained bond angles and stretched bonds. Red lines indicate strongly deformed bonds, blue dots and dashed lines indicate missing particles and bonds. All these defects' energies of formation are given in Table 4.1.

Energy of Stone-Wales Defects

The Stone-Wales defect is a very common type of defect in graphene. It is essentially caused by a particle pair turning 90°, leading to the formation of two 7-membered and two 5-membered rings, shown schematically in Figure 4.12 (defect a). The defect is never observed in colloidal graphene. Using the bond bending and stretching energies determined from Figure 4.10a and b, we determine the energies of formation of the Stone Wales defect in colloidal graphene and compare it to the energy in atomic graphene. We estimate that in colloidal graphene, the defect imposes an energy penalty of $21 k_\mathrm{b} T$ relative to the regular lattice, which is a very significant penalty. On top of that, to reach this state, a rather large activation energy is necessary to break four particle bonds. Therefore, the Stone-Wales defect is very unfavourable in colloidal graphene, and we do not observe it.

Energy of a Single Vacancy

Single vacancies are generally understood to exist in graphene in two distinct ways, the symmetric monovacancy and the 59 (or 'reconfigured') monovacancy, shown in Figure 4.12 (defects b and c) [180]. In atomic graphene, a reconfigured vacancy has only a marginally smaller energy to the symmetric one (only $0.2\,\mathrm{eV}$), so there is a small driving force for reconfiguration, see Table 4.1. The energy difference is small because the crystal lattice around a reconfigured vacancy needs to be deformed, which balances any energy gains due to fewer dangling bonds [181]. Compared to atomic graphene, the energy penalty of symmetric single vacancies in colloidal graphene is much lower than the penalty for forming the 59 defect, see Table 4.1. This indicates that this defect is unlikely to occur in colloidal graphene, which matches our observations.

Energy of a Double Vacancy

Double vacancies exist in the honeycomb lattice in three configurations, the symmetric divacancy (Figure 4.12, defect d), the 585 divacancy (Figure 4.12, defect e), and the 555-777 divacancy (Figure 4.12, defect f). Both the 555-777 and the 585 defects have significantly lower energies compared to the symmetric divacancy in the atomic case, reflected in their ubiquity in defected graphene [182]. However, in the colloidal case, the energies of the reconfigured configurations are very similar to the symmetric divacancy. In fact, the 585 defect exhibits a slightly lower

energy than the symmetric defect. Nevertheless, we do not observe this defect reconfiguring, likely because of the high activation energy such a reconfiguration would need to overcome.

In general, larger vacancies in colloidal graphene have a lower energy penalty for reconfiguration to a state with fewer or no dangling bonds. Activation energies are similarly easier to overcome in larger vacancies. Therefore, large vacancies are expected to reconfigure to some lower energy state, as we can observe in for instance the yellow region of Figure 4a (main text), while small vacancies do not.

4.5.9 Merging of Grains

When multiple crystal grains meet during assembly, they will attempt to merge into one bigger grain to minimize the number of dangling bonds. If the two crystals are aligned, the two crystals can be merged easily, resulting in one bigger crystal with no defect. This 'seamless' merging has been mentioned in the main text, and we provide an example in Figure 4.13. Four different crystals meet and form one bigger grain. The red and blue grains merge, and form a new 6-membered ring at their interface. The combination of yellow, green and blue also yield 6-membered rings. Yellow and green are both small structures with no or a few closed rings, and are therefore more flexible with regard to their orientation. The creation of a nice, 6-membered ring is therefore more likely.

Table 4.1 : Formation energies of several commonly observed defects in atomic graphene. The formation energies of common defects in atomic and colloidal graphene are compared. The energies of colloidal graphene defects have been estimated based on particles positions found in atomic systems, so represent a rough estimate.

Defect type	Type of restructuring	$E_{\text{formation}}$ relative to HC lattice		Refs used
		Atomic case (eV)	Colloidal case ($k_{\text{B}}T$)	
Cluster	Regular HC	0	0	-
	Stone-Wales	4.8	21	[183, 184]
Monovacancy	Symmetric	8	45	[185]
	59	7.75	105	[181]
Divacancy	Symmetric	10.7	60	[185]
	555-777	7.5	63	[171, 186]
	585	8.4	55	[171, 186]

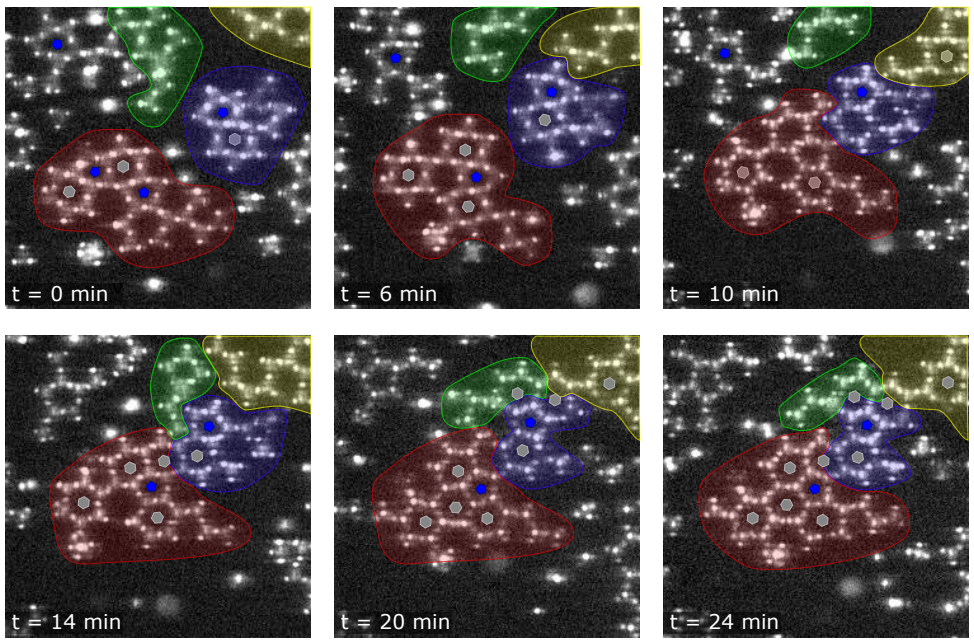

Figure 4.13 : Four crystal grains merge into one. Confocal snapshots of the 'seamless' merging of 4 crystal grains into one. Each separate grain is colour coded for the situation at $t = 0$ min.

5 Phases of surface-confined trivalent particles

> Chaos is merely order waiting to be deciphered.
>
> *José Saramago*
> The Double

In the previous Chapter, we have studied the assembly of pseudo-trivalent patchy particles into colloidal graphene. Here, we further elucidate the complex phase behaviour of these particles: besides the honeycomb phase, we observe an amorphous network phase and a triangular phase. Structural analysis is performed on the three condensed phases, revealing their shared structural motifs. Using a combined experimental and numerical simulations approach, we elucidate the origins of these phases and construct the phase diagram of this system. Using appropriate order parameters, we accurately determine coexistence lines in the phase diagram. Our results reveal the rich phase behaviour of the relatively simple patchy particle system, and open the door to a further joined simulation and experimental exploration of the full patchy-particle phase space.

5.1 Introduction

Colloidal particles are an ideal system for studying the assembly of complex materials. Despite their apparent simplicity, colloidal particles can assemble into complex structures, sometimes even mimicking atomic materials, while still being easily studied using simple scattering or microscopy methods [9]. Modern synthesis methods can go far beyond the classic isotropic colloidal sphere, endowing particles with special properties like specific particle shape and valency [19, 187, 188]. A subfield of colloidal assembly that has grown especially prominent over the past decade is the study of so-called patchy particles. A patchy particle is a colloid decorated with patches of a different material than the bulk; the patches are typically used to induce specific attraction to other patches, and thus to steer the assembly towards specific phases. Simulations and theoretical studies have revealed a wealth of structures that even relatively simple patch geometries can assemble into [23, 25, 189].

In the past, probing patchy particle assembly was performed largely through simulations, due to the challenge of synthesizing these particles bottom-up and introducing and controlling the anisotropic interactions. However, recent advances in colloid chemistry and new experimental strategies have made possible the production of more complex geometries of patchy particles and the study of their assembly [67, 190]. Experimental realization of reversible patch-patch bonding is still challenging, but opens the door to many complex structures, analogues of atomic compounds and beyond [15, 61, 191]. One way to realize selective patch-patch attraction of tunable magnitude is through critical Casimir interactions that depend on the solvent affinity of the particle surfaces [131, 192]. The critical Casimir force arises in binary solvents close to their critical point when the confinement of solvent fluctuations between the particle surfaces causes an effective attractive force on the order of the thermal energy, $k_{\mathrm{B}}T$, tunable by the temperature offset ΔT from the solvent critical point, T_{c}.

It is tempting to think of the assembly of patchy particles as simple binaries: either patches are not attractive and do not assemble, or patches are attractive, and assembly starts. Reality is fortunately much more interesting; simulations reveal that patchy particles often have rich phase behaviour, and equilibrium structures do not only depend on particle geometry, but also on patch attractive strength and particle density [25, 26, 193]. Although hints of complex phase behaviour

are sometimes reported in experimental work [27], it has never been the primary object of study.

In this work, we experimentally explore the phase diagram of surface-confined, pseudo-trivalent particles that interact via critical Casimir forces. The critical Casimir force allows us to finely adjust the attraction between particles, enabling easy access to the full range of the phase diagram. We observe the formation of three structurally distinct condensed phases: the honeycomb lattice, an amorphous network, and the so-called triangular phase. The honeycomb lattice has been studied comprehensively in Chapter 4, but the less intuitive amorphous and triangular phases have never been observed experimentally. We elucidate the basic morphological motifs of the three condensed phases and reveal how the phases are structurally related. Finally, we use the bonding state and typical lattice distances as structural order parameters to pinpoint the phase transition between the phases. Our results reveal that simple surface-confined trivalent particles display a surprisingly complex phase diagram, highlighting the rich phase behaviour even very simple patchy particles can display. Our results open the door to a larger effort towards a joined simulation and experimental exploration of the full patchy-particle phase space.

5.2 Methods

In this chapter, we make use of a system similar to the one described in Chapter 4. We use particle batch C from Table 2.1: tetrapatch particles consisting of a polystyrene (PS) bulk and fluorescently labelled 3-(trimethoxysilyl)propyl methacrylate (TPM) patches, with a diameter of $\sigma = 2.0\,\mu\mathrm{m}$ and a patch diameter $d_\mathrm{p} \approx 0.2\,\mu\mathrm{m}$, see Figure 5.1a&b [67]. We suspend the particles in a binary mixture of lutidine and water close to its critical point to induce an effective patch-patch attraction. The confinement of solvent fluctuations between the particle surfaces then causes attractive critical Casimir interactions, tunable by the temperature offset ΔT from the solvent critical point, T_c, see section 2.2.2.

We use a binary mixture of lutidine and water with lutidine volume fraction $c_\mathrm{L} = 0.25$ close to the critical volume fraction $c_\mathrm{L,c} = 0.27$ [86], and solvent demixing temperature $T_\mathrm{cx} = 34.12\,^\circ\mathrm{C}$, and add 1 mM of $MgSO_4$ to screen the particles' electrostatic repulsion and enhance the lutidine adsorption of the hydrophobic patches (see section 2.2.3). The suspension is injected into a glass

capillary with hydrophobically treated walls to which the particles become adsorbed via one of their patches at $\Delta T \leq 0.7\,^{\circ}\mathrm{C}$. The resulting pseudo-trivalent particles diffuse freely along the surface (see section 4.5.2), until approximately $\Delta T \leq 0.45\,^{\circ}\mathrm{C}$, when the free patches start attracting each other noticeably.

To study the formation of phases, we let the sample assemble by slowly approaching T_c in steps of $0.01\,\mathrm{K}$ or larger (up to $0.05\,\mathrm{K}$), starting from $\Delta T = 0.65\,^{\circ}\mathrm{C}$. The sample is prepared with a particle density gradient by slightly tilting the sample, so it is easy to observe a range of different area coverages η at a constant ΔT, see section 5.5.1. We take confocal microscopy images at several points in the sample and track both the particles' centre of mass and fluorescent patches to determine the bond angles with their neighbours (for tracking details, see section 2.3.3). While 1 of the 4 patches is bonded to the glass, the other 3 patches can participate in bonding and are at approximately the same height (see Figure 5.1c). By focussing at different heights, we can accurately determine the horizontal position of the particle centre (from the glass-bound patch) and the bonds between particles (from the bonding patches).

Simulations

In parallel with experiments, we also perform Monte Carlo (MC) simulations, to aid the mapping of the phase space. The interaction between particles is set by a generalized Lennard-Jones (LJ) repulsive core and an attractive tail modulated by an angle dependent function, which is a reasonable model for our patchy particle system [194, 195]. Further simulation details are given in SI. Simulations are performed at a range of different reduced temperatures (T^*) and surface coverages. In section 5.5.3, we compare the inter-particle potentials at several ΔT and T^* to be able to directly compare experiments and simulations at similar attractive strength.

5.3 Results and Discussion

At low patch-patch interaction strength (high ΔT) and low density (approx. $\eta < 0.5$), particle patches interact only weakly, resulting in a two-dimensional colloidal fluid, see Figure 5.1d. We measure the diffusion constant of the particles, see section 4.5.2, showing that colloids can freely diffuse laterally over the surface. At higher patch-patch interaction strength, starting from $\Delta T \approx 0.38\,\mathrm{K}$, particles

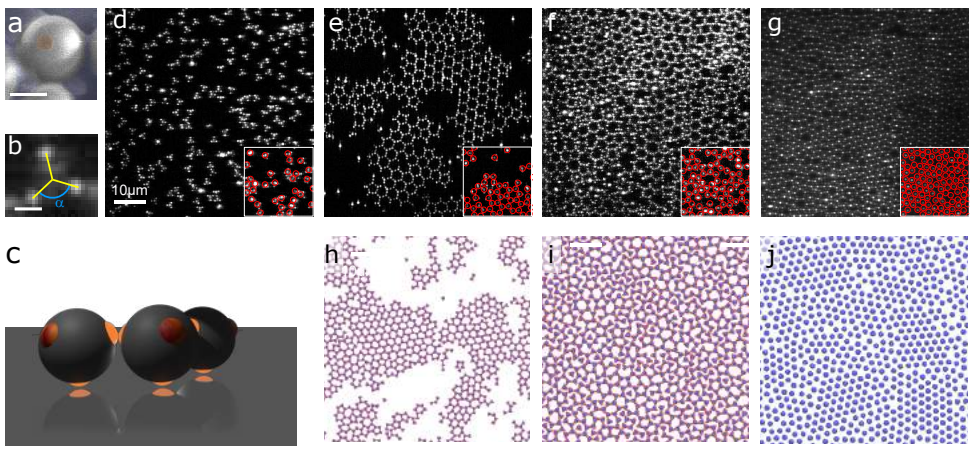

Figure 5.1 : Pseudo-trivalent tetrahedral particles display complex assembly. Tetrahedral particles with diameter $\sigma = 2$ μm are shown under (a) electron microscopy with false colour and (b) under confocal microscopy, where patches are fluorescent. The angle between particle bonds is indicated by α, corresponding to 120°. The scalebar in panel (a) and (b) is 1 μm. (c) shows that a particle becomes effectively trimeric when we attach one patch to the surface. The remaining three patches are available for bonding to other particles. Depending on interaction strength and particle density, simulation and confocal snapshots show (d) a fluid phase, (e)&(h) honeycomb-fluid coexistence, (f)&(i) an amorphous network, and (g)&(j) a triangular lattice in coexistence with an amorphous network. Confocal snapshots (e-g) are scaled equally, and have a small region where particles are annotated in red. In simulations snapshot (j), the patches are hidden to highlight the triangular packing of particles.

form a honeycomb lattice in equilibrium with a dilute fluid phase, see Figure 5.1e. In the lattice, each particle binds three other particles at 120° angle with respect to each other resulting in the typical repeating 6-membered rings motif of the honeycomb lattice. The honeycomb lattice is common in nature and engineering at all length scales due to its extraordinary mechanical and electronic properties. Famous examples include graphene, which is formed by the two-dimensional assembly of trivalent atoms [149, 196].

At higher densities, more exotic equilibrium structures emerge. Around an area fraction of $\eta = 0.55$, an amorphous network is observed, Figure 5.1f. This network is characterized by a wide distribution of ring sizes, in which particles exhibit non-ideal bond angles, slightly above or below 120°. The open nature of the honeycomb lattice is preserved, but the order is lost: the rings do not periodically tile the surface like in the honeycomb lattice, but fill the area seemingly without long-range order. At yet higher density, at an area fraction of approximately $\eta > 0.6$, the particles pack tightly in the triangular phase, Figure 5.1g. The triangular lattice consists of a honeycomb structure in which each honeycomb cell is occupied by an additional particle. Particles are ordered in a dense hexagonal close packing (hcp), but still bind to neighbours within the lattice due to their attractive patches.

Simulation snapshots of the system at similar density and attractive strength as the experimental snapshots are shown in Figure 5.1h-j. The simulations seem to capture our experimental results very well: simulated and experimental snapshots display remarkably similar structures; the three condensed phases are formed both in experiment and simulation.

5.3.1 The Phase Diagram

To gain a more complete understanding of our system, we construct a density-temperature phase diagram based on our experiments in Figure 5.2a, and simulations in Figure 5.2b. The fluid phase is indicated in grey, the honeycomb-fluid coexistence in yellow, the amorphous network phase in blue and the amorphous-triangular coexistence phase in red. Each point in the diagram represents an observation.

In experiments, the fluid phase (microscopy snapshot overlaid with particle orientations shown in Figure 5.2c), is present at high ΔT (low interaction strength) and low density, and consists of freely diffusing, mostly unbound particles. The

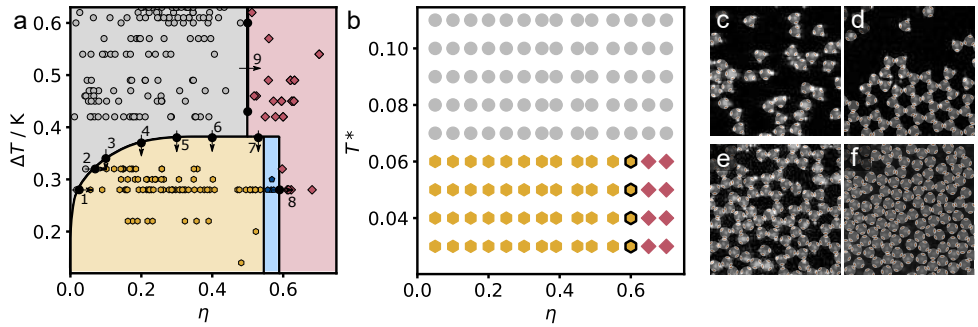

Figure 5.2 : The phase diagram. Combining all our data, we construct a phase diagram of our experimental system in (a) and simulated system in (b). The fluid phase is indicated in grey, the honeycomb-fluid coexistence phase is indicated in yellow, the amorphous network phase is indicated in blue and the amorphous-triangular coexistence phase is indicated in red. In (a), black points and their number indicate points $\mathbf{x}_i$ on the coexistence line, which are determined from isotherms (horizontal arrow) or isobars (vertical arrow) in Figure 5.4. The pure honeycomb phase in (b) is indicated with yellow hexagons with black borders. Each point is an observation, coloured based on the phase we observe in a snapshot at these conditions. To illustrate the phases, patchy particles are drawn on top of the insets of Figure 5.1d-g: (c) the fluid phase, (d) honeycomb-fluid coexistence, (e) amorphous network and (f) amorphous-triangular coexistence.

fluid-to-honeycomb transition occurs upon increasing interaction strength (decreasing ΔT) as indicated by arrows 3 to 6, or when increasing density, along arrows 1&2. A microscopy snapshot of the fluid-honeycomb coexistence is shown in Figure 5.2d.

In experiments, a phase transition from fluid-honeycomb coexistence to the amorphous phase takes place at surface coverage $\eta = 0.53$. The amorphous phase, Figure 5.2e, leaves part of the open honeycomb structure intact, but packs particles at a higher density by introducing different ring sizes. This results in a structure which is slightly density than the honeycomb lattice, and contains only few unsaturated patches. Due to its open structure, the honeycomb lattice has a maximum packing fraction $\eta \approx 0.60$, beyond which the lattice simply cannot accommodate more particles. The amorphous network on the other hand can accommodate higher particle densities, but pays an energy penalty for bending bonds out of their equilibrium angles to from non-ideal ring sizes.

As density increases further, another phase transition is observed in experiments: along arrow 8 in Figure 5.2a, a transition from the amorphous network

to a coexistence of amorphous and triangular phases takes place. The triangular lattice is shown in Figure 5.2f, and consists of particles assembled in a hexagonal close-packed (hcp) structure, such that as many patch-patch bonds as possible are formed. The triangular phase is essentially just the honeycomb lattice with additional particles placed in the centre of each hexagon. This leads to at least 20% of patches being unsaturated in equilibrium, which makes this phase energetically unfavourable at lower densities.

The simulations phase diagram, Figure 5.2b, is mostly in agreement with the experimental phase diagram: the fluid, fluid-honeycomb and amorphous-triangular phases are all present at approximately the same attractive strength and density (see section 5.5.3). Unfortunately, the density-induced fluid to fluid-honeycomb coexistence transition cannot be verified in simulations, due to difficulties in equilibrating the MC simulations at these very low densities.

In simulations, we observe a pure honeycomb lattice, a feature not found in experiments. This is not surprising: due to the short range of the critical Casimir force (in the order of 0.01σ, section 5.5.3), the pure honeycomb region is expected to be extremely narrow and easily missed, and kinetic effects may quickly lead to the amorphous phase.

Furthermore, a pure amorphous phase is not observed in simulations. Instead, there is an immediate transition from honeycomb to amorphous-triangular coexistence. The amorphous and triangular phases can accommodate a high particle density at the expense of bending and dangling bonding energy penalties, respectively. This means that the bond flexibility of the patchy particle determines what structure is energetically more favourable: if the particle's bond bending energy penalty is relatively minor compared to the dangling bond energy penalty, we expect the amorphous phase to take up an extended region in phase space. If, on the other hand, bond bending carries a large energy penalty due to e.g. narrow patches, we expect to see a gradual transition from honeycomb to triangular, without an intermediate amorphous phase [26]. In our experimental system, the bond bending energy cost is estimated to be on the order of $40 k_\mathrm{B} T \mathrm{rad}^{-2}$ (assuming spring-like bending, see section 4.5.6), leading to a small energy penalty to the formation of penta- and heptagons. A difference in this value between experiments and simulations may thus explain why experiments show a narrow amorphous region, while simulations do not show an amorphous region at all.

In experiments, the triangular phase is encountered at low interaction strength (high ΔT), contrary to the other condensed phases, and contrary to what sim-

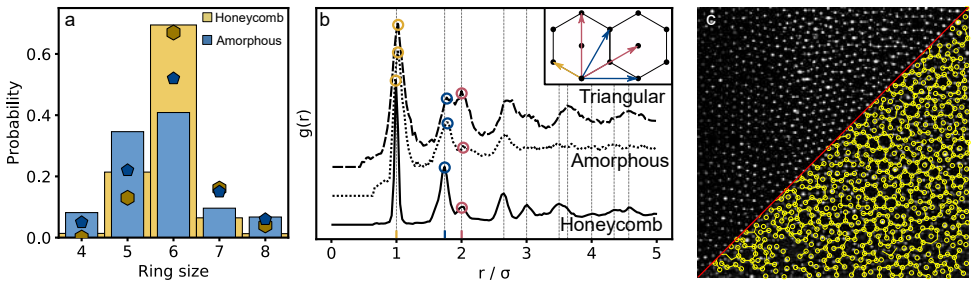

Figure 5.3 : Structural analysis. (a) Ring size distribution in the honeycomb phase (yellow) and amorphous phase (blue). The histogram shows experimental results, the dots the results from simulations. (b) The radial distribution function, $g(r)$ of the three different condensed phases, honeycomb (solid), amorphous (dotted), and triangular (dashed). The $g(r)$ has been normalized to the height of its nearest-neighbour peak as well as shifted along the y-axis. The vertical dotted lines indicate theoretical peak locations, full analysis can be found in section 5.5.5. The inset shows a schematic drawing of the 3 smallest typical distances in our system, 1σ (yellow), 1.74σ (blue) and 2σ (red). The matching peaks in the plot have been highlighted. (c) Confocal image of triangular lattice and bonding. In the top-left half of the image we show the glass-bound patches, effectively particle centres. In the bottom-right we show the bonding patches overlaid with all particle bonds in yellow, showing the internal network of the triangular phase.

ulations show. As the patches are only weakly attractive at such high ΔT, our particles act somewhat like isotropic colloids. We hypothesize that the crystallization along arrow 9 in Figure 5.2a is akin to simple hard-sphere crystallization under high pressures. The transition at $\eta_9 \approx 0.5$ is lower than expected based on purely hard-sphere interactions, and is not observed in simulations, but reasonable if we assume there is likely some bulk-bulk attraction [197].

5.3.2 Structural Analysis

To further elucidate the nature of the amorphous and triangular phases and their relation to the honeycomb lattice, we analyse their structures. Important structural motifs are the rings, the sizes of which are characteristic of the phases: they are strictly 6-membered in the honeycomb lattice, and more broadly distributed in the amorphous phase. The ring size distribution of both phases are shown in Figure 5.3a, bars indicate experimental measurements, dots indicate simulation results. As expected, both the experimentally obtained and simulated honeycomb

phase consists primarily of 6-membered rings, but also shows a small fraction of 5- and 7-membered rings. While the perfect honeycomb lattice would purely consist of only hexagons, the experimental and simulated lattices display defects, mostly at grain boundaries (see Chapter 4), leading to deviations from perfect hexagons. Nevertheless, the amorphous network phase displays a much broader distribution of ring sizes, indicating that this phase consists of a variety of motifs in its bulk, including large fractions of 5- and 7- membered rings. This broad ring size distribution is a hallmark of two-dimensional trivalent particle networks: similar distributions have been found in amorphous silica and the theoretical triangle network, even though the bond details (bending and stretching strain) are very different from our case [198]. The ring-size distributions from experiments, compared to the ones from simulations reveal an interesting kinetic effect: the number of 5-membered rings in experiments is significantly larger, while the number of 7-membered rings is smaller than in simulations. The origin of this difference may lie in kinetic effects, favouring smaller ring sizes in experiments, and in the different effective patch sizes of experiments versus simulations.

We can further compare the experimental amorphous and honeycomb phases via the pair correlation function $g(r)$, plotted in Figure 5.3b. Surprisingly, even after the expected nearest-neighbour peak at 1σ (1 particle diameter), the $g(r)$ of the two phases is remarkably similar: all visible peaks seem to coincide, indicating similar short-range structure. For the amorphous phase, however, peaks diminish after a few particle radii, while for the honeycomb phase, peaks are still well-defined even at long distances. The short-range similarity of the amorphous and honeycomb radial distribution functions is a direct result of their very similar basic structural motifs. Both phases consist of rings related to the particles' vacancy: hexagons in the honeycomb case, a mix of mainly penta-, hexa-, and heptagons in the amorphous case. These rings share similar typical internal distances, leading to a very similar short-range radial distribution function (see section 5.5.5). The amorphous $g(r)$ decorrelates at larger distances because each shell of rings introduces a diverging number of ring size combinations and associated characteristic distances. Although some ring combinations are preferred, see section 5.5.6, the decorrelation is inevitable, and consistent with the lack of long-range order of the network. These effects are in line with other observations of amorphous networks consisting of trivalent subunits, and have been observed at length scales spanning from atomic to macroscopic [198].

In contrast to the honeycomb and amorphous phases, the triangular phase is characterized by hexagonal close packing, giving rise to a dense network of patch-patch bonds within this packing. These two layers of organization are exemplified in the microscopic image in Figure 5.3c. The glass-bound patches (equivalent to particle centres) in the top-left clearly show the hcp lattice of the phase. The bottom-right of Figure 5.3c highlights the network of bonds between particles overlaid onto the image. Combined, both halves of Figure 5.3c reveal the complex internal structure of the triangular phase at low ΔT that is not revealed by simple particle locations.

The close vicinity of the triangular to the honeycomb lattice, with each honeycomb cell occupied by another particle, is reflected in the $g(r)$ (Figure 5.3b): the peak positions of the triangular lattice largely coincide with those of the honeycomb lattice, but the peak intensities are different: for instance, the peak at 1.74σ, corresponding to a particle in the ring, and the peak at 2.00σ, corresponding to both particle in a ring and the central particle of a ring, have different relative heights. In the honeycomb lattice, the peak at 2.00σ is smaller than the one at 1.74σ, reflecting the absence of centre particles in the open honeycomb lattice compared to the triangular lattice: in the latter, both distances are equally likely, while in the honeycomb case, the 2.00σ distance only occurs half as often, see inset of Figure 5.3b. The intensity ratio R of the two peaks thus characterizes open and closed phases: a ratio below 1 indicates an open structure (the honeycomb and amorphous phases), while a ratio above 1 corresponds to the closed triangular phase, and a ratio close or equal to 1 indicates that neither peak is present, signalling a disordered fluid phase.

5.3.3 Order Parameters

Based on the structural properties discussed, we can now define order parameters to construct the coexistence lines between the phases in the experimental phase diagram. To do so, we follow the main structural changes along isobars and isotherms, and use structural order parameters to pinpoint the phase transition lines.

The fluid phase is characterized by a low number of bonded neighbours, therefore, the fluid-honeycomb phase transition along arrows 1 to 5 in Figure 5.2a is easily determined using the mean number of neighbours $\langle N_{\mathrm{nb}} \rangle$ of a particle. We define nearest neighbours as those particles with centres found within 1.1σ of

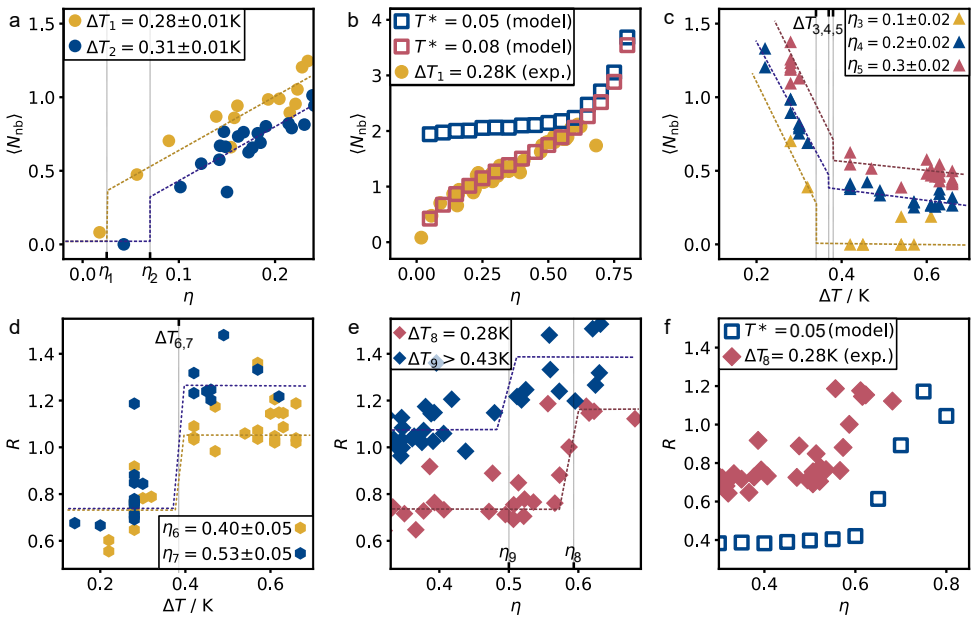

Figure 5.4 : Visualizing the phase transitions along isotherms and isobars. By following an order parameter along isotherms and isobars, we can identify points $\mathbf{x}_i$ along the coexistence lines of the experimental phase diagram (Figure 5.2a). We determine the average number of neighbours $\langle N_{\mathrm{nb}} \rangle$ as a function of surface coverage η (a) and ΔT (c) in experimental snapshots to pinpoint the fluid to fluid-honeycomb transition. The trends found in (a) are in excellent agreement with results from our simulations shown in (b). To determine the other transitions in experiments, we follow typical lattice distances via ratio R (see eq. 5.6) as a function of η (d) and ΔT (e). Panel (f) shows the qualitative agreement between trends in R as a function of η observed in experiment and simulations. In all Figure panels, the dotted line is a guide for the eye.

the particle under consideration. In Figure 5.4a, we show $\langle N_{\mathrm{nb}} \rangle$ as a function of surface coverage η at two different interaction strengths. In both cases, $\langle N_{\mathrm{nb}} \rangle$ jumps from 0 to a non-zero value, signalling the transition from a low-density fluid phase to fluid-honeycomb coexistence. After this point is reached, $\langle N_{\mathrm{nb}} \rangle$ increases monotonically along the ΔT_1 and ΔT_2 isotherms, indicating the growth of the honeycomb lattice at the expense of the fluid phase. In Figure 5.4b, we follow the same order parameter for the simulations at two constant attractive strengths. The behaviour is strikingly similar to that in the experiment: the evolution of $\langle N_{\mathrm{nb}} \rangle$ at $T^* = 0.08$ and $\Delta T = 0.28\,\mathrm{K}$ almost perfectly overlap, as expected from their similar attractive strength (section 5.5.3). Although the discontinuity is not observed in simulations due to problems with equilibrating the system at low densities, the similarity between simulation and experiment suggest a fluid-fluid transition as well. In contrast, at higher interactive strength, $T^* = 0.05$ - equivalent to approx. $20 k_{\mathrm{B}} T$, $\langle N_{\mathrm{nb}} \rangle$ plateaus at low density; the fluid-honeycomb coexistence phase extends all the way to low density.

We also explore the isobaric path at constant density and increasing attraction, by plotting the experimentally observed $\langle N_{\mathrm{nb}} \rangle$ as a function of ΔT at three different volume fractions in Figure 5.4c. In the fluid phase, at low attraction (high ΔT), $\langle N_{\mathrm{nb}} \rangle$ is low. When the attraction increases, $\langle N_{\mathrm{nb}} \rangle$ jumps and increases strongly, signalling the transition from the fluid phase to honeycomb-fluid coexistence. Still, only at the lowest density $\eta_3 = 0.1$, the fluid phase shows vanishing $\langle N_{\mathrm{nb}} \rangle$. At higher volume fractions $\eta_4 = 0.2$ and $\eta_5 = 0.3$, $\langle N_{\mathrm{nb}} \rangle$ no longer vanishes; the reason is twofold: firstly, particles in the fluid can bond transiently; bonds form, but break up before particles get close to forming the honeycomb lattice. Secondly, at higher densities, particles are statistically more likely to be within the nearest-neighbour range without being bonded. These tendencies lead to slight continuous increase of $\langle N_{\mathrm{nb}} \rangle$ before reaching the true phase transition. $\langle N_{\mathrm{nb}} \rangle$ is therefore not the ideal order parameter to identify the phases at higher densities. Instead, we can make use of the characteristic distances of the condensed phases of 1.74σ and 2.00σ. Specifically, the characteristic height ratio R of the $g(r)$ peaks at 1.74σ and 2.00σ can be used as an order parameter indicative of the phase transitions.

Because of these properties, R is a suitable order parameter for characterizing the transition from fluid to amorphous or honeycomb phases, specifically at high density, e.g. paths 6 & 7 in Figure 5.2a, whose R values are shown as a function of ΔT in Figure 5.4d. The transition from fluid to honeycomb lattice is signalled

by a jump of R from below 1 in the open lattice to approximately 1 in the fluid phase, placing the phase transition at $\Delta T_6 \approx 0.35$. The isobar along $\eta_7 = 0.53$ acts differently: instead of R jumping to 1, R becomes larger than 1, indicating a transition from an open structure to the triangular phase, as shown in the phase diagram in Figure 5.2a.

R is also a suitable order parameter to detect the transition from the triangular to the amorphous phase, arrow 8 & 9 in Figure 5.2a. We follow R as a function of η at $\Delta T_8 = 0.28\,\mathrm{K}$ in Figure 5.4e. The clear jump at $\eta_8 = 0.58$ indicates the phase transition from the open amorphous lattice to the triangular lattice. The simulations show a similar transition from an open to a closed structure in Figure 5.4f. The transition occurs at a slightly higher density compared to the experiments, which is expected given the somewhat shifted phase diagram of the simulations. The difference in magnitude of R between simulation and experiment is probably due to the inherent noise present in the experimental data, leading to R values closer to $R = 1$.

Finally, we also use the peak ratio R to follow the density-induced transition from unordered fluid to triangular phase in the absence of strong patch-patch attraction (arrow 9 in Figure 5.2a). By plotting R as a function of η for $\Delta T_9 > 0.43\,\mathrm{K}$ in Figure 5.4e. Although R is by no means the ideal parameter to signal this transition [197], a jump does clearly occur at around $\eta_9 = 0.5$, indicating a transition to an ordered phase.

5.4 Conclusion

By utilizing the excellent control over patch-patch attraction offered by the critical Casimir force, we experimentally explore the pressure-interaction phase diagram of pseudo-trivalent colloidal particles adsorbed at a substrate. This relatively simple system displays a surprisingly rich phase behaviour, not only assembling into the honeycomb lattice, but also into an amorphous network and a triangular phase at increasing particle density. Combining our experiments with simulations, we find that the three condensed phases are structurally closely related, and a delicate balance between bending and bonding energies determine their interconversion. By following order parameters along isobars and isotherms, we construct the phase diagram of the system.

The exploration of the complex phase diagram illustrates the increasingly advanced control over patchy particle assembly, and opens the door to experimental investigation of the full phase space of the assembly of patchy particles with different valencies. The surprisingly rich assembly behaviour found in this simple patchy particle system hints at a wealth of interesting behaviours in more complex systems; there is a huge phase space to explore, while varying parameters such as density, attractive strength, particle geometry, and system dimensionality.

5.5 Appendix

5.5.1 Sample Preparation and Measurements

Tetrapatch particles (diameter of $2.0\ \mu\mathrm{m}$, patch diameter of approx. $0.5\ \mu\mathrm{m}$, batch C in Table 2.1, see sections 4.5.3 & 4.5.6) are dispersed in the regular binary solvent of 25% 2,6-lutidine ($\geq 99.0\%$, Sigma Aldrich) and 75% milliQ water with $1\ \mathrm{mM}$ $MgSO_4$ ($\geq 99.5\%$, Sigma-Aldrich), as described in section 2.2.3. The particles are washed several times in the water-lutidine mixture. The resulting particle dispersion is injected into a silanized hydrophobic glass capillary and sealed with teflon grease (for full preparation see section 2.3.1).

Confocal Microscopy and Particle Tracking

Particles are left to sediment to the bottom of the sample at room temperature before measurements. We tilt the sample slightly during sedimentation, so a small density gradient is present in the sample. We then heat the sample to 33.45°C ($\Delta T \approx 0.65$°C), which causes one of the particle patches to attach to the sample wall. For heating, we use a well-controlled temperature stage in combination with an objective heating element, as described in section 2.3.2.

In an experiment, we typically heat a sample to a certain ΔT below the phase separation temperature of the lutidine-water mixture, inducing critical Casimir attraction between patches. The structures then grow by two-dimensional diffusion in the plane. No mixing is necessary. After several hours of equilibration, we investigate the structures using a 100x oil-immersion objective.

We image the assembled structures using confocal microscope image stacks, sometimes alternating with bright field images. We track the particle locations via the network-based approach described in section 2.3.3. The highest density samples (i.e, the triangular phase) could not be tracked using this technique: there were too many outer patches to consistently identify bonds. However, particle centres could still be accurately determined. The bonds shown in Figure 5.3c are determined by naked eye.

5.5.2 Simulation Details

The Potential

The interaction between particles is described by a generalized Lennard-Jones (LJ) repulsive core and an attractive tail modulated by an angular dependent function [194, 195]:

$$V_{ij}(\mathbf{r}_{ij}, \mathbf{\Omega}_i, \mathbf{\Omega}_j) = \begin{cases} V'_{\mathrm{LJ}}(r_{ij}) & : r_{ij} < \sigma'_{\mathrm{LJ}} \\ V'_{\mathrm{LJ}}(r_{ij}) V_{\mathrm{ang}}(\hat{\mathbf{r}}_{ij}, \mathbf{\Omega}_i, \mathbf{\Omega}_j) & : r_{ij} \geq \sigma'_{\mathrm{LJ}} \end{cases}, \tag{5.1}$$

where $\mathbf{r}_{ij}$ is the inter-particle vector, α and β are patches on particles i and j, respectively, $\mathbf{\Omega}_i$ is the orientation of particle i, $V'_{\mathrm{LJ}}(r)$ is a cut-and-shifted $m-n$ LJ potential and σ'_{LJ} corresponds to the distance at which V'_{LJ} passes through zero:

$$V'_{\mathrm{LJ}}(r_{ij}) = \frac{n}{n-m}\left(\frac{n}{m}\right)^{\frac{m}{n-m}} \epsilon_{LJ}\left(\left(\frac{\sigma_{LJ}}{r_{ij}}\right)^n - \left(\frac{\sigma_{LJ}}{r_{ij}}\right)^m\right) \tag{5.2}$$

The exponents of the generalized-LJ model are assigned large values, in particular 200-100, to obtain a short ranged model mimicking that found in experiments of colloidal particles. The cut-off distance is set to $r_{\mathrm{cut}} = 1.10\,\sigma_{\mathrm{LJ}}$, at which the energy is rather small (-0.0029ϵ).

The angular modulation term V_{ang} is a measure of how directly the patches α and β point at each other, and is given by

$$V_{\mathrm{ang}}(\hat{\mathbf{r}}_{ij}, \mathbf{\Omega}_i, \mathbf{\Omega}_j) = \exp\left(-\frac{\theta^2_{\alpha ij}}{2\sigma^2_{\mathrm{ang}}}\right)\exp\left(-\frac{\theta^2_{\beta ji}}{2\sigma^2_{\mathrm{ang}}}\right), \tag{5.3}$$

$\theta_{\alpha ij}$ is the angle between the patch vector $\hat{\mathbf{P}}^{\alpha}_i$, representing the patch α, and $\hat{\mathbf{r}}_{ij}$. Each particle has four patches distributed tetrahedrally on the particle surface. σ_{ang} is a measure of the angular width of the patch. In this study, the angular width is set to σ_{ang}=0.52 radians.

The patches interact also with the bottom surface through the same interaction potential (Eq. 5.2). The difference is that now the distance between the particle and the surface is given by the z-coordinate of the particle position vector, and the angular term depends only on the Gaussian of the angle of the interacting patch

with the normal to the surface. The interaction strength between two particles is set to unity, $\epsilon_{LJ} = 1$, and that between a particle and the bottom surface is set to $\epsilon_s = 4\epsilon_{LJ}$. We use σ_{LJ} as the unit of length, and the LJ well depth $\varepsilon_{\mathrm{LJ}}$ as the unit of energy. Temperatures are given in reduced form:

$$T^* = k_B T/\varepsilon_{\mathrm{LJ}}. \tag{5.4}$$

Besides these interactions, to mimic the experimental conditions, particles were also subject to a gravitational potential:

$$u_{\mathrm{grav}}(z) = \frac{z}{l_{\mathrm{grav}}} k_{\mathrm{B}} T \tag{5.5}$$

where l_{grav} is the gravitational length, whose value was estimated from the relation $l_{\mathrm{grav}} = k_{\mathrm{B}}T/\Delta\rho V_{\mathrm{c}} g$, where $\Delta\rho$ is the density difference between the colloids and the solvent, V_{c} is the volume of the colloidal particles and g is the gravitational constant. Here, we took $l_{\mathrm{grav}} = 0.5865\sigma_{\mathrm{LJ}}$. Note, however, that the effect of this term once the particles are deposited on the surface is small, because the strength of the wall with the particles' patches is stronger.

Simulations

We use Metropolis Monte Carlo to simulate the patchy-particle systems in the canonical ensemble (NVT). The simulations are performed in an orthorhombic box with $N = 900$ colloidal particles. Periodic boundary conditions are applied along the x and y axes. Several lengths of the simulation box along the x and y, L_x and L_y, are used to cover surface packing fractions, $\eta = N\pi/L_x/L_y/4$, between 0.001 and 0.85. In order to minimize the incommensurability of the assembled honey-comb and triangular lattices with the simulation box, we set $L_x = 2/\sqrt{3}L_y$. L_z is initially set to $L_z = 100\sigma_{\mathrm{LJ}}$. Particles are initially distributed randomly in the simulation box. The system is then allowed to evolve until all the particles sediment and bind to the bottom surface. Using this state as the initial configuration, simulations are then performed at different temperatures. To improve the sampling, besides normal MC moves, aggregation volume moves (AVB) [199] are also performed. The acceptance probability of the MC moves is set to 50-70%. Typically, the MC simulations consist of 100 million MC cycles, where one cycle is defined as N attempts to translate or to rotate a particle. At the

lower temperatures, simulations need to be twice or three times longer to get well converged results.

5.5.3 Comparing Simulations and Experiments

The reduced temperature T^* sets the interaction strength between particles in simulations, while the distance to the critical temperature $\Delta T = T - T_c$ sets the interaction strength in experiments. Unfortunately, relating these two parameter is non-trivial, which limits direct comparison of simulation and experimental results. To nevertheless make a comparison, we plot the inter-patch potentials in simulations and experiment in Figure 5.5. Simulated potentials result from the Lennard-Jones potential of eq. 5.2, while the Casimir potential is generated by formulating the critical Casimir potential model presented in [82] for patchy particles and benchmarking it onto our patchy particles as shown in [133]. We select values of ΔT and T^* which result in approximately the same potentials, so that we can estimate at which temperatures similar behaviour is expected. Figure 5.4b of the main text shows that this approach is effective: the average number of neighbours $\langle N_{\mathrm{nb}} \rangle$ as a function of area coverage η in experiments and simulations almost perfectly overlap for $\Delta T = 0.28\,\mathrm{K}$ and $T^* = 0.08$, in agreement with their matching potentials in Figure 5.5.

5.5.4 Order Parameter R

When our system transitions from an open structure (like a honeycomb lattice or amorphous network) to a closed lattice (the triangular lattice), the systems' radial distribution undergoes a small but significant change, as illustrated in Figure 5.3b. The most obvious change occurs at the 2σ peak, which is significantly bigger in the triangular phase due to the particle occupying each hexagonal ring. Therefore, we can use the ratio between this peak and the unchanged peak at 1.74σ to follow the transition from open to closed structure; we define the ratio between the two peaks:

$$R = \frac{\int_{1.6\sigma}^{1.9\sigma} g(r)\,\mathrm{d}r}{\int_{1.9\sigma}^{2.1\sigma} g(r)\,\mathrm{d}r}. \tag{5.6}$$

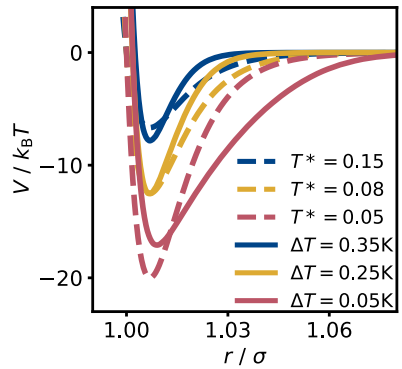

Figure 5.5 : **Inter-particle potential in simulations and experiments.** The inter-particle potential V in units $k_\mathrm{B}T$ as a function of distance between particles centres r in units diameter. We compare the potential in simulations at three reduced temperatures (dashed lines) with estimated critical Casimir potentials in experiment (solid lines). Although the potentials do not match perfectly, we can estimate that comparable behaviour is expected at potentials with the same colour.

This ratio R has a value below 1 in the case of an open structure (the honeycomb and amorphous phases), while a value above 1 corresponds to the closed triangular phase, and a value close or equal to 1 when neither peak is present, signalling an unordered fluid phase. We use this ratio as order parameter to determine coexistence points between two phases in Figure 5.4.

5.5.5 Radial Distribution Peaks

Figure 5.3b shows the radial distribution function of the honeycomb, triangular and amorphous phases. As we discuss, the typical distances revealed by the radial distribution function of these three condensed phases overlap due to their shared structural motifs. In Figure 5.6a, we show the radial distribution function of the honeycomb lattice without normalization, with each characteristic distance indicated. In Figure 5.6b, the corresponding distance is indicated in the honeycomb or triangular lattice. Figure 5.6c highlights the small difference in internal distances of a 5-, 6-, and 7-membered ring: the two possible distances within a ring, indicated with red and blue are very similar in all three ring types.

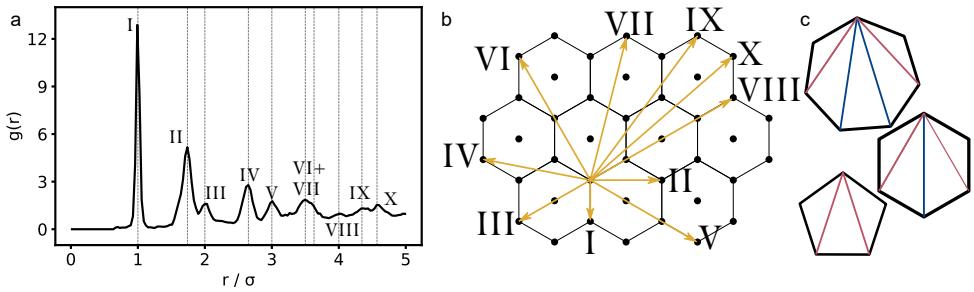

Figure 5.6 : Typical distances in an open lattice. The characteristic distances of the honeycomb lattice are labelled with Roman numerals in its radial distribution function (a). These distances are schematically denoted in a sketch of the honeycomb lattice (b). In (c), the small difference in typical internal distances of 5-, 6-, and 7-membered rings is indicated, highlighting why the amorphous networks still show the same typical distances as a regular honeycomb lattice.

5.5.6 Particle Neighbourhood

In this chapter we have briefly discussed that the amorphous phase shows some local order, but little long range order, highlighted by the radial distribution function shown in Figure 5.3a, where peaks die away only at longer ranges. Here, we further examine the short-to-medium range order of the amorphous phase by studying the local ring neighbourhood. We find all particle rings in a sample, and determine the probability to find an n-membered ring as neighbour to an m-membered ring, see Figure 5.7a-c. In the honeycomb phase (shown in yellow), 5-, 6-, and 7-membered rings are all most likely to have a neighbouring 6-membered ring. However, it is clear that 5-membered rings are much more likely to be next to a 7-membered ring instead of another 5-membered ring and visa versa. This is in line with the fact that neighbouring 5- and 7-membered rings experience significantly less bonding strain, see Figure 4.2b: a 'scar' of 5- and 7-membered rings is a typical defect seen in assemblies of trivalent, surface-confined building blocks because it is geometrically relatively stable, see Chapter 4 [200].

In the amorphous case (shown in blue), the distribution is much more ambivalent: All ring sizes have nearly equal probability of being next to any other ring. This is hardly surprising considering the random packing of these many-sized rings.

A related metric is the probability of ring triplets combinations, given in Figure 5.7d: the probability of finding 3 rings clustered together, see the inset draw-

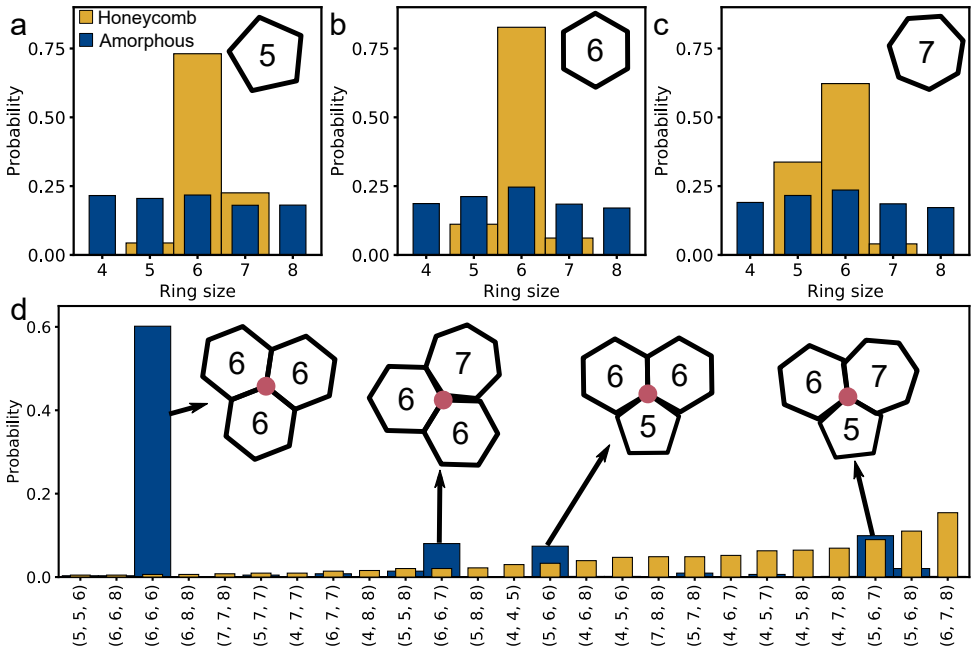

Figure 5.7 : Particle neighbourhoods. The ring neighbourhood evaluation: the probability of finding an n-membered ring neighbouring a 5-membered ring (a), 6-membered ring (b), and 7-membered ring (c). The data is given for both the experimental honeycomb lattice (blue) and amorphous network (blue). (d) Probability of encountering ring triplet combinations in the honeycomb (blue) and amorphous (yellow) phase.

ings. In the honeycomb case (blue), the (6,6,6) triplet is by far the most common, as we would expect in this lattice built of hexagons. Other significant fractions include (5,6,7), a typical defect element (see Chapter 4), (5,6,6), and (6,6,7). In the amorphous case (yellow), the triplet probability is much more broadly distributed. However, there are still clear preferences, clearly signalling that the amorphous phase is still somewhat ordered over 'medium' distances. This matches similar observations in other trivalent amorphous networks, like amorphous silica [200].

6 Networks of patchy colloids

> There will be seen in [this book] demonstrations of those kinds which do not produce as great a certitude as those of geometry, and which even differ much therefrom, since whereas the geometers prove their Propositions by fixed and incontestable Principles, here the Principles are verified by the conclusions to be drawn from them; the nature of these things not allowing of this being done otherwise.
>
> *Christiaan Huygens*
> Treatise on Light [201]

In this chapter, we study networks formed by aggregating patchy particles. Using critical Casimir forces, we assemble divalent and pseudo-trivalent patchy particles by slowly increasing the attractive strength. We compare this near-equilibrium route to a fast quench to high interaction strength and observe that both assembly routes pass through the same equilibrium states, suggesting that the limited valency of particles leads to the formation of an equilibrium gel. The topology of the network is purely set by the equilibrium configuration, independent of its history. Our limited-valency system follows percolation theory remarkably well, and approaches the percolation point with the expected universal exponents. Finally, we show that Flory-Stockmayer theory describes the assembly process well, with a small correction applied for the additional rotational degree of freedom of single monomers.

6.1 Introduction

Gels are ubiquitous in our daily lives as food and cosmetic products, and of importance in fields ranging from art conservation [202] to Alzheimer research [203] and biomaterials [204]. Gels are therefore well studied, but not every aspect of the gelling process is equally well understood. A gel is a dilute microscopic network consisting of interconnecting chains, typically made up of either polymers or colloidal particles. Although the end results of both types of gelation are rather similar, a low-density load-bearing material, their formation process is fundamentally different. A polymer gel is formed by monomers that have a well-defined valency (for instance a mix of monomers with two and three binding sites), undergoing covalent reactions to form a network. Colloidal gels, on the other hand, are typically formed by simple isotropic particles that undergo an arrested phase separation: particles are made strongly attractive (quenched) after which they cluster together and assemble into an out-of-equilibrium network of clustered particles [48].

To describe the formation of a polymer gel, Flory and Stockmayer proposed a series of laws and relations based on graph theory to describe the growth of polymers with a discrete valency into larger and larger networks [205]. As it turns out, the principles underlying this chemical process apply to many other fields involving the growth of networks, ranging from the spread rate of forest fires to oil field exploration. The physical basis is given by percolation theory, the study of networks and their properties [206]. Unfortunately, due to the fundamentally different formation mechanism, Flory Stockmayer theory (FS) is not applicable to the gelation of colloidal particles as described above. The formation of a colloidal gel is by definition an out-of-equilibrium process, and the properties of the gel are set by the conditions under which gelation takes place [207–209]. There is therefore no general theory encompassing the aggregation and structure formation processes in this type of system.

However, simulations and theory have shown that colloidal gels can be formed under equilibrium conditions, given that particles have a limited bonding valency [40, 49]. Therefore, equilibrium thermodynamics and statistical mechanics can be applied to this system, in contrast to a conventional, out-of-equilibrium colloidal gel, which bonding state is very much dependent on the system's history. This is an exciting and counterintuitive property, that is of great interest both fundamentally and from an applications' perspective. Equilibrium gels do not

undergo ageing, the slow phase separation process that colloidal gels undergo over time [210], because they are already at the thermodynamically preferred state; the gelling state is now only a function of the thermodynamic parameters of the system [49].

The limited valency required for an equilibrium gel can be achieved using anisotropic colloidal particles decorated with 'patches', attractive sites, on their surface. By tuning the size, number, and geometry of these patches, the valency and bonding geometry of these particles can be accurately controlled. This system is very similar to the polymer gels originally considered by Flory-Stockmayer (FS) theory: monomers with well-defined bonding valency cross-link into a network, and such a system can be well described by percolation theory. As such, the assembly of patchy particles into networks has been studied extensively in numerical models, and advanced theoretical predictions based on FS and Wertheim theory have been made [134, 211–215].

However, experimental confirmation has hardly been obtained, as it has been challenging, if not impossible, to induce particles to undergo sufficiently selective patch-to-patch bonding, especially forming bulk materials. In recent years, the situation has improved with the advancement of patchy-particle synthesis [190], so that experimental studies are becoming available [216, 217]. Especially work on DNA stars with well-defined valency has been very revealing [218–221]. However, these systems are mostly limited to studies of bulk properties, without direct observation of the percolating clusters, making direct comparison of experiment and theory elusive.

In this work, we assemble networks consisting of di- and trivalent colloidal particles, and directly observe the formation of a network using optical microscopy. We elucidate the network properties and formation dynamics of this system by applying classical FS theory. By tuning the patch-to-patch attraction using the critical Casimir force, we explore how the limited valency of the particles leads to the formation of an equilibrium gel. Specifically, we compare a fast quench of the system to a slow near-equilibrium route to percolation, to show that the state of the system is independent of the path. As predicted by FS theory, the bond probability uniquely defines the binding state of the system. As such, FS theory, with small corrections stemming from the quasi-2D nature of the system we consider here, is shown to capture our system remarkably well.

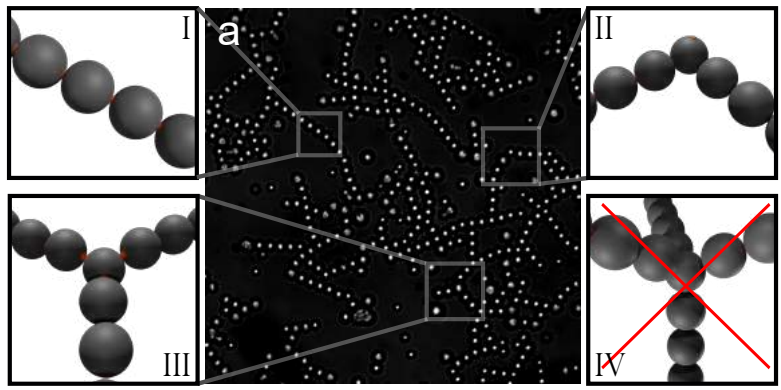

Figure 6.1 : An assembled network. After a deep quench to an attractive strength of $> 15k_{\mathrm{B}}T$ and sufficient equilibration time, a colloidal network is formed. In the network we observe three basic structural motifs: (I) stiff linear chains of dipatch particles, (II) kinked chains, formed by a tetrapatch particles with two (I) chains attached, and (III) a central tetrapatch hub with 3 (I) chains attached. Curiously, we never observe (IV), a central tetrapatch particle with four (I) chains attached.

6.2 Methods

The monomers used to assemble a network are 2- and 4-patch particles with diameters $3.2\,\mu\mathrm{m}$ and $3.7\,\mu\mathrm{m}$ respectively, batch A&B from table 2.1. Synthesized by colloidal fusion, the patch sizes are sufficiently small to allow only a single bond between particles per patch to be formed, as follows from Chapter 3. Particles are suspended in a binary mixture of water and 2,6-lutidine with lutidine volume fraction $c_L = 0.25$, with $1\,\mathrm{mM}$ $\mathrm{MgSO_4}$ to increase the bulk-patch contrast, see section 2.2.3. In this mixture, particles have a gravitational length of approximately 0.1 particle diameter, confining particles to the two-dimensional plane of the sample wall. The water-lutidine mixture induces attractive critical Casimir interactions between the particles when close to the critical temperature, T_{c}. The distance to this critical temperature, ΔT, sets the interaction strength between the patches, see section 2.2. In Chapter 3 we assembled analogues of alkane molecules using the same particles.

We investigate a particle mixture with a fixed 1:6 mixing ratio of 4- and 2-patch particles with a surface fraction of approximately $\eta = 0.1$. This concentration results in $S \approx 1700$ particles in our $\sim 240 \times 240\,\mu\mathrm{m}$ field of view, of which on average, there are $L \approx 240$ 4-patch and $N \approx 1460$ 2-patch particles. There

is also a small fraction of 'dud' particles ζ_{dud}: because of synthetic inaccuracies these particles lack patches and are thus not binding and not participating in the network. However, in regular bright-field imaging, dud particles cannot be distinguished from regular particles during experiments. The fraction of dud particles is estimated to be in the order of $\zeta_{\mathrm{dud}} = 0.05$.

We adjust the patch-patch attraction by varying the temperature offset from solvent critical temperature between $\Delta T = 0.40\,\mathrm{K}$ and $\Delta T = 0.05\,\mathrm{K}$, corresponding to an estimated interaction energy of approximately 2 to $> 15 k_{\mathrm{B}}T$ (see section 3.4.4) [133]. Using bright-field microscopy with careful temperature control, we follow the assembly of the network in real-time. Using a modern particle tracking package (TrackPy[120]), we locate the centres of all particles, see section 2.3.3. We consider two particles bonded when they are separated by $4.0\,\mu\mathrm{m}$ (approximately 1.1 particle diameters) or less, and if this bond persists for at least 50 consecutive seconds (5 frames).

In this work, we explore two different assembly paths: a deep quench to high interaction strength (from $\Delta T = 0.40\,\mathrm{K}$ to $\Delta T = 0.05\,\mathrm{K}$ in approx. $5\,\mathrm{min}$), and a near-equilibrium route, where we increase the interaction strength between particles slowly: starting at $\Delta T = 0.35\,\mathrm{K}$, we wait until we visually confirm the sample is in a steady state (in the order of 4-6 hours), and increase temperature by $0.05\,\mathrm{K}$, where we wait again, followed by another small increment, etc., until we reach $\Delta T = 0.05\,\mathrm{K}$. At low interaction strengths, the bond lifetime is much shorter than the experimental timescale, which leads to a balance of breaking and formation of bonds, see Figure 6.6b.

6.3 Results and Discussion

6.3.1 Hubs & Spokes

By quickly increasing the interaction strength from 2 to $> 15 k_{\mathrm{B}}T$ in a quench, patches become strongly attractive, and patch-patch bonds are formed. After about 4 hours of assembly, we obtain a network that spans the field of view, see online video [238]. Figure 6.1a shows a snapshot of the assembled structure; the particle network is easily recognized. We observe three types of structural motifs, schematically shown in Figure 6.1: (I) stiff linear chains consisting of dipatch particles, (II) kinked linear chains consisting of two strands of (I) connected by a

tetrapatch particle, and (III) branching points, a central tetrapatch particle connecting three strands of (I). Compared to (I) and (II), structure (III) has a small formation energy penalty because bonding patches point out of plane somewhat due to their tetrahedral arrangement; in Chapter 4 we have seen that tetrapatch particles can form 3 bonds in-plane, but at the cost of some energy penalty. Related to that realization is the fact that, despite the 4 available bonding sites on a tetrapatch particle, we never observe a tetrapatch particle with 4 connected strands in our experiments (Figure 6.1a-(IV)). Due to the small gravitational height of our particles, such a bonding arrangement will be energetically unfavourable due to the lifting of particles required to form structure (IV).

6.3.2 Cluster Structure

We hence consider the 4-patch particle as quasi 3-valent, which is essential for a quantitative understanding of our system using Flory-Stockmayer theory. Taking into account the observation that tetrapatch particles have a valency $f_N = 3$, the 2- to 4-patch ratio of 6:1 leads to an average valency of $\langle f \rangle = \frac{1\cdot3+6\cdot2}{6+1} = 2\frac{1}{7}$.

We track particle positions during the assembly process, and show a few representative snapshots in Figure 6.2a-d. Initially, clusters have a linear geometry and show little branching. As the assembly progresses, structures become increasingly cross-linked. The pseudo-trivalent tetrapatch particles act as hubs, leading to crosslinking between otherwise linear chains. This branching can be quantified by plotting the radius of gyration, r_g, as a function of the number of particles s in a cluster, as shown in Figure 6.2e-h. Initially, the radius grows linearly with the number of particles; resulting in a fractal dimension of $d_\mathrm{f} = 1$ (dotted line). When structures become larger than approximately $s = 10$ particles, the radius of gyration grows as the power of approximately 1.8^{-1}, indicating clusters are now branching, yielding a fractal dimension of $d_\mathrm{f} = 1.8$ (dashed line) [222]. This crossing over to a higher fractal dimension coincides with the behaviour found in simulations on particles with a similarly limited valency, and is close to the percolation universality class value of $d_\mathrm{f} = 91/48 \approx 1.89$, indicating that percolation theory can be used to describe our system [211].

A fractal dimension of $d_\mathrm{f} = 1.8$ is close to the full coverage of 2 dimensions, which is caused by the large density of loops and cross-links in large clusters, clearly visible in the snapshot of Figure 6.2d. The observation of the formation of loops in larger structures is significant; one of the key assumptions of the FS and Wertheim

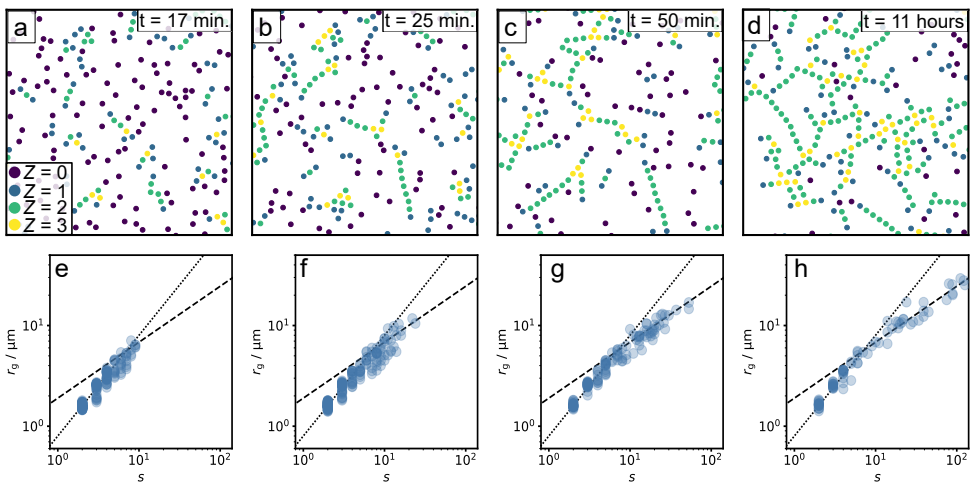

Figure 6.2 : Linear to branched clusters of quenched particle network. In (a-d), we show snapshots of the assembly process, with particles indicted as dots colour coded for the number of particles bonded to it (Z). In the early stages of the assembly process (a), clusters are small, but as the assembly progresses (b, c), structures grow larger, eventually leading to a phase-spanning network, (d), where central trivalent hubs connect linear chains. To visualize the transition from small linear chains to a branched network, we plot the radius of gyration r_g as a function of cluster size s, of the (a-d) snapshots in (e-h). We obtain the fractal dimension d_f of the system by fitting a power law to this relation, indicating to what degree the assembly is linear ($d_f = 1$) or two-dimensional ($d_f = 2$). In (e-h), dots are individual clusters in the system, dotted lines indicate a power law with exponent $d_f = 1$, dashed lines indicate a power law with exponent $d_f = 1.8$.

theories is that bonding loops are non-existent [205, 223]. Although the classical FS theory does not rely on spatial dimensions, it is known to work well enough for a three-dimensional system, where cross-links are rare [224], but is prone to fail in two-dimensional systems due to the large probability of forming loops [211].

6.3.3 Cluster Size Evolution - Quench vs Equilibrium

In contrast to the quench route, along which bonds hardly reconfigure, we observe frequent bond-breaking along the near-equilibrium route, especially at lower interaction strength (larger ΔT), indicating the system approaches the equilibrium state at each step.

To compare the near-equilibrium route with the fast quench, we follow the second moment of the cluster size distribution, $C = \sum s^2 N_s / \sum s N_s$, where N_s is the number of clusters of size s, which is commonly used in percolation theory as measure for the mean cluster size. The growth of the network in the quenched case is shown in Figure 6.3a. As expected, C sharply increases initially, stabilizing after approximately 4 hours. The near-equilibrium assembly process shown in Figure 6.3b on the other hand clearly displays step-wise growth of the network: at each increased interaction strength, the system approaches a new equilibrium cluster size distribution.

We can also follow the progress of the assembly process using the normalized number of bonds in the system, or bond probability, p_b, defined as

$$p_\mathrm{b} = \langle Z \rangle / \langle f \rangle, \tag{6.1}$$

where $\langle Z \rangle$ is the average number of bonds per particle, and $\langle f \rangle$ is the average number of bonding sites per particle. $\langle f \rangle$ is simply equal to

$$\langle f \rangle = \frac{3N + 2L}{N + L}, \tag{6.2}$$

with N 3-valent particles and L 2-valent particles.

We plot the bond probability and together with the mean cluster size C in both the quenched and near-equilibrium growth in Figures 6.3a&b (right axis, hexagons). The bond probability reflects the trend of the mean cluster size C: the quenched system shows a smooth increase to a plateau value, while the near-equilibrium assembly route stabilizes at a constant p_b at every intermediate at-

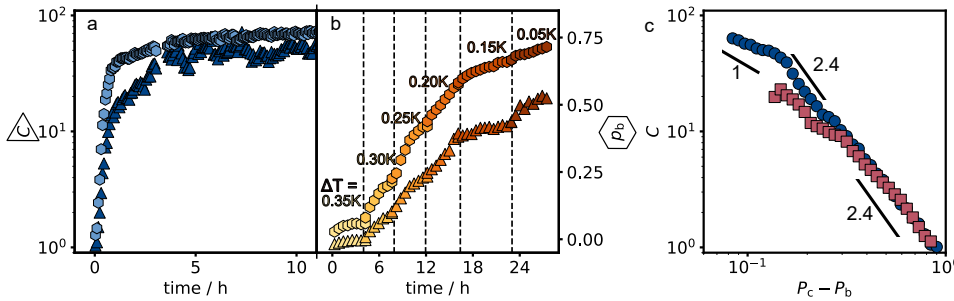

Figure 6.3 : Cluster evolution: quench and near-equilibrium assembly. The particles' assembly *via* the quench (a) and near-equilibrium (b) route is quantized by following the second moment of the cluster size distribution, C (left y-axis, triangles), and the bond probability, p_b (right y-axis, hexagons), as a function of time. In the near-equilibrium case (b), the stepped ΔT (attractive strength) from $0.35\,\mathrm{K}$ to $0.05\,\mathrm{K}$ is indicated by colour coding. In (c), we plot C as a function of distance to the predicted percolation threshold (p_c), for both the quench (blue circles) and near-equilibrium (red squares) route. The solid lines indicate power laws with exponents of 1 and 2.4.

tractive strength. Despite the very different routes to the final state, the eventual bond probability is remarkably similar in both systems: stabilization occurs at $p_b \approx 0.75$ at $\Delta T = 0.05\,\mathrm{K}$.

Percolation theory predicts that percolation occurs at the critical bond probability $p_c = \frac{1}{\langle f \rangle - 1} = \frac{1}{2\frac{1}{7} - 1} = \frac{7}{8}$ [205]. Curiously, both the quenched and near-equilibrium system are very close to percolation at the end of measurements, as illustrated by Figure 6.2d, however, the observed bond probability of $p_b \approx 0.75$ is significantly smaller than $p_b = \frac{7}{8} = 0.875$. This difference between predicted and observed percolation threshold is not entirely unexpected: the prevalence of loops in large clusters depresses the bond probability at which percolation takes place. Numerical simulations have encountered similar discrepancies between percolation theory and observation in 2D systems [211].

To check the scaling predictions of percolation theory, we plot the mean cluster size as a function of the distance to the theoretical critical bond probability ($p_c - p_b$) of both quench and near-equilibrium systems in Figure 6.3c. The mean cluster size initially increases as a power law with an exponent of 2.4, crossing over to an exponent of approximately 1 in the quench case at $p_c - p_b \approx 0.15$. The divergence approaching the critical point is expected from percolation theory: in a 2D system, C is expected to diverge with a critical exponent $\gamma = 43/18 \approx 2.4$,

crossing over to 1 close to p_c [206], in very good agreement with our observations. Unlike the quench route, the near-equilibrium route does not show a cross-over to a lower exponent, probably because it does not get close enough to the percolation threshold to observe this behaviour. The slight wobble in the data at $p_c - p_b \approx 0.3$ may be associated with the increased likelihood of the presence of rings, influencing the cluster size distribution. Besides this slight deviation, the agreement with percolation theory is striking.

6.3.4 Cluster Size Distributions

Beside some deviations closer to percolation, the quench and near-equilibrium routes show the same increase in mean cluster size with bond probability, suggesting that the system proceeds through the same aggregation states, uniquely defined by the particle geometry and system bond probability. To further investigate the similarity of both routes, we determine cluster size distributions and plot them for four different bond probabilities and both assembly paths in Figure 6.4.

Indeed, the experimental cluster size distributions overlap almost perfectly, confirming that we have experimentally realized an equilibrium gel, the physical properties of which do not depend on its history. With increasing bond probability, large clusters become increasingly likely, as seen by the right-shift of the tails in Figures 6.4a-d. Close to percolation, at $p_b = 0.73$, the cluster size distribution decreases as a power law with exponent $\tau = 2.16$, indicated by a black dotted line in Figure 6.4d. Percolation theory predicts that the number of large clusters of size s decreases as a power law with two-dimensional universal scaling constant $\tau = 187/91 \approx 2.05$ close to percolation [206]. Our experimentally determined value is only slightly off, indicating a good match with the theory; some deviation is expected due to the inclusion of small clusters in the fit (for which the relation is not expected to hold), the presence of loops in clusters, and possibly because we are not sufficiently close to percolation.

We can further compare our measured cluster size distributions with distributions found from FS theory. FS theory gives the number of clusters $N_{n,l}$ consisting of n 3- and l 2-valent particles as a function of bond probability as [205]:

$$N_{n,l} = N \frac{(1-p_b)^2}{\rho p_b} [\rho p_b (1-p_b)^2]^n [(1-\rho) p_b]^l \omega_{n,l}. \tag{6.3}$$

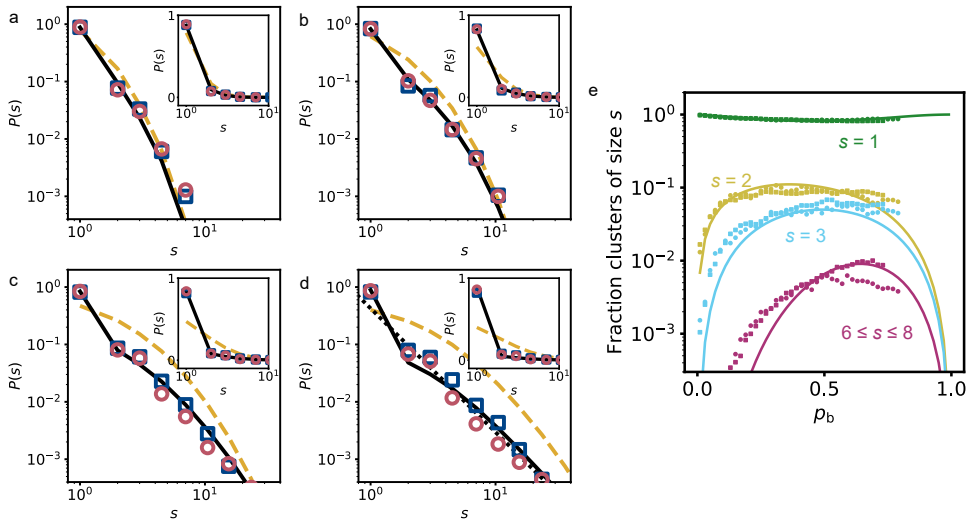

Figure 6.4 : Cluster size distribution: experiment and theory. We plot the cluster size distribution at four different bond probabilities: $p_b = 0.21$ (a), $p_b = 0.41$ (b), $p_b = 0.61$ (c), and $p_b = 0.73$ (d). In each graph, we show the distribution of cluster sizes for the quench (blue squares) and near-equilibrium (red circle) case, as well as the pure Flory-Stockmayer prediction (dashed yellow line) and the corrected Flory-Stockmayer prediction (black solid line). The insets show the same data, but plotted with a linear y-axis, to highlight the difference between pure and corrected Flory-Stockmayer predictions. In (d), the black dotted line indicates a power law with exponent $\tau = 2.16$. (e) To compare the cluster size distributions over the full range of bond probabilities, the fraction of clusters with size $s = 1$ (green), $s = 2$ (yellow), $s = 3$ (blue), and the average of clusters with size $6 \leq s \leq 8$ (burgundy) is plotted as a function of bond probability for the quenched (squares) and near-equilibrium (circles) systems, as well as the corrected FS predictions (solid lines).

Here, $\rho = \frac{3N}{3N+2L}$ is the probability that a randomly chosen patch belongs to an 3-valent particle. The combinatorial term $\omega_{n,l}$ accounts for the possible conformations of clusters of n 3-valent and l 2-valent particles, and is given by eq. 6.7. The cluster size distribution can thus be found for every given bond probability p_b.

Recent work [225] has shown that in our quasi-2D system, divalent particles exhibiting three-dimensional rotational motion have a lower chance of binding, because patches are not always pointing in plane, but are pointing towards the substrate or are pointing up. In this case, particles will not be able to bind, leading to deviations from FS theory. Luckily, a small correction to FS theory can be made to account for the effect: we define a fraction ζ of dipatch particles that are 'inactive' and will effectively remain monomers, appearing as clusters of size $s = 1$. We thus calculate $N_{n,l}$ (eq. 6.3), but correct for the number of inactive divalent particles $L_\mathrm{inactive} = \zeta \cdot L$, by subtracting them from the active particles $L_\mathrm{active} = L - L_\mathrm{inactive}$ and adding them to the number of monomers predicted by FS. Since ζ is hard to accurately estimate, we treat it as a fitting parameter. The full correction is treated comprehensively in section 6.5.2.

We plot the cluster size distributions obtained from uncorrected (dashed yellow line), and corrected FS theory (solid black line) in Figure 6.4a-d for four bond probabilities. The experimental data and the predictions from uncorrected FS theory show an increasingly large discrepancy for larger p_b. The largest difference between experimental data and theory is the number clusters with size $s = 1$: pure FS theory strongly underestimates the number of observed monomers, which is especially clear in the linear insets of Figure 6.4a-d. The corrected FS theory obtained by fitting the experimental data, with $\zeta = 0.436$ on the other hand agrees exceptionally well with the experimental data. Furthermore, an inactive 2-valent particle fraction of $\zeta = 0.436$ is reasonable based on our particle geometry and theory on a similar system [225].

We further compare the corrected FS model to experimental data over the full range of bond probabilities. In Figure 6.4e, we plot the fraction of clusters with size $s = 1$, $s = 2$, $s = 3$, and the average of $6 \leq s \leq 8$ as a function of bond probability. Again, we note the good overlap between the quenched (squares) and near-equilibrated (dots) datasets. The solid lines indicating the corrected FS predictions are in reasonable agreement with the experimental data. Deviations from FS theory are small, but easily identified due to the logarithmic y-scale of Figure 6.5a. At low bond probability, FS predictions underestimate the number

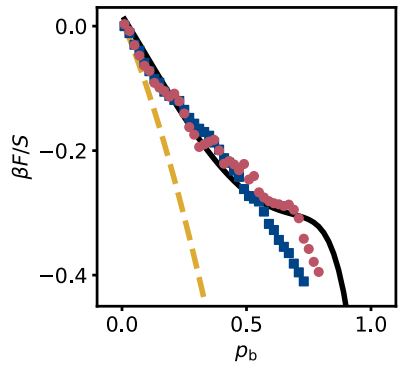

Figure 6.5 : Free energy as a function of bond probability. The Helmholtz free energy per particle is plotted as a function of the bond probability of the quenched (red circles) and near-equilibrium (blue squares) systems, as well as the theoretical predictions from FS with (solid black line) and without (dashed yellow line) correction. The free energy is determined from eq. 6.4, and solely dependent on the bonding state of the system.

of large clusters, probably because ζ is not a perfect descriptor of the correction we apply. Additionally, a breakdown of FS theory close to the critical point is expected [226], which we indeed observe.

6.3.5 Free Energy

We further make use of the remarkable properties of an equilibrium gel to directly relate the experimentally determined cluster size distribution to the free energy of the system. By considering our system as a 2-dimensional ideal gas of clusters, the Helmholtz free energy F can be expressed as

$$\beta F = N\beta\mu_N + L\beta\mu_L - \sum N_{n,l}, \tag{6.4}$$

where $\beta\mu_N = \ln \frac{N_{1,0}}{A}$ and $\beta\mu_L = \ln \frac{N_{0,1}}{A}$ are the chemical potentials of the tetra- and dipatch particle respectively with A the area, and $\Sigma N_{n,l}$ is the total number of clusters, see section 6.5.3. All parameters needed to obtain the free energy are related to the cluster size distribution, and thus directly observable in experiment. Therefore, we can easily determine the Helmholtz free energy as a function of bond probability, as shown in Figure 6.5. Again, the quench and near-equilibrium cases are strikingly comparable: the energies largely overlap. The system energy is calculated from cluster distributions derived from corrected and uncorrected

FS theory are in reasonable agreement with experimental results, as we expect based on the similar cluster size distributions shown in Figure 6.4e. At large bond probabilities, the quenched route appears to describe FS theory predictions better, although more experiments are needed to elucidate this point.

6.4 Conclusions

Our results convincingly show that this experimental system of divalent and pseudo-trivalent particles form an equilibrium gel. Moreover, experiments show that slowly increasing attractive strength does not lead to a different network architecture as a quick quench to high attractive strengths. While conventional colloidal gel material properties are strongly dependent on the formation history of the gel, the properties of our limited-valency system experiences little to no effect from its exact formation process. We determine several percolation exponents, and note on their remarkable match with predictions from percolation theory. We show that Flory-Stockmayer theory can quantitatively describe our system when we apply a small correction for the extra rotational degree of freedom of monomers for our pseudo-2D geometry. Finally, we show that the free energy of the system can be inferred from the network state directly observed in experiments, made possible due to the equilibrium nature of our gel.

The characteristics of limited-valency networks were predicted through theory and simulations over a decade ago, but experimental conformation has been hard to obtain. In this chapter, we have shown a simple system of patchy particles interacting via critical Casimir forces that display the characteristics predicted by *in silica* studies. Furthermore, our system is easily studied in real time using optical microscopy, opening the door to facile study of the formed architectures. Our results highlight the exceptional richness of patchy particle assembly: a relatively simple combination of di- and pseudo-trivalent particles can assemble into disordered networks with counterintuitive properties.

6.5 Appendix

6.5.1 Temperature-dependent Behaviour

In Figure 6.3b, we show the evolution of the mean cluster size C and bond probability p_b as a function of time in the near-equilibrium assembly case, which means we see the behaviour as a function of temperature, and thus attractive strength. A few other parameters change as a function of attractive strength that are not explicitly shown in the main text of this chapter. In Figure 6.6a, we show the evolution of the fraction of unreacted particles ($N_{s=1}$). As in Figure 6.3, we observe a clear stepwise evolution, especially at the lower attractive strengths. There, the faster equilibration takes place because the structures are much more dynamic at low interaction strength. This is examplified in Figure 6.6b, where we show the bond lifetime at the different temperatures. Clearly, at smaller ΔT (higher attractive strength), the bond lifetime is much higher, leading to much slower equilibration.

6.5.2 Correcting Flory-Stockmayer

Flory-Stockmayer theory can be used to predict all network properties as a function of the bond probability, like the number of clusters of a certain composition.

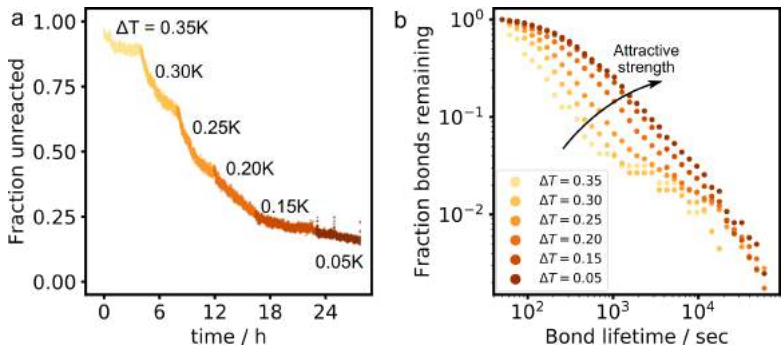

Figure 6.6 : Parameters as a function of ΔT in near-equilibrium assembly. (a) The fraction of particles that are not part of a larger structure as a function of time. Data is colour coded for the temperature. (b) The lifetime of patch-patch bonds at the temperatures visited in the near-equilibrium assembly process.

In this work, we are interested specifically in the number of clusters $N_{n,l}$ consisting of n f_N-valent particles, and l 2-valent particles; which is equal to [205]:

$$N_{n,l} = N\frac{(1-p_\mathrm{b})^2}{\rho p_\mathrm{b}}[\rho p_\mathrm{b}(1-p_\mathrm{b})^2]^n[(1-\rho)p_\mathrm{b}]^l\omega_{n,l}, \tag{6.5}$$

where $\rho = \frac{f_N N}{f_N N+2L}$ is the probability that a randomly chosen patch belongs to an f_N-valent particle. The combinatorial term $\omega_{n,l}$ accounts for the possible conformations of clusters of n f_N-valent and l 2-valent particles, and is given by:

$$\omega_{n,l} = f_N\frac{(l+f_N n-n)!}{l!n!(f_N n-2n+2)!}. \tag{6.6}$$

In our system, we have mix of 2- and 3-valent particles, so $f_N = 3$, meaning $\rho = \frac{3N}{3N+2L}$, as given in the main text, and the combinatorial term simplifies to:

$$\omega_{n,l} = \frac{3(l+2n)!}{l!n!(n+2)!}. \tag{6.7}$$

From our experimental bright-field microscopy images, the 2- and 3-valent particles cannot be distinguished. Therefore, it is convenient to focus on the distribution of total cluster sizes $s = n+l$, not individual combinations of n and l. To find the predicted number of clusters of a given size s, we use:

$$N_s = \sum_{i=0}^{s} N_{i,s-i}, \tag{6.8}$$

which for a cluster size of $s = 1$ is simply given by $N_s = N_{0,1} + N_{1,0}$. The cluster size distribution, which is easily determined experimentally, can thus also be found trough FS theory for every given bond probability p_b.

As mentioned in the main text, recent work [225] has shown that in our quasi-2D system, non-bonded divalent particles exhibiting three-dimensional rotational motion have a lower chance of binding, because patches are not always pointing in plane, but are pointing towards the substrate or are pointing up. In this case, particles will also not be able to bind. Both effects lead to deviations from FS theory.

Luckily, small corrections to FS theory can be made to account for the effect: we define a fraction ζ of dipatch particles that are 'inactive' and will effectively remain monomers, appearing as clusters of size $s = 1$. Practically, we calculate $N_{n,l}$ (eq. 6.3), but corrected for the effective number of active divalent particles, by taking

$$\rho' = \frac{3N}{3N + 2L(1-\zeta)}. \tag{6.9}$$

Furthermore, we add the inactive particles $L_{\text{inactive}} = \zeta \cdot L$ to the number of monomers predicted by FS:

$$N'_s = \begin{cases} \sum_{i=0}^{s} N'_{i,s-i} + L_{\text{inactive}} & \text{if } s = 1, \\ \sum_{i=0}^{s} N'_{i,s-i} & \text{if } s > 1. \end{cases} \tag{6.10}$$

Since ζ is hard to accurately estimate, we treat it as a fitting parameter.

6.5.3 Energy of Patchy Networks

If we assume our system is an ideal gas of clusters, we can directly infer the Helmholtz free energy of our system from its cluster size distribution.

The Helmholtz free energy (in units $k_\text{b}T$) is given by:

$$\beta F = \beta G - \beta PA, \tag{6.11}$$

with G the Gibbs free energy, and P and A the pressure and area respectively. In an ideal gas of clusters, βPA is simply equal to the number of observed clusters:

$$PA = k_\text{b}T \sum N_{n,l} \tag{6.12}$$

$$\beta PA = \sum N_{n,l}. \tag{6.13}$$

The Gibbs free energy can be expressed in terms of the chemical potential of our di- and tetrapatch particles. At low density, we can approximate the chemical

potential of a freely diffusing particle in two dimensions as the logarithm of the particle number density:

$$\mu^{s=1} = k_\mathrm{b}T \ln \frac{N}{A}, \tag{6.14}$$

Because of the extraordinary properties of our system, it can be assumed we are always in equilibrium, which means that the chemical potential of e.g. a freely diffusing non-bonded divalent particles must be equal to divalent particles in clusters [227, 228], so:

$$\mu_L^{s=1} = k_\mathrm{b}T \ln \frac{N_{0,1}}{A} = \mu_L^{s=2} = \mu_L^{s=3} = \dots \tag{6.15}$$

Therefore, the Gibbs free energy can be obtained in terms of quantities directly observable in our system:

$$\beta G = N\beta\mu_N + L\beta\mu_L \tag{6.16}$$

$$\beta G = N \ln \frac{N_{1,0}}{A} + L \ln \frac{N_{0,1}}{A}, \tag{6.17}$$

with $N_{1,0}$ the number of monomers that are tetrapatch particles, and $N_{0,1}$ the number of monomers that are dipatch particles, see eq. 6.3. By plugging in equations 6.13 and 6.17 into equation 6.11, we obtain:

$$\beta F = N \ln \frac{N_{1,0}}{A} + L \ln \frac{N_{0,1}}{A} - \sum N_{n,l}, \tag{6.18}$$

which is equivalent to eq. 6.4. The monomer counts $N_{1,0}$ and $N_{0,1}$ cannot be determined independently from experiment, since we cannot tell the difference between dipatch and tetrapatch particles from our microscopy images. However, since we know that the corrected FS theory describes our system well, we can use it to determine the number of 2- and 3-valent monomers. Eq. 6.10 describes the number of monomers as

$$N'_{s=1} = N_{0,1} + N_{1,0} + L_\mathrm{inactive}, \tag{6.19}$$

where $N'_{s=1}$ is the (measured) total number of monomers, $N_{0,1}$ is the number of 3-valent monomers, and $N_{1,0} + L_{\text{inactive}}$ is the number of 2-valent monomers. Using the fitted $\zeta = 0.436$, we can simply determine $L_{\text{inactive}} = \zeta L$. Using eq. 6.3 we can determine the ratio between $N_{1,0}$ and $N_{0,1}$, which we combine with the observed number of monomers to give the actual di- to trivalent particle ratio:

$$N_{1,0} = N\frac{(1-p_\text{b})^2}{\rho p_\text{b}}[\rho p_\text{b}(1-p_\text{b})^2] \tag{6.20}$$

$$N_{0,1} = N\frac{(1-p_\text{b})^2}{\rho p_\text{b}}[(1-\rho)p_\text{b}] \tag{6.21}$$

$$\frac{N_{1,0}}{N_{0,1}} = \frac{\rho}{1-\rho}(1-p_\text{b})^2 \tag{6.22}$$

$$N_{1,0} = \frac{N_{1,0}}{N_{0,1}}(S - L_{\text{inactive}}) \tag{6.23}$$

$$N_{0,1} = (S - L_{\text{inactive}}) - N_{1,0}. \tag{6.24}$$

7 Summary

> I've never seen the Icarus story as a lesson about the limitations of humans. I see it as a lesson about the limitations of wax as an adhesive.
>
> *Randall Munroe*

The properties of materials, like metals or plastics, are hard to explain when considering only their constituent particles (atoms and molecules): a purely reductionist approach fails. Instead, we must consider the complex interplay between all components: properties emerge from the collective behaviour of the system. Such emergent behaviour is ubiquitous in the natural world: from consciousness to protein folding, these behaviours are hard to explain even with a near-perfect understanding of the underlying principles and components. The process of self-assembly is a particularly interesting element of emergence, and the main topic of this thesis; relatively simple building blocks can assemble into complex, counterintuitive structures. Colloidal particles are a prime example of self-assembling building blocks: they are simple, well-understood spherical blobs, but together, a very wide range of unexpected behaviours emerge, assembling into a wide range of materials, from small, self-limiting clusters to larger superstructures, and from crystalline lattices to disordered gels.

In the past few years, significant advancements in colloidal synthesis have given us more synthetic control than ever over the composition and geometry of colloidal particles. Simulations and theory have shown that particles with specific shape and valency can be used to assemble highly controllable functional architectures that have specific, tunable material properties. A particularly exciting particle design is the so-called *patchy particle*, a particle decorated with patches of specific surface chemistry, with well-defined symmetry, allowing the reproduction of the specificity and geometry of atom-like valence bonds. Despite promising in

silica studies, experimental realization of complex structures using patchy particles has remained illusive, and promises remain largely unfulfilled. In this thesis, we take steps into this largely unexplored territory using a system of well-defined patchy particles with highly specific patch-to-patch attraction using the *critical Casimir force*, a solvent-mediated force that can easily be tuned with temperature. We assemble this system into a wide variety of colloidal structures, varying from small clusters to phase-spanning networks. Using optical microscopy, we study the assembly, dynamics, and other properties of the structures by tracking particles and their bonds.

We start small: in Chapter 3, we assemble small colloidal clusters with the same bonding geometry as alkanes. These *colloidal molecules*, assembled from di- and tetrameric patchy particles undergo the same chemical transformations as their atomic counterparts. Specifically colloidal cyclopentane shows interesting behaviour. By direct observation via optical microscopy, we reveal that the small colloidal cluster undergoes transitions between chair and twist conformations, just like in atomic cyclopentane. We elucidate the interplay of bond bending strain and entropy in the molecular transition states and ring-opening reactions. These results open the door to investigate complex molecular kinetics and molecular reactions in the high-temperature classical limit, in which the colloidal analogue becomes a good model.

We describe how we grow a similar patchy particle system into larger architectures in Chapter 4. One of the patches of tetravalent particles is bonded to the sample wall, leaving the three other patches free to bind other particles in-plane. This leads to the assembly of *colloidal graphene*, a honeycomb lattice of patchy particles. Direct observations of the growth, defects, and healing of the lattice grants us insight into what may occur during the growth process of atomic graphene, normally hidden due to the extreme conditions in which it takes place. These direct observations reveal that the origins of the most common defects lie in the early stages of graphene assembly, where pentagons are kinetically favoured over the equilibrium hexagons of the honeycomb lattice, subsequently stabilized during further growth.

In Chapter 5, we dive deeper into the system of pseudo-trivalent patchy particles confined to a plane and map the full phase diagram of the system. Apart from the colloidal graphene described comprehensively in Chapter 4, under certain conditions we observe the spontaneous formation of a triangular lattice and amorphous network. We investigate these unexpected condensed phases, revealing their

shared structural motifs. Combining results from simulations and experiment, we elucidate the origin of the three condensed phases and construct the phase diagram of the system. This chapter illustrates the rich phase behaviour a relatively simple patchy particle system can display.

Finally, Chapter 6 treats an unordered patchy particle superstructure: networks constructed from a mix of di- and pseudo-trivalent patchy particles. This network is a so-called *equilibrium gel*, and has some very counterintuitive properties: while the properties of a 'regular' colloidal gel strongly depend on the conditions of its formation, the history of an equilibrium network does not influence its eventual properties. On top of that, we can use a corrected Flory-Stockmayer theory to accurately describe and predict the behaviour of the system as a function of the normalized number of bonds.

The simple bonding geometry of carbon atoms is at the basis of materials ranging from wood to diamonds. In this thesis, we have taken the first steps on a similar path: we have experimentally explored the assembly of patchy colloids, and revealed how these precisely controllable building blocks can be used to assemble into a range of different structures. The continuous improvement in synthesis of patchy particles and their increasingly complex assembly shows that our control over microscopic assembly is ever-increasing. This exploratory work should be seen as the basis for the design of more advanced future smart materials, with precisely tunable mechanical, electronic and optical properties. Future 'colloidal architects' may have abilities approaching that of nature: with excellent control over the building blocks of a material comes excellent control over the macroscopic material properties.

8 Nederlandstalige samenvatting

> Alle verhalen eindigen gelukkig, als je maar op tijd stopt.
>
> *Annie M.G. Schmidt*

De eigenschappen van veelvoorkomende materialen, zoals plastic of hout, zijn lastig te verklaren als we alleen de moleculen en atomen waaruit het materiaal bestaat bekijken; een puur reductionistische aanpak werkt simpelweg niet. In plaats daarvan moeten we de interactie tussen alle componenten in een materiaal in beschouwing nemen: onverwachte eigenschappen kunnen namelijk ontstaan door het collectieve gedrag van het systeem. Dit zogenaamde *emergente* gedrag zien we vaak terug in ons dagelijks leven: fenomenen als het samenzwermen van vogels, het ontstaan van files, en zelfs ons bewustzijn, zijn lastig of onmogelijk te verklaren aan de hand van alleen de eigenschappen van de individuele componenten van een systeem. Zelfassemblage is een bijzonder interessant voorbeeld van een emergent fenomeen, en het onderwerp van dit proefschrift. Zelfassemblage vindt plaats als bouwstenen zich spontaan op een bepaalde manier ordenen, in bijvoorbeeld een specifiek patroon. Zelfs zeer simpele bouwstenen kunnen zich op zeer ingewikkelde manier ordenen. *Colloïdale deeltjes* zijn een goed voorbeeld - dit zijn simpele balletjes van tussen de 10 nanometer en 10 micrometer in doorsnede, typisch gemaakt van plastic - maar samen kunnen ze allerlei structuren aannemen. Afhankelijk van de omstandigheden (typisch door de deeltjes elkaar een beetje aan te laten trekken, bijna als magneetjes) kunnen ze zich ordenen in zeer regelmatige *colloïdale kristallen*, zoals je ziet in sommige edelstenen, waaronder opalen. Onder andere omstandigheden kunnen zich totaal andere structuren vormen, zoals willekeurig geordende netwerken, zogenaamde *colloïdale gels*, die je terugziet in veel cosmetica.

In de afgelopen jaren is er veel vooruitgang gemaakt in het produceren van colloïdale deeltjes, en we hebben meer controle over deeltjessamenstelling en -vorm dan ooit. Computersimulaties lijken erop te wijzen dat colloïdale deeltjes die op een beperkt aantal manieren aan elkaar kunnen plakken zich kunnen assembleren in materialen met interessante materiaaleigenschappen. Door de deeltjes aan te passen kunnen we de materiaaleigenschappen dan ook makkelijk veranderen. Een type colloïdaal deeltje dat deze voorspellingen wellicht waar kan maken zijn zogenaamde *lappendeeltjes* (*patchy particles* in het Engels). Deze lappendeeltjes hebben "lapjes" op hun oppervlak, gemaakt van een ander materiaal als de rest van het deeltje. Met behulp van de zogenaamde *kritische Casimir kracht* kunnen we de lapjes elkaar laten aantrekken. Dit leid tot een situatie waarin de lappendeeltjes zich min of meer gedragen als atomen: ze hebben een vast maximaal aantal deeltjes die zich aan elke deeltje kunnen binden, en alleen in specifieke richtingen.

Helaas blijft het bouwen van complexe structuren met behulp van lappendeeltjes erg uitdagend. Niet alleen is het maken van deeltjes met de juiste eigenschappen lastig, maar de assemblage zelf blijkt ook erg moeilijk. In dit proefschrift neem ik een aantal grote stappen op dit gebied. Ik bouw een aantal structuren, zowel grote als kleine, zowel geordend als ongeordend. Ik gebruik optische microscopie om de structuren en hun vorming, rijping en dynamica te bestuderen, door zoveel mogelijk bij te houden waar elk deeltje is, en met welke andere deeltjes het gebonden is.

In hoofdstuk 3 beschrijf ik experimenten waarin ik lappendeeltjes laat assembleren zodat zich kleine structuren vormen die dezelfde bindingsgeometrie hebben als moleculen. Deze zogenaamde *colloïdale moleculen*, bestaande uit lappendeeltjes met twee of vier lapjes, ondergaan soms dezelfde transformaties als hun atomaire tegenhangers. Vooral colloïdaal cyclopentaan, een ring van vijf deeltjes, vertoont gedrag dat verdacht veel lijkt op atomair cyclopentaan, een ring van vijf koolstofatomen: niet alleen hebben de twee analogen dezelfde kreukels, de conversie tussen twee typen kreukels vindt in beide gevallen plaats via hetzelfde mechanisme, de zogenaamde pseudorotaties. Daarnaast heeft een oppervlakte in de buurt van colloïdaal cyclopentaan een katalytisch effect: het bevorderd het uiteenvallen van het colloïdaal molecuul. Een vergelijkbaar effect bestaat in atomair cyclopentaan. Deze observaties tonen aan dat een colloïdaal modelsysteem onder bepaalde voorwaarden gebruikt kan worden om complex moleculair gedrag te onderzoeken.

In hoofdstuk 4&5 laat ik lappendeeltjes met vier lapjes assembleren, maar nu in veel grotere bouwwerken. We dwingen de bouwwerken om zich in twee dimensies

te ontwikkelen, door één van de vier lapjes te laten binden aan het oppervlakte van het glazen buisje, waar de colloïden in zitten. We zien dat drie verschillende structuren zich kunnen vormen, afhankelijk van de deeltjesdichtheid en de aantrekkingskracht tussen de lapjes. Ten eerste vormt zich een honinggraatkristal, *colloïdaal grafeen*, dat gevormd word door zich herhalende zeshoeken, waar elke hoek word gevormd door één deeltje dat drie andere deeltjes bind. In hoofdstuk 4 bestuderen we de groei, defecten, en dynamica van colloïdaal grafeen, omdat dat potentieel interessant is om atomair grafeen beter te begrijpen: atomair grafeen is lastig te observeren gedurende de assemblage. Ten tweede vinden we een amorf netwerk - een fase waarin elk lappendeeltje nog steeds zoveel mogelijk aan drie andere deeltjes bind, maar waar niet alleen zeshoeken, maar ook vijf- en zevenhoeken worden gevormd. Ten slotte vinden we een driehoekig kristal, waarbij elk deeltje door zes andere deeltjes word omringt, maar slecht aan drie deeltjes gebonden is door middel van lapjes. In hoofdstuk 5 bekijken we hoe deze drie fases zich onderscheiden, en wat de reden is dat ze überhaupt gevormd worden.

In hoofdstuk 6 beschrijf ik ten slotte de vorming van een netwerk bestaande uit deeltjes die elk twee andere deeltjes binden, en deeltjes die elk drie andere deeltjes binden. Dit netwerk is een zogenaamde *evenwichtsgel*, en heeft een aantal eigenschappen die niet voor de hand liggen. Waar de eigenschappen van een 'normale' gel altijd afhangen van hoe het gemaakt is, is dat niet het geval in een evenwichtsgel - het verleden van een evenwichtsgel is niet van invloed op zijn eigenschappen. Bovendien kunnen we het Flory-Stockmayer model gebruiken om de eigenschappen van de gel te voorspellen (na een kleine correctie).

De simpele bindingsgeometrie van koolstofatomen staat aan de basis van materialen met zeer verschillende eigenschappen, van hout tot diamant. In dit proefschrift heb ik geprobeerd om de eerste stappen te zetten op een vergelijkbaar pad: we hebben assemblage van lappendeeltjes experimenteel verkend, en laten zien hoe deze deeltjes in een grote variatie aan structuren kunnen assembleren. De continue verbetering in de synthese van lappendeeltjes en de daaraan gerelateerde verbreding van het aantal structuren dat gevormd kan worden met die deeltjes, laat zien dat onze controle over de microscopische wereld elke dag beter word. Dit proefschrift moet gezien worden als een eerste uitstapje in een wereld waarin precies-controleerbare materiaaleigenschappen werkelijkheid kunnen worden. Toekomstige 'colloïdale architecten' zijn wellicht even handig in het controleren van materiaaleigenschappen als de natuur dat is: met precieze controle over de bouwstenen van een materiaal, komt de precieze controle over het materiaal.

List of publications

As part of this thesis

Chapter 3: P.J.M. Swinkels, S.G. Stuij, Z. Gong, H. Jonas, N. Ruffino, B. van der Linden, P.G. Bolhuis, S. Sacanna, S. Woutersen & P. Schall. "Revealing pseudorotation and ring-opening reactions in colloidal organic molecules". In: *Nature Communications*, 12, 2810 (2021). DOI: 10.1038/s41467-021-23144-6.
P.J.M.S., S.G.S., S.W., and P.S. conceived the study. P.J.M.S. performed the experiments with help of N.R. and B.vdL. P.J.M.S analysed the data with help of N.R. H.J. and P.G.B. performed the simulations. Z.G. and S.S. made the particles. P.J.M.S. and P.S. wrote the manuscript. All authors discussed the data and reviewed the manuscript.

Chapter 4: P.J.M. Swinkels, Z. Gong, S. Sacanna, E.G. Noya & P. Schall. "Revealing defect dynamics in colloidal graphene". *Under review*.
P.J.M.S. and P.S. conceived the study. P.J.M.S. performed the experiments and analysed the data. Z.G. and S.S. made the particles. P.J.M.S. and P.S. wrote the manuscript. All authors discussed the data and reviewed the manuscript.

Chapter 5: P.J.M. Swinkels, Z. Gong, S. Sacanna, E.G. Noya & P. Schall. "Phases of surface-confined trivalent particles". *In preparation*.
P.J.M.S. and P.S. conceived the study. P.J.M.S. performed the experiments and analysed the data. Z.G. and S.S. made the particles. E.G.N. performed the simulations and their analysis. P.J.M.S. and P.S. wrote the manuscript. All authors discussed the data.

Chapter 6: P.J.M. Swinkels, J.C. Rouwhorst, R. Sinaasappel, Z. Gong, J.G. Eustace, W.V. Meyer, S. Sacanna, F. Sciortino & P. Schall. "Networks of limited-valency patchy particles". *In preparation*.
J.C.R., P.J.M.S. and P.S. conceived the study. R.S. and J.C.R. performed the experiments. P.J.M.S., J.C.R., and R.S. analysed the data. Z.G. and S.S. made the particles. P.J.M.S. and P.S. wrote the manuscript. All authors discussed the data.

Outside this work

- B. Gabryelczyk, H. Cai, X. Shi, Y. Sun, P.J.M. Swinkels, S. Salentinig, K. Pervushin & A. Miserez. "Hydrogen bond guidance and aromatic stacking drive liquid-liquid phase separation of intrinsically disordered histidine-rich peptides". In: *Nature Communications*, 10, 5465 (2019). DOI: 10.1038/s41467-019-13469-8.

- I.A. van Hees, P.J.M. Swinkels, R.G. Fokkink, A.H. Velders, I.K. Voets, J. van der Gucht & M. Kamperman. "Self-assembly of oppositely charged polyelectrolyte block copolymers containing short thermoresponsive blocks". In: *Polymer Chemistry*, 10, 3127-3134 (2019). DOI: 10.1039/C9PY00250B.

Acknowledgements

Let me start this section by saying that compiling these few pages took a lot more time than I had hoped - although it is probably the best read part of this booklet. The time I spent on this section is telling: I have received help, big or small, from quite a large group of people, too many to mention here (or in fact, too many for me to remember).

It hardly needs saying that without the help of my promotor, I would not be writing this text. *Peter* of all the people mentioned in this section, you deserve the most thanks - and by quite a lot. I have thoroughly enjoyed working with you in the past years, I hope I leave you with a similar experience. You have (almost) always let me just do what I thought was best, which is scary sometimes, but an invaluable experience. Our more-or-less weekly discussions were not only a source of your seemingly endless scientific ideas and help, but also managed to get me enthusiastic about whatever I was working on if necessary - your passion for science is infectious.

My closest colleagues are of course those participating in our colloid meetings. I am nostalgic to all those colloid meetings we had in the oxygen-depleted room, I am not sure what exactly made me enjoy these meetings so much, but I did. *Simon*, toen ik aankwam in Amsterdam was je de onbetwiste koning van de colloïde, en keek ik erg tegen je op. Wat dat betreft is er denk ik weinig veranderd. *Hannah*, toen ik je voor het eerst ontmoette in Han-sur-Lesse had ik geen idee dat we elkaar de komende 3 jaar wekelijks zouden zien - een welkome verrassing. Jij bent na mijn vertrek de meest ervaren colloïdale persoon, ik heb er geen twijfel over dat je die last zonder problemen zal dragen. *Nick*, I don't think you remember, but he first time we met, you called me 'old' and 'no longer fresh', a bold move considering you were applying for a job. Luckily, you charmed Hannah and Peter, and me too, be it a few weeks later. I wish you the best of luck with taming the patchy particles further. *Fuzhen*, when we are talking, I feel like you are always on some adventure where no-one really knows what is happening exactly - or why. I have enjoyed being part of some of the adventures, and wish you successful adventures in the future.

Janne-Mieke, ik ben erg blij dat we een tijdje veel hebben kunnen kletsen, zowel omdat dat erg gezellig was, en omdat je nu eenmaal een vrijwel onuitputtelijke bron van kennis en literatuur bent. Ik hoop dat we zo nu en dan nog een kopje thee kunnen drinken in de toekomst. *Peter Bolhuis*, ik kan veilig stellen dat jouw vlijmscherpe opmerkingen alle aanwezige van de colloid meeting wel eens aan het fundament van hun onderzoek hebben doen twijfelen. Hoewel dat niet per se fijn is, wens ik toekomstige generaties studenten hetzelfde toe: het is een erg nuttige ervaring. Of course, I extend my gratitude to all other unmentioned members of the colloid meeting, you have all contributed to this work, even if only for a single comment.

I also extend special thanks to the students I supervised over the years. *Léa*, I hope you enjoyed your time working with me - I enjoyed working with you! You try to hide it sometimes, but you are a hard worker and clever thinker. *Kasper*, ik was erg onder de indruk van je programmeer-skills, je wist duidelijk wat je aan het doen was, en dat is maar goed ook, gezien de lastige omstandigheden van je project. *Bram*, ik hoop dat je nog steeds even veel vragen stelt als toen je bij mij je BSc project begon, ik weet zeker dat je nieuwsgierigheid je goed van pas zal komen. *Nicola*, your initial patchy particle experiments and particle tracking skills have helped this thesis along tremendously, as you probably know very well.

When I arrived in Amsterdam to start my PhD, now over 4.5 years ago, I was very happy to find I had many nice colleagues - and many more nice ones have joined over the years. Thanks to the members of the Soft Matter group - *Antoine (yes, all variants), Ananya, David, Daan, Elham, Etiene, Felipe, Guillaume, Hans, Herish, Joep, Kasra, Martin, Marius, Manon, Melin, Menno, Nico, Riande, Rick, Rosa, Rozeline, Stefan, Thijs, Wenfeng, Yuri*, and all others which I fail to mention here or elsewhere in this section - for the good atmosphere, the support, and the nice conversations in the lab, during lunch, and in the office. I don't know half of you half as well as I should like, and I like less than half of you half as well as you deserve.

Doing routine work in the chemical lab always helps me think, so I guess I need to acknowledge *room D0.114* here, and a special thanks to those people who spend a chunk of time there with me: way too many to mention, ranging from BSc student to postdoc, from *Bas*, *Luci*, and *Marie*, who left only shortly after I joined, to *Azeza*, *Daphne*, and *Thekla*. *Paul*, your fight for a well-kept lab is commendable, but, I fear, in vain. It's a shame we've never really got to do a project together.

Another area where I spend a lot of time is, of course, our office, *C4.234*, where I sat throughout the entirety of my stay in Amsterdam, and where - despite the fact that its residents gradually changed over time - the atmosphere remained remarkably constant. Thanks to *Andreas, Bastiaan, Ellen, Heleen, Marion, Mohsin, Jackson, Romane, Rinse, Simon (the French one), Thijs*, and other (temporary) members of this select group for striking the right balance between complete silence and some chatting. *Marion*, I hope you did not take my occasional cynical comments too seriously - I promise you I enjoy(ed) my work.

I always enjoyed chatting with our friends in the *other* office. I hope the screams I heard through our shared wall were indicative of joy, not of frustration.

I can hardly skip over the *technical workshop* in this word of thanks, without whom our microscope would probably have disintegrated somewhere during my work in Amsterdam. *Gerrit* in particular cannot be praised enough for his Herculean effort.

Zhe and *Stefano*, we have never actually talked to each other in person, and I think it is pretty unlikely you will ever read this, but you have been absolutely critical for each part of my PhD. The particles you made for us were perfect in every way.

Bedankt *AmsteRIC 8*, gedachteloos roeien is een fijne afwisseling na een week vol geconcentreerd nadenken. Ik hoop dat mijn (zeer bewust geplande) gebrek aan concentratie tijdens het roeien niet te veel frustraties heeft opgeleverd.

Evelien, Gea, Ilona, Inge, Steven, Tess, Vincent en *WJ* bedankt! Ik zie jullie minder vaak dan ik graag zou willen, maar het leven zit zo nu en dan in de weg. Ik hoop dat we elkaar nog vaak zien, of het nu voor een online spel is, of voor een avontuur naar een wel heel vaag vakantiehuisje.

Ik denk dat dit proefschrift tot stand is gekomen met een mix van de *Van Den Boogaard* en *Swinkels* stijl van werken, dus beide families ontkomen niet aan een korte vermelding. Bedankt voor jullie interesse in dit werk, ik vond het erg leuk om jullie de binnenkant van de universiteit te laten zien.

Papa, Mama, Teun, (en natuurlijk *Muf* en *Flannagan*), bedankt dat thuis altijd thuis is gebleven. De afgelopen vijf jaar waren nu niet bepaald de makkelijkste, gelukkig had dat weinig met mijn PhD te maken. Hopelijk word het de komende jaren wat rustiger aan het thuisfront, ondanks mijn ongetwijfeld spannende toekomst.

Tess, ik ben je erg dankbaar voor al je steun en aanwezigheid. Ik heb stiekem best genoten van de periode dat onze eettafel omgetoverd werd in een kantoor -

het is duidelijk dat we de dagen prima kunnen vullen met kletsen over niets (en de consumptie van absurde hoeveelheden thee). Ik heb benieuwd wat de toekomst voor ons in petto heeft!

Bibliography

[1] Vinothan N. Manoharan. "Colloidal Matter: Packing, Geometry, and Entropy". In: *Science* 349.6251 (2015). DOI: 10.1126/science.1253751 (cit. on pp. 3, 42, 43).

[2] *Molecule*. In: *Merriam-Webster Dictionary*. Merriam-Webster, 2022. URL: https://www.merriam-webster.com/dictionary/molecule (cit. on p. 4).

[3] David C Rees, Thomas N Williams, and Mark T Gladwin. "Sickle-Cell Disease". In: *The Lancet* 376.9757 (2010), pp. 2018–2031. DOI: 10.1016/S0140-6736(10)61029-X (cit. on p. 5).

[4] Rees F. Garmann, Mauricio Comas-Garcia, Charles M. Knobler, and William M. Gelbart. "Physical Principles in the Self-Assembly of a Simple Spherical Virus". In: *Accounts of Chemical Research* 49.1 (2016), pp. 48–55. DOI: 10.1021/acs.accounts.5b00350 (cit. on p. 5).

[5] Martin Hofmann, Robert Anderssohn, Hans-Achim Bahr, Hans-Jürgen Weiß, and Jens Nellesen. "Why Hexagonal Basalt Columns?" In: *Physical Review Letters* 115.15 (2015), p. 154301. DOI: 10.1103/PhysRevLett.115.154301 (cit. on p. 6).

[6] Charlotte Aumeier, Laura Schaedel, Jérémie Gaillard, Karin John, Laurent Blanchoin, and Manuel Théry. "Self-Repair Promotes Microtubule Rescue". In: *Nature Cell Biology* 18.10 (10 2016), pp. 1054–1064. DOI: 10.1038/ncb3406 (cit. on p. 6).

[7] Alex W. Robertson, Barbara Montanari, Kuang He, Judy Kim, Christopher S. Allen, Yimin A. Wu, Jaco Olivier, Jan Neethling, Nicholas Harrison, Angus I. Kirkland, and Jamie H. Warner. "Dynamics of Single Fe Atoms in Graphene Vacancies". In: *Nano Letters* 13.4 (2013), pp. 1468–1475. DOI: 10.1021/nl304495v (cit. on p. 6).

[8] Roseanna N. Zia, Benjamin J. Landrum, and William B. Russel. "A Micro-Mechanical Study of Coarsening and Rheology of Colloidal Gels: Cage Building, Cage Hopping, and Smoluchowski's Ratchet". In: *Journal of Rheology* 58.5 (2014), pp. 1121–1157. DOI: 10.1122/1.4892115 (cit. on p. 7).

[9] J. Lyklema. *Fundamentals of Interface and Colloid Science. 4: Particulate Colloids*. Vol. 4. 5 vols. Fundamentals of Interface and Colloid Science. Elsevier, 2005. 692 pp. (cit. on pp. 7, 8, 11, 98).

[10] Wilson C. K. Poon. "Colloids as Big Atoms: The Genesis of a Paradigm". In: *Journal of Physics A: Mathematical and Theoretical* 49.40 (2016), p. 401001. DOI: 10.1088/1751-8113/49/40/401001 (cit. on p. 8).

[11] Jean Perrin. "Mouvement brownien et réalité moléculaire". In: *Annales de chimie et de physique*. 8th ser. 18 (1909), pp. 5–114 (cit. on p. 8).

[12] Laura Rossi, Stefano Sacanna, William T. M. Irvine, Paul M. Chaikin, David J. Pine, and Albert P. Philipse. "Cubic Crystals from Cubic Colloids". In: *Soft Matter* 7.9 (2011), pp. 4139–4142. DOI: 10.1039/C0SM01246G (cit. on p. 9).

[13] Anke Kuijk, Alfons van Blaaderen, and Arnout Imhof. "Synthesis of Monodisperse, Rodlike Silica Colloids with Tunable Aspect Ratio". In: *Journal of the American Chemical Society* 133.8 (2011), pp. 2346–2349. DOI: 10.1021/ja109524h (cit. on pp. 9, 10).

[14] Stephanie H. Lee and Chekesha M. Liddell. "Anisotropic Magnetic Colloids: A Strategy to Form Complex Structures Using Nonspherical Building Blocks". In: *Small* 5.17 (2009), pp. 1957–1962. DOI: 10.1002/smll.200900135 (cit. on pp. 9, 10).

[15] Jae Hwang Lee, Jonathan P. Singer, and Edwin L. Thomas. "Micro- / Nanostructured Mechanical Metamaterials". In: *Advanced Materials* 24.36 (2012), p. 4782. DOI: 10.1002/adma.201201644 (cit. on pp. 9, 13, 70, 81, 98).

[16] Amir A. Zadpoor. "Mechanical Meta-Materials". In: *Mater. Horiz.* 3.5 (2016), pp. 371–381. DOI: 10.1039/C6MH00065G (cit. on p. 9).

[17] Shin-Hyun Kim, Su Yeon Lee, Seung-Man Yang, and Gi-Ra Yi. "Self-Assembled Colloidal Structures for Photonics". In: *NPG Asia Materials* 3.1 (2011), pp. 25–33. DOI: 10.1038/asiamat.2010.192 (cit. on p. 9).

[18] Sharon C. Glotzer and Michael J. Solomon. "Anisotropy of Building Blocks and Their Assembly into Complex Structures". In: *Nature materials* 6.8 (2007), pp. 557–562. DOI: 10.1038/nmat1949 (cit. on p. 9).

[19] "Non-Spherical Particles". In: *Colloidal Suspension Rheology*. Ed. by Jan Mewis and Norman J. Wagner. Cambridge Series in Chemical Engineering. Cambridge: Cambridge University Press, 2011, pp. 155–179. DOI: 10.1017/CBO9780511977978.008 (cit. on pp. 9, 98).

[20] Janne-Mieke Meijer, Vera Meester, Fabian Hagemans, H.N.W. Lekkerkerker, Albert P. Philipse, and Andrei V. Petukhov. "Convectively Assembled Monolayers of Colloidal Cubes: Evidence of Optimal Packings". In: *Langmuir* 35.14 (2019), pp. 4946–4955. DOI: 10.1021/acs.langmuir.8b04330 (cit. on p. 9).

[21] Deshpremy Mukhija and Michael J. Solomon. "Nematic Order in Suspensions of Colloidal Rods by Application of a Centrifugal Field". In: *Soft Matter* 7.2 (2011), pp. 540–545. DOI: 10.1039/C0SM00493F (cit. on p. 10).

[22] Qian Chen, Sung Chul Bae, and Steve Granick. "Directed Self-Assembly of a Colloidal Kagome Lattice". In: *Nature* 469.7330 (2011), pp. 381–384. DOI: 10.1038/nature09713 (cit. on pp. 10, 12, 71).

[23] Daniel Morphew, James Shaw, Christopher Avins, and Dwaipayan Chakrabarti. "Programming Hierarchical Self-Assembly of Patchy Particles into Colloidal Crystals via Colloidal Molecules". In: *ACS Nano* 12.3 (2018), pp. 2355–2364. DOI: 10.1021/acsnano.7b07633 (cit. on pp. 10, 98).

[24] Mingxin He, Johnathon P. Gales, Étienne Ducrot, Zhe Gong, Gi-Ra Yi, Stefano Sacanna, and David J. Pine. "Colloidal Diamond". In: *Nature* 585.7826 (7826 2020), pp. 524–529. DOI: 10.1038/s41586-020-2718-6 (cit. on pp. 10, 12, 71).

[25] Eva G. Noya, Itziar Zubieta, David J. Pine, and Francesco Sciortino. "Assembly of Clathrates from Tetrahedral Patchy Colloids with Narrow Patches". In: *The Journal of Chemical Physics* 151.9 (2019), p. 094502. DOI: 10.1063/1.5109382 (cit. on pp. 10, 12, 42, 45, 71, 78, 98).

[26] Eva G. Noya, Noé G. Almarza, and Enrique Lomba. "Assembly of Trivalent Particles under Confinement: From an Exotic Solid Phase to a Liquid Phase at Low Temperature". In: *Soft Matter* 13.17 (2017), pp. 3221–3229. DOI: 10.1039/C7SM00217C (cit. on pp. 10, 73, 98, 104).

[27] Mingzhu Liu, Xiaolong Zheng, Veronica Grebe, David J. Pine, and Marcus Weck. "Tunable Assembly of Hybrid Colloids Induced by Regioselective Depletion". In: *Nature Materials* (2020), pp. 1–8. DOI: 10.1038/s41563-020-0744-2 (cit. on pp. 10, 13, 14, 99).

[28] Qian Chen, Jonathan K. Whitmer, Shan Jiang, Sung Chul Bae, Erik Luijten, and Steve Granick. "Supracolloidal Reaction Kinetics of Janus Spheres". In: *Science* 331.6014 (2011), pp. 199–202. DOI: 10.1126/science.1197451 (cit. on p. 10).

[29] John Russo, Piero Tartaglia, and Francesco Sciortino. "Reversible Gels of Patchy Particles: Role of the Valence". In: *The Journal of Chemical Physics* 131.1 (2009), p. 014504. DOI: 10.1063/1.3153843 (cit. on p. 10).

[30] Akira Kose, Masataka Ozaki, Kaoru Takano, Yoko Kobayashi, and Sei Hachisu. "Direct Observation of Ordered Latex Suspension by Metallurgical Microscope". In: *Journal of Colloid and Interface Science* 44.2 (1973), pp. 330–338. DOI: 10.1016/0021-9797(73)90224-5 (cit. on p. 11).

[31] P. N. Pusey and W. van Megen. "Phase Behaviour of Concentrated Suspensions of Nearly Hard Colloidal Spheres". In: *Nature* 320.6060 (6060 1986), pp. 340–342. DOI: 10.1038/320340a0 (cit. on pp. 11, 70).

[32] R. Buscall, P. D. A. Mills, and G. E. Yates. "Viscoelastic Properties of Strongly FlocculatedPolystyrene LatexDispersions". In: *Colloids and Surfaces* 18.2 (1986), pp. 341–358. DOI: 10.1016/0166-6622(86)80322-5 (cit. on p. 11).

[33] Robert J Pugh and Lennart Bergström. *Surface and Colloid Chemistry in Advanced Ceramics Processing*. 1st ed. Vol. 51. Surfactant Science. CRC Press, 1994. DOI: 10.1201/9780203737842 (cit. on p. 11).

[34] C. P. Collier, T. Vossmeyer, and J. R. Heath. "Nanocrystal Superlattices". In: *Annual Review of Physical Chemistry* 49.1 (1998), pp. 371–404. DOI: 10.1146/annurev.physchem.49.1.371 (cit. on p. 11).

[35] C. B. Murray, C. R. Kagan, and M. G. Bawendi. "Synthesis and Characterization of Monodisperse Nanocrystals and Close-Packed Nanocrystal Assemblies". In: *Annual Review of Materials Science* 30.1 (2000), pp. 545–610. DOI: 10.1146/annurev.matsci.30.1.545 (cit. on p. 11).

[36] D. V. Talapin, E. V. Shevchenko, A. Kornowski, N. Gaponik, M. Haase, A. L. Rogach, and H. Weller. "A New Approach to Crystallization of CdSe Nanoparticles into Ordered Three-Dimensional Superlattices". In: *Advanced Materials* 13.24 (2001), pp. 1868–1871. DOI: 10.1002/1521-4095(200112)13:24<1868::AID-ADMA1868>3.0.CO;2-0 (cit. on p. 11).

[37] Cherry A. Murray and David G. Grier. "Video Microscopy of Monodisperse Colloidal Systems". In: *Annual Review of Physical Chemistry* 47.1 (1996), p. 421. DOI: 10.1146/annurev.physchem.47.1.421 (cit. on p. 11).

[38] David R. Nelson. "Toward a Tetravalent Chemistry of Colloids". In: *Nano Letters* 2.10 (2002), pp. 1125–1129. DOI: 10.1021/nl0202096 (cit. on p. 11).

[39] Zhenli Zhang, Aaron S. Keys, Ting Chen, and Sharon C. Glotzer. "Self-Assembly of Patchy Particles into Diamond Structures through Molecular Mimicry". In: *Langmuir* 21.25 (2005), pp. 11547–11551. DOI: 10.1021/la0513611 (cit. on pp. 11, 12).

[40] Emanuela Bianchi, Julio Largo, Piero Tartaglia, Emanuela Zaccarelli, and Francesco Sciortino. "Phase Diagram of Patchy Colloids: Towards Empty Liquids". In: *Physical Review Letters* 97.16 (2006), p. 168301. DOI: 10.1103/PhysRevLett.97.168301 (cit. on pp. 11, 122).

[41] K. M. Ho, C. T. Chan, and C. M. Soukoulis. "Existence of a Photonic Gap in Periodic Dielectric Structures". In: *Physical Review Letters* 65.25 (1990), pp. 3152–3155. DOI: 10.1103/PhysRevLett.65.3152 (cit. on p. 12).

[42] Martin Maldovan and Edwin L. Thomas. "Diamond-Structured Photonic Crystals". In: *Nature Materials* 3.9 (9 2004), pp. 593–600. DOI: 10.1038/nmat1201 (cit. on p. 12).

[43] Daniel F. Tracey, Eva G. Noya, and Jonathan P. K. Doye. "Programming Patchy Particles to Form Complex Periodic Structures". In: *The Journal of Chemical Physics* 151.22 (2019), p. 224506. DOI: 10.1063/1.5128902 (cit. on pp. 12, 42).

[44] Abhishek B. Rao, James Shaw, Andreas Neophytou, Daniel Morphew, Francesco Sciortino, Roy L. Johnston, and Dwaipayan Chakrabarti. "Leveraging Hierarchical Self-Assembly Pathways for Realizing Colloidal Photonic Crystals". In: *ACS Nano* 14.5 (2020), pp. 5348–5359. DOI: 10.1021/acsnano.9b07849 (cit. on pp. 12, 71, 78).

[45] Dan Liu, Yihua Gao, Aihong Tong, and Sen Hu. "Absolute Photonic Band Gap in 2D Honeycomb Annular Photonic Crystals". In: *Physics Letters A* 379.3 (2015), pp. 214–217. DOI: 10.1016/j.physleta.2014.11.030 (cit. on pp. 13, 70, 81).

[46] Simon Yves, Fabrice Lemoult, Mathias Fink, and Geoffroy Lerosey. "Crystalline Soda Can Metamaterial Exhibiting Graphene-like Dispersion at Subwavelength Scale". In: *Scientific Reports* 7.1 (1 2017), p. 15359. DOI: 10.1038/s41598-017-15335-3 (cit. on pp. 13, 81).

[47] D. Chen, G. Zhang, and S. Torquato. "Inverse Design of Colloidal Crystals via Optimized Patchy Interactions". In: *The Journal of Physical Chemistry B* 122.35 (2018), pp. 8462–8468. DOI: 10.1021/acs.jpcb.8b05627 (cit. on pp. 13, 81).

[48] Emanuela Zaccarelli. "Colloidal Gels: Equilibrium and Non-Equilibrium Routes". In: *Journal of Physics: Condensed Matter* 19.32 (2007), p. 323101. DOI: 10.1088/0953-8984/19/32/323101 (cit. on pp. 13, 122).

[49] Francesco Sciortino and Emanuela Zaccarelli. "Equilibrium Gels of Limited Valence Colloids". In: *Current Opinion in Colloid & Interface Science* 30 (2017), pp. 90–96. DOI: 10.1016/j.cocis.2017.06.001 (cit. on pp. 13, 122, 123).

[50] Yufeng Wang, Yu Wang, Dana R. Breed, Vinothan N. Manoharan, Lang Feng, Andrew D. Hollingsworth, Marcus Weck, and David J. Pine. "Colloids with Valence and Specific Directional Bonding". In: *Nature* 491.7422 (2012), pp. 51–55. DOI: 10.1038/nature11564 (cit. on pp. 13, 14, 42, 70).

[51] Simon Stuij, Joep Rouwhorst, Hannah J. Jonas, Nicola Ruffino, Zhe Gong, Stefanno Sacanna, Peter G. Bolhuis, and Peter Schall. "Revealing Polymerization Kinetics with Colloidal Dipatch Particles". In: *Physical Review Letters* 127.10 (2021), p. 108001. DOI: 10.1103/PhysRevLett.127.108001 (cit. on pp. 13, 14, 70).

[52] Angus McMullen, Miranda Holmes-Cerfon, Francesco Sciortino, Alexander Y. Grosberg, and Jasna Brujic. "Freely Jointed Polymers Made of Droplets". In: *Physical Review Letters* 121.13 (2018), p. 138002. DOI: 10.1103/PhysRevLett.121.138002 (cit. on p. 13).

[53] Xiaolong Zheng, Yufeng Wang, Yu Wang, David J. Pine, and Marcus Weck. "Thermal Regulation of Colloidal Materials Architecture through Orthogonal Functionalizable Patchy Particles". In: *Chemistry of Materials* 28.11 (2016), p. 3984. DOI: 10.1021/acs.chemmater.6b01313 (cit. on p. 13).

[54] Rebecca W. Perry, Miranda C. Holmes-Cerfon, Michael P. Brenner, and Vinothan N. Manoharan. "Two-Dimensional Clusters of Colloidal Spheres: Ground States, Excited States, and Structural Rearrangements". In: *Physical Review Letters* 114.22 (2015), p. 228301. DOI: 10.1103/PhysRevLett.114.228301 (cit. on p. 14).

[55] Junwei Wang, Chrameh Fru Mbah, Thomas Przybilla, Benjamin Apeleo Zubiri, Erdmann Spiecker, Michael Engel, and Nicolas Vogel. "Magic Number Colloidal Clusters as Minimum Free Energy Structures". In: *Nature Communications* 9.1 (2018), p. 5259. DOI: 10.1038/s41467-018-07600-4 (cit. on p. 14).

[56] Yaroslav A. Urzhumov, Gennady Shvets, Jonathan A. Fan, Federico Capasso, Daniel Brandl, and Peter Nordlander. "Plasmonic Nanoclusters: A Path towards Negative-Index Metafluids". In: *Optics Express* 15.21 (2007), pp. 14129–14145. DOI: 10.1364/oe.15.014129 (cit. on p. 14).

[57] Jonathan A. Fan, Chihhui Wu, Kui Bao, Jiming Bao, Rizia Bardhan, Naomi J. Halas, Vinothan N. Manoharan, Peter Nordlander, Gennady Shvets, and Federico Capasso. "Self-Assembled Plasmonic Nanoparticle Clusters". In: *Science* 328.5982 (2010), pp. 1135–1138. DOI: 10.1126/science.1187949 (cit. on p. 14).

[58] Yufeng Wang, Yufeng Wang, Xiaolong Zheng, Gi-Ra Yi, Stefano Sacanna, David J. Pine, and Marcus Weck. "Three-Dimensional Lock and Key Colloids". In: *Journal of the American Chemical Society* 136.19 (2014), pp. 6866–6869. DOI: 10.1021/ja502699p (cit. on pp. 14, 20).

[59] Songbo Ni, Jessica Leemann, Ivo Buttinoni, Lucio Isa, and Heiko Wolf. "Programmable Colloidal Molecules from Sequential Capillarity-Assisted Particle Assembly". In: *Science Advances* 2.4 (2016), e1501779. DOI: 10.1126/sciadv.1501779 (cit. on pp. 14, 42).

[60] Pierre-Etienne Rouet, Cyril Chomette, Etienne Duguet, and Serge Ravaine. "Colloidal Molecules from Valence-Endowed Nanoparticles by Covalent Chemistry". In: *Angewandte Chemie International Edition* 57.48 (2018), pp. 15754–15757. DOI: 10.1002/anie.201809895 (cit. on pp. 14, 42).

[61] Theodore Hueckel, Glen M. Hocky, and Stefano Sacanna. "Total Synthesis of Colloidal Matter". In: *Nature Reviews Materials* 6.11 (2021), pp. 1053–1069. DOI: 10.1038/s41578-021-00323-x (cit. on pp. 14, 98).

[62] Ruben W. Verweij, Pepijn G. Moerman, Loes P. P. Huijnen, Nathalie E. G. Ligthart, Indrani Chakraborty, Jan Groenewold, Willem Kegel, Alfons van Blaaderen, and Daniela J. Kraft. "Conformations and Diffusion of Flexibly Linked Colloidal Chains". In: *Journal of Physics: Materials* 4.3 (2021), p. 035002. DOI: 10.1088/2515-7639/abf571 (cit. on p. 14).

[63] Mehdi B. Zanjani, Ian C. Jenkins, John C. Crocker, and Talid Sinno. "Colloidal Cluster Assembly into Ordered Superstructures via Engineered Directional Binding". In: *ACS Nano* 10.12 (2016), pp. 11280–11289. DOI: 10.1021/acsnano.6b06415 (cit. on p. 14).

[64] Seigou Kawaguchi and Koichi Ito. "Dispersion Polymerization". In: *Advances in Polymer Science*. Vol. 175. 2005, pp. 299–328. DOI: 10.1007/b100118 (cit. on p. 20).

[65] Peter A. Lovell and F. Joseph Schork. "Fundamentals of Emulsion Polymerization". In: *Biomacromolecules* 21.11 (2020), pp. 4396–4441. DOI: 10.1021/acs.biomac.0c00769 (cit. on p. 20).

[66] Rongchao Jin, Chenjie Zeng, Meng Zhou, and Yuxiang Chen. "Atomically Precise Colloidal Metal Nanoclusters and Nanoparticles: Fundamentals and Opportunities". In: *Chemical Reviews* 116.18 (2016), pp. 10346–10413. DOI: 10.1021/acs.chemrev.5b00703 (cit. on p. 20).

[67] Zhe Gong, Theodore Hueckel, Gi Ra Yi, and Stefano Sacanna. "Patchy Particles Made by Colloidal Fusion". In: *Nature* 550.7675 (2017), pp. 234–238. DOI: 10.1038/nature23901 (cit. on pp. 20, 42, 43, 70, 71, 98, 99).

[68] Young Sang Cho, Gi Ra Yi, Shin Hyun Kim, Seog Jin Jeon, Mark T. Elsesser, Hyung Kyun Yu, Seung Man Yang, and David J. Pine. "Particles with Coordinated Patches or Windows from Oil-in-Water Emulsions". In: *Chemistry of Materials* 19.13 (2007), pp. 3183–3193. DOI: 10.1021/cm070051w (cit. on p. 20).

[69] Vera Meester, Ruben W. Verweij, Casper Van Der Wel, and Daniela J. Kraft. "Colloidal Recycling: Reconfiguration of Random Aggregates into Patchy Particles". In: *ACS Nano* 10.4 (2016), pp. 4322–4329. DOI: 10.1021/acsnano.5b07901 (cit. on p. 20).

[70] Weiya Li, Hervé Palis, Rémi Mérindol, Jérôme Majimel, Serge Ravaine, and Etienne Duguet. "Colloidal Molecules and Patchy Particles: Complementary Concepts, Synthesis and Self-Assembly". In: *Chemical Society Reviews* 49.6 (2020), pp. 1955–1976. DOI: 10.1039/C9CS00804G (cit. on p. 20).

[71] Serge Ravaine and Etienne Duguet. "Synthesis and Assembly of Patchy Particles: Recent Progress and Future Prospects". In: *Current Opinion in Colloid & Interface Science* 30 (2017), pp. 45–53. DOI: 10.1016/j.cocis.2017.05.002 (cit. on p. 20).

[72] Kyung Ho Roh, David C. Martin, and Joerg Lahann. "Triphasic Nanocolloids". In: *Journal of the American Chemical Society* 128.21 (2006), pp. 6796–6797. DOI: 10.1021/ja060836n (cit. on p. 20).

[73] Adeline Perro, Stéphane Reculusa, Serge Ravaine, Elodie Bourgeat-Lami, and Etienne Duguet. "Design and Synthesis of Janus Micro- and Nanoparticles". In: *Journal of Materials Chemistry* 15.35-36 (2005), pp. 3745–3760. DOI: 10.1039/B505099E (cit. on p. 20).

[74] Rachelle M Choueiri, Elizabeth Galati, Héloïse Thérien-Aubin, Anna Klinkova, Egor M. Larin, Ana Querejeta-Fernández, Lili Han, Huolin L. Xin, Oleg Gang, Ekaterina B. Zhulina, Michael Rubinstein, and Eugenia Kumacheva. "Surface Patterning of Nanoparticles with Polymer Patches". In: *Nature* 538.7623 (7623 2016), pp. 79–83. DOI: 10.1038/nature19089 (cit. on p. 20).

[75] André H. Gröschel, Andreas Walther, Tina I. Löbling, Felix H. Schacher, Holger Schmalz, and Axel H. E. Müller. "Guided Hierarchical Co-Assembly of Soft Patchy Nanoparticles". In: *Nature* 503.7475 (7475 2013), pp. 247–251. DOI: 10.1038/nature12610 (cit. on p. 20).

[76] Huixin Bao, Wolfgang Peukert, and Robin Klupp Taylor. "One-Pot Colloidal Synthesis of Plasmonic Patchy Particles". In: *Advanced Materials* 23.22-23 (2011), pp. 2644–2649. DOI: 10.1002/adma.201100698 (cit. on p. 20).

[77] Xiuyang Xia, Hao Hu, Massimo Pica Ciamarra, and Ran Ni. "Linker-Mediated Self-Assembly of Mobile DNA-coated Colloids". In: *Science Advances* 6.21 (2020), eaaz6921. DOI: 10.1126/sciadv.aaz6921 (cit. on p. 23).

[78] Kun Zhao and Thomas G. Mason. "Assembly of Colloidal Particles in Solution". In: *Reports on Progress in Physics* 81.12 (2018), p. 126601. DOI: 10.1088/1361-6633/aad1a7 (cit. on p. 23).

[79] Bhuvnesh Bharti and Orlin D. Velev. "Assembly of Reconfigurable Colloidal Structures by Multidirectional Field-Induced Interactions". In: *Langmuir* 31.29 (2015), pp. 7897–7908. DOI: 10.1021/la504793y (cit. on p. 23).

[80] V D Nguyen, M T Dang, T A Nguyen, and P Schall. "Critical Casimir Forces for Colloidal Assembly". In: *Journal of Physics: Condensed Matter* 28.4 (2016), p. 043001. DOI: 10.1088/0953-8984/28/4/043001 (cit. on p. 24).

[81] A. Gambassi, A. Maciołek, C. Hertlein, U. Nellen, L. Helden, C. Bechinger, and S. Dietrich. "Critical Casimir Effect in Classical Binary Liquid Mixtures". In: *Physical Review E* 80.6 (2009), p. 061143. DOI: 10.1103/PhysRevE.80.061143 (cit. on p. 25).

[82] S. G. Stuij, M. Labbé-Laurent, T. E. Kodger, A. Maciołek, and P. Schall. "Critical Casimir Interactions between Colloids around the Critical Point of Binary Solvents". In: *Soft Matter* 13.31 (2017), pp. 5233–5249. DOI: 10.1039/C7SM00599G (cit. on pp. 25, 45, 58, 76, 87, 115).

[83] Andrea Pelissetto and Ettore Vicari. "Critical Phenomena and Renormalization-Group Theory". In: *Physics Reports* 368.6 (2002), pp. 549–727. DOI: 10.1016/S0370-1573(02)00219-3 (cit. on p. 25).

[84] Michael E. Fisher and Pierre GD Gennes. “Wall Phenomena in a Critical Binary Mixture”. In: *Comptes Rendus Hebdomadaires Des Seances De L Academie Des Sciences Serie B* 287.8 (1978), pp. 207–209 (cit. on p. 25).

[85] C Hertlein, L Helden, A Gambassi, S Dietrich, and C Bechinger. “Direct Measurement of Critical Casimir Forces”. In: *Nature* 451 (January 2008). DOI: 10.1038/nature06443 (cit. on p. 25).

[86] S. Z. Mirzaev, R. Behrends, T. Heimburg, J. Haller, and U. Kaatze. “Critical Behavior of 2,6-Dimethylpyridine-Water: Measurements of Specific Heat, Dynamic Light Scattering, and Shear Viscosity”. In: *Journal of Chemical Physics* 124.14 (2006). DOI: 10.1063/1.2188396 (cit. on pp. 28, 29, 73, 99).

[87] Arnold Stein, Steven J. Davidson, Joseph C. Allegra, and Guy F. Allen. “Tracer Diffusion and Shear Viscosity for the System 2,6-Lutidine-Water near the Lower Critical Point”. In: *The Journal of Chemical Physics* 56.12 (1972), pp. 6164–6168. DOI: 10.1063/1.1677168 (cit. on p. 29).

[88] Erdoğan Gülari, A. F. Collings, R. L. Schmidt, and C. J. Pings. “Light Scattering and Shear Viscosity Studies of the Binary System 2,6-Lutidine-Water in the Critical Region”. In: *The Journal of Chemical Physics* 56.12 (1972), pp. 6169–6179. DOI: 10.1063/1.1677169 (cit. on p. 29).

[89] Stanislaw Warycha and J. Howard Rytting. “Vapor Pressure Studies of Pyridine, Picolines and 2,6-Lutidine in Isooctane”. In: *Journal of Solution Chemistry* 13.8 (1984), pp. 589–598. DOI: 10.1007/BF00647227 (cit. on p. 29).

[90] Carlos A. Grattoni, Richard A. Dawe, C. Yen Seah, and Jane D. Gray. “Lower Critical Solution Coexistence Curve and Physical Properties (Density, Viscosity, Surface Tension, and Interfacial Tension) of 2,6-Lutidine + Water”. In: *Journal of Chemical & Engineering Data* 38.4 (1993), pp. 516–519. DOI: 10.1021/je00012a008 (cit. on p. 29).

[91] Y. Jayalakshmi, J. S. Van Duijneveldt, and D. Beysens. “Behavior of Density and Refractive Index in Mixtures of 2,6-Lutidine and Water”. In: *The Journal of Chemical Physics* 100.1 (1994), pp. 604–609. DOI: 10.1063/1.466921 (cit. on p. 29).

[92] John C. Clunie and James K. Baird. “Interdiffusion Coefficient and Dynamic Viscosity for the Mixture 2,6-Lutidine + Water near the Lower Consolute Point”. In: *Physics and Chemistry of Liquids* 37.4 (1999), pp. 357–371. DOI: 10.1080/00319109908031441 (cit. on p. 29).

[93] Liu-Cheng Wang, Hai-Sheng Xu, Jian-Hong Zhao, Cheng-Ying Song, and Fu-An Wang. "Density and Viscosity of (3-Picoline+water) Binary Mixtures from T=(293.15 to 343.15) K". In: *The Journal of Chemical Thermodynamics* 37.5 (2005), pp. 477–483. DOI: 10.1016/j.jct.2004.11.009 (cit. on p. 29).

[94] Wojciech Marczak. "Speed of Ultrasound, Density, and Adiabatic Compressibility for 2-Methylpyridine + Heavy Water in the Temperature Range 293 K to 313 K". In: *Journal of Chemical and Engineering Data* 44.3 (1999), pp. 621–625. DOI: 10.1021/je980285j (cit. on p. 29).

[95] T. Anh Nguyen, Arthur Newton, Daniela Kraft, Peter Bolhuis, and Peter Schall. "Tuning Patchy Bonds Induced by Critical Casimir Forces". In: *Materials* 10.11 (2017), p. 1265. DOI: 10.3390/ma10111265 (cit. on p. 29).

[96] Nobuyuki Ito, Tsunetake Fujiyama, and Yasuo Udagawa. "A Study of Local Structure Formation in Binary Solutions of 2-Butoxyethanol and Water by Rayleigh Scatterring and Raman Spectra". In: *Bulletin of the Chemical Society of Japan* 56.2 (1983), pp. 379–385. DOI: 10.1246/bcsj.56.379 (cit. on p. 29).

[97] T. Lapp, M. Rohloff, J. Vollmer, and B. Hof. "Particle Tracking for Polydisperse Sedimenting Droplets in Phase Separation". In: *Experiments in Fluids* 52.5 (2012), pp. 1187–1200. DOI: 10.1007/s00348-011-1243-7 (cit. on p. 29).

[98] Umberto Capasso Palmiero, Azzurra Agostini, Enrico Lattuada, Simone Gatti, Jaspreet Singh, Christopher Thomas Canova, Stefano Buzzaccaro, and Davide Moscatelli. "Use of RAFT Macro-Surfmers for the Synthesis of Transparent Aqueous Colloids with Tunable Interactions". In: *Soft Matter* 13.37 (2017), pp. 6439–6449. DOI: 10.1039/C7SM01084B (cit. on p. 29).

[99] Stefano Buzzaccaro, Jader Colombo, Alberto Parola, and Roberto Piazza. "Critical Depletion". In: *Physical Review Letters* 105.19 (2010), pp. 1–4. DOI: 10.1103/PhysRevLett.105.198301 (cit. on p. 29).

[100] Ignacio A. Martínez, Clemence Devailly, Artyom Petrosyan, and Sergio Ciliberto. "Energy Transfer between Colloids via Critical Interactions". In: *Entropy* 19.2 (2017), p. 77. DOI: 10.3390/e19020077 (cit. on p. 29).

[101] Simon G. Stuij. "Colloidal Design: Building, Bending and Breaking". Amsterdam: Universiteit van Amsterdam, 2020. 166 pp. (cit. on p. 29).

[102] Jeroen S. van Duijneveldt and Daniel Beysens. "Adsorption on Colloids and Flocculation: The Influence of Salt". In: *The Journal of Chemical Physics* 94.7 (1991), pp. 5222–5225. DOI: 10.1063/1.460526 (cit. on p. 29).

[103] Ursula Nellen, Julian Ditrich, Laurent Helden, Shirish Chodankar, Kim Nygrd, J. Friso van der Veen, and Clemens Bechinger. "Salt-Induced Changes of Colloidal Interactions in Critical Mixtures". In: *Soft Matter* 7.11 (2011), pp. 5360–5364. DOI: 10.1039/C1SM05103B (cit. on p. 29).

[104] Faezeh Pousaneh, Alina Ciach, and Anna Maciołek. "How Ions in Solution Can Change the Sign of the Critical Casimir Potential". In: *Soft Matter* 10.3 (2014), pp. 470–483. DOI: 10.1039/c3sm51972d (cit. on p. 29).

[105] Werner Kunz. *Specific Ion Effects*. World Scientific, 2010. 347 pp. DOI: 10.1142/7261 (cit. on p. 29).

[106] Nadine Schwierz, Dominik Horinek, Uri Sivan, and Roland R. Netz. "Reversed Hofmeister Series—The Rule Rather than the Exception". In: *Current Opinion in Colloid & Interface Science* 23 (2016), pp. 10–18. DOI: 10.1016/j.cocis.2016.04.003 (cit. on p. 29).

[107] Beibei Kang, Huicheng Tang, Zengdian Zhao, and Shasha Song. "Hofmeister Series: Insights of Ion Specificity from Amphiphilic Assembly and Interface Property". In: *ACS Omega* 5.12 (2020), pp. 6229–6239. DOI: 10.1021/acsomega.0c00237 (cit. on p. 29).

[108] Kasimir P. Gregory, Erica J. Wanless, Grant B. Webber, Vincent S. J. Craig, and Alister J. Page. "The Electrostatic Origins of Specific Ion Effects: Quantifying the Hofmeister Series for Anions". In: *Chemical Science* 12.45 (2021), p. 15007. DOI: 10.1039/D1SC03568A (cit. on p. 29).

[109] Gudrun Glende, Astrid S. de Wijn, and Faezeh Pousaneh. "The Vanishing Water/Oil Interface in the Presence of Antagonistic Salt". In: *The Journal of Chemical Physics* 152.12 (2020), p. 124707. DOI: 10.1063/1.5142811 (cit. on p. 30).

[110] Jay W. Grate, Marvin G. Warner, Jonathan W. Pittman, Karl J. Dehoff, Thomas W. Wietsma, Changyong Zhang, and Mart Oostrom. "Silane Modification of Glass and Silica Surfaces to Obtain Equally Oil-Wet Surfaces in Glass-Covered Silicon Micromodel Applications". In: *Water Resources Research* 49.8 (2013), pp. 4724–4729. DOI: 10.1002/wrcr.20367 (cit. on p. 33).

[111] Annina M. Steinbach, Tanja Sandner, Boris Mizaikoff, and Steffen Strehle. "Gas Phase Silanization for Silicon Nanowire Sensors and Other Lab-on-a-Chip Systems". In: *physica status solidi c* 13.4 (2016), pp. 135–141. DOI: 10.1002/pssc.201510211 (cit. on p. 33).

[112] Walid-Madhat Munief, Florian Heib, Felix Hempel, Xiaoling Lu, Miriam Schwartz, Vivek Pachauri, Rolf Hempelmann, Michael Schmitt, and Sven Ingebrandt. "Silane Deposition via Gas-Phase Evaporation and High-Resolution Surface Characterization of the Ultrathin Siloxane Coatings". In: *Langmuir* 34.35 (2018), p. 10217. DOI: 10.1021/acs.langmuir.8b01044 (cit. on p. 33).

[113] Chris L. Kennedy, Daphne Sayasilpi, Peter Schall, and Janne-Mieke Meijer. "Self-Assembly of Colloidal Cube Superstructures with Critical Casimir Attractions". In: *Journal of Physics: Condensed Matter* 34.21 (2022), p. 214005. DOI: 10.1088/1361-648X/ac5866 (cit. on p. 34).

[114] John C. Crocker and David G. Grier. "Methods of Digital Video Microscopy for Colloidal Studies". In: *Journal of Colloid and Interface Science* 179.1 (1996), pp. 298–310. DOI: 10.1006/jcis.1996.0217 (cit. on p. 35).

[115] Casper van der Wel and Daniela J. Kraft. "Automated Tracking of Colloidal Clusters with Sub-Pixel Accuracy and Precision". In: *Journal of Physics: Condensed Matter* 29.4 (2017), p. 044001. DOI: 10.1088/1361-648X/29/4/044001 (cit. on p. 35).

[116] Jean-Yves Tinevez, Nick Perry, Johannes Schindelin, Genevieve Hoopes, Gregory Reynolds, Emmanuel Laplantine, Sebastian Bednarek, Spencer Shorte, and Kevin Eliceiri. "TrackMate: An Open and Extensible Platform for Single-Parti-ļe Tracking". In: *Methods*. Image Processing for Biologists 115 (2017), pp. 80–90. DOI: 10.1016/j.ymeth.2016.09.016 (cit. on p. 35).

[117] Marjolein Bruijning, Marco D. Visser, Caspar A. Hallmann, and Eelke Jongejans. "Trackdem: Automated Particle Tracking to Obtain Population Counts and Size Distributions from Videos in r". In: *Methods in Ecology and Evolution* 9.4 (2018), pp. 965–973. DOI: 10.1111/2041-210X.12975 (cit. on p. 35).

[118] T. Wollmann, C. Ritter, J. N. Dohrke, J.-Y. Lee, R. Bartenschlager, and K. Rohr. "Detnet: Deep Neural Network For Particle Detection In Fluorescence Microscopy Images". In: *2019 IEEE 16th International Symposium on Biomedical Imaging (ISBI 2019)*. 2019, pp. 517–520. DOI: 10.1109/ISBI.2019.8759234 (cit. on p. 35).

[119] Jiahao Liu, Xiaoshuai Huang, Liangyi Chen, Liangyi Chen, Shan Tan, and Shan Tan. "Deep Learning-Enhanced Fluorescence Microscopy via Degeneration Decoupling". In: *Optics Express* 28.10 (2020), pp. 14859–14873. DOI: 10.1364/OE.390121 (cit. on p. 35).

[120] Daniel B. Allan, Thomas Caswell, Nathan C. Keim, Casper M. van der Wel, and Ruben W. Verweij. *Soft-Matter/Trackpy: Trackpy v0.5.0*. Zenodo, 2021. DOI: 10.5281/zenodo.4682814 (cit. on pp. 35, 125).

[121] P.-L. Chau and A. J. Hardwick. "A New Order Parameter for Tetrahedral Configurations". In: *Molecular Physics* 93.3 (1998), pp. 511–518. DOI: 10.1080/002689798169195 (cit. on p. 36).

[122] Songrit Maneewongvatana and David M Mount. "It's Okay to Be Skinny, If Your Friends Are Fat". In: Center for Geometric Computing 4th Annual Workshop on Computational Geometry. Vol. 2. 1999, pp. 1–8. URL: https://www.cs.umd.edu/~mount/Papers/cgc99-smpack.pdf (cit. on p. 38).

[123] Ying Ying Diao and Xiang Yang Liu. "Controlled Colloidal Assembly: Experimental Modeling of General Crystallization and Biomimicking of Structural Color". In: *Advanced Functional Materials* 22.7 (2012), pp. 1354–1375. DOI: 10.1002/adfm.201102288 (cit. on p. 42).

[124] Zhiyong Tang, Nicholas A. Kotov, and Michael Giersig. "Spontaneous Organization of Single CdTe Nanoparticles into Luminescent Nanowires". In: *Science* 297.5579 (2002), pp. 237–240. DOI: 10.1126/science.1072086 (cit. on p. 42).

[125] Yun Liu, Lionel Porcar, Jinhong Chen, Wei-Ren Chen, Peter Falus, Antonio Faraone, Emiliano Fratini, Kunlun Hong, and Piero Baglioni. "Lysozyme Protein Solution with an Intermediate Range Order Structure". In: *The Journal of Physical Chemistry B* 115.22 (2011), pp. 7238–7247. DOI: 10.1021/jp109333c (cit. on p. 42).

[126] Flavio Romano, Eduardo Sanz, and Francesco Sciortino. "Crystallization of Tetrahedral Patchy Particles in Silico". In: *The Journal of Chemical Physics* 134.17 (2011), p. 174502. DOI: 10.1063/1.3578182 (cit. on p. 42).

[127] Rodrigo Soto and Ramin Golestanian. "Self-Assembly of Active Colloidal Molecules with Dynamic Function". In: *Physical Review E* 91.5 (2015), p. 052304. DOI: 10.1103/PhysRevE.91.052304 (cit. on p. 42).

[128] Elizabeth Elacqua, Xiaolong Zheng, Cicely Shillingford, Mingzhu Liu, and Marcus Weck. "Molecular Recognition in the Colloidal World". In: *Accounts of Chemical Research* 50.11 (2017), pp. 2756–2766. DOI: 10.1021/acs.accounts.7b00370 (cit. on p. 42).

[129] Emanuele Marino, Daniel M. Balazs, Ryan W. Crisp, Daniel Hermida-Merino, Maria A. Loi, Thomas E. Kodger, and Peter Schall. "Controlling Superstructure–Property Relationships via Critical Casimir Assembly of Quantum Dots". In: *The Journal of Physical Chemistry C* 123.22 (2019), pp. 13451–13457. DOI: 10.1021/acs.jpcc.9b02033 (cit. on p. 42).

[130] Van Duc Nguyen, Suzanne Faber, Zhibing Hu, Gerard H. Wegdam, and Peter Schall. "Controlling Colloidal Phase Transitions with Critical Casimir Forces". In: *Nature Communications* 4 (2013), p. 1584. DOI: 10.1038/ncomms2597 (cit. on p. 42).

[131] Minh Triet Dang, Ana Vila Verde, Van Duc Nguyen, Peter G. Bolhuis, and Peter Schall. "Temperature-Sensitive Colloidal Phase Behavior Induced by Critical Casimir Forces". In: *The Journal of Chemical Physics* 139.9 (2013), p. 094903. DOI: 10.1063/1.4819896 (cit. on pp. 42, 98).

[132] Sandra J. Veen, Oleg Antoniuk, Bart Weber, Marco A C Potenza, Stefano Mazzoni, Peter Schall, and Gerard H. Wegdam. "Colloidal Aggregation in Microgravity by Critical Casimir Forces". In: *Physical Review Letters* 109.24 (2012). DOI: 10.1103/PhysRevLett.109.248302 (cit. on p. 42).

[133] H. J. Jonas, S. G. Stuij, P. Schall, and P. G. Bolhuis. "A Temperature-Dependent Critical Casimir Patchy Particle Model Benchmarked onto Experiment". In: *The Journal of Chemical Physics* 155.3 (2021), p. 034902. DOI: 10.1063/5.0055012 (cit. on pp. 45, 58, 87, 88, 115, 125).

[134] Francesco Sciortino, Emanuela Bianchi, Jack F. Douglas, and Piero Tartaglia. "Self-Assembly of Patchy Particles into Polymer Chains: A Parameter-Free Comparison between Wertheim Theory and Monte Carlo Simulation". In: *Journal of Chemical Physics* 126.19 (2007). DOI: 10.1063/1.2730797 (cit. on pp. 45, 64, 85, 123).

[135] James B. Hendrickson. "Molecular Geometry. I. Machine Computation of the Common Rings". In: *Journal of the American Chemical Society* 83.22 (1961), pp. 4537–4547. DOI: 10.1021/ja01483a011 (cit. on p. 46).

[136] John E. Kilpatrick, Kenneth S. Pitzer, and Ralph Spitzer. "The Thermodynamics and Molecular Structure of Cyclopentane". In: *Journal of the American Chemical Society* 69.10 (1947), pp. 2483–2488. DOI: 10.1021/ja01202a069 (cit. on p. 48).

[137] R. Poupko, Z. Luz, and H. Zimmermann. "Pseudorotation in Cyclopentane. An Experimental Determination of the Puckering Amplitude by NMR in Oriented Solvents". In: *Journal of the American Chemical Society* 104.20 (1982), pp. 5307–5314. DOI: 10.1021/ja00384a008 (cit. on p. 48).

[138] Esther J. Ocola, Leslie E. Bauman, and Jaan Laane. "Vibrational Spectra and Structure of Cyclopentane and Its Isotopomers". In: *The Journal of Physical Chemistry A* 115.24 (2011), pp. 6531–6542. DOI: 10.1021/jp2032934 (cit. on pp. 48, 49).

[139] Philipp Kowalewski, Hans-Martin Frey, Daniel Infanger, and Samuel Leutwyler. "Probing the Structure, Pseudorotation, and Radial Vibrations of Cyclopentane by Femtosecond Rotational Raman Coherence Spectroscopy". In: *The Journal of Physical Chemistry. A* 119.45 (2015), pp. 11215–11225. DOI: 10.1021/acs.jpca.5b07930 (cit. on p. 48).

[140] D. Cremer and J. A. Pople. "General Definition of Ring Puckering Coordinates". In: *Journal of the American Chemical Society* 97.6 (1975), pp. 1354–1358. DOI: 10.1021/ja00839a011 (cit. on pp. 48, 56).

[141] David W. Flaherty, Alper Uzun, and Enrique Iglesia. "Catalytic Ring Opening of Cycloalkanes on Ir Clusters: Alkyl Substitution Effects on the Structure and Stability of C–C Bond Cleavage Transition States". In: *The Journal of Physical Chemistry C* 119.5 (2015), pp. 2597–2613. DOI: 10.1021/jp511688x (cit. on p. 51).

[142] Hongbin Du, Craig Fairbridge, Hong Yang, and Zbigniew Ring. "The Chemistry of Selective Ring-Opening Catalysts". In: *Applied Catalysis A: General* 294.1 (2005), pp. 1–21. DOI: 10.1016/j.apcata.2005.06.033 (cit. on p. 51).

[143] Zhi-Jian Zhao, Lyudmila V. Moskaleva, and Notker Rösch. "Ring-Opening Reactions of Methylcyclopentane over Metal Catalysts, M = Pt, Rh, Ir, and Pd: A Mechanistic Study from First-Principles Calculations". In: *ACS Catalysis* 3.2 (2013), pp. 196–205. DOI: 10.1021/cs3005924 (cit. on p. 51).

[144] Lyudmila Moskaleva, Cheng-chau Chiu, Alexander Genest, and Notker Rösch. "Transformations of Organic Molecules over Metal Surfaces: Insights from Computational Catalysis". In: *The Chemical Record* 16.5 (2016), pp. 2388–2404. DOI: 10.1002/tcr.201600048 (cit. on p. 51).

[145] Saliha Haddoum, Ioana Fechete, Bertrand Donnio, Francois Garin, Doina Lutic, and Chems Eddine Chitour. "Fe-TUD-1 for the Preferential Rupture of the Substituted CC Bond of Methylcyclopentane (MCP)". In: *Catalysis Communications* 27 (2012), pp. 141–147. DOI: 10.1016/j.catcom.2012.07.009 (cit. on p. 51).

[146] Arthur C. Newton, Ramses Kools, David W.H. Swenson, and Peter G. Bolhuis. "The Opposing Effects of Isotropic and Anisotropic Attraction on Association Kinetics of Proteins and Colloids". In: *Journal of Chemical Physics* 147.15 (2017). DOI: 10.1063/1.5006485 (cit. on p. 53).

[147] T. F. Mohry, A. MacIoek, and S. Dietrich. "Phase Behavior of Colloidal Suspensions with Critical Solvents in Terms of Effective Interactions". In: *Journal of Chemical Physics* 136.22 (2012). DOI: 10.1063/1.4722883 (cit. on p. 60).

[148] Ruohai Guo, Jian Mao, Xu Ming Xie, and Li Tang Yan. "Predictive Supracolloidal Helices from Patchy Particles". In: *Scientific Reports* 4.1 (2014), pp. 1–7. DOI: 10.1038/srep07021 (cit. on p. 60).

[149] Deji Akinwande, Christopher J. Brennan, J. Scott Bunch, Philip Egberts, Jonathan R. Felts, Huajian Gao, Rui Huang, Joon-Seok Kim, Teng Li, Yao Li, Kenneth M. Liechti, Nanshu Lu, Harold S. Park, Evan J. Reed, Peng Wang, Boris I. Yakobson, Teng Zhang, Yong-Wei Zhang, Yao Zhou, and Yong Zhu. "A Review on Mechanics and Mechanical Properties of 2D Materials—Graphene and Beyond". In: *Extreme Mechanics Letters* 13 (2017), pp. 42–77. DOI: 10.1016/j.eml.2017.01.008 (cit. on pp. 70, 102).

[150] Qiang Li, Jun Lu, Prince Gupta, and Min Qiu. "Engineering Optical Absorption in Graphene and Other 2D Materials: Advances and Applications". In: *Advanced Optical Materials* 7.20 (2019), p. 1900595. DOI: 10.1002/adom.201900595 (cit. on p. 70).

[151] Sojung Kang, Donghun Lee, Jonghun Kim, Andrea Capasso, Hee Seong Kang, Jin-Woo Park, Chul-Ho Lee, and Gwan-Hyoung Lee. "2D Semiconducting Materials for Electronic and Optoelectronic Applications: Potential and Challenge". In: *2D Materials* 7.2 (2020), p. 022003. DOI: 10.1088/2053-1583/ab6267 (cit. on p. 70).

[152] Florian Banhart, Jani Kotakoski, and Arkady V. Krasheninnikov. "Structural Defects in Graphene". In: *ACS Nano* 5.1 (2011), pp. 26–41. DOI: 10.1021/nn102598m (cit. on pp. 70, 76).

[153] Lili Liu, Miaoqing Qing, Yibo Wang, and Shimou Chen. "Defects in Graphene: Generation, Healing, and Their Effects on the Properties of Graphene: A Review". In: *Journal of Materials Science & Technology*. A Special Issue on 1D Nanomaterials 31.6 (2015), pp. 599–606. DOI: 10.1016/j.jmst.2014.11.019 (cit. on p. 70).

[154] Gao Yang, Lihua Li, Wing Bun Lee, and Man Cheung Ng. "Structure of Graphene and Its Disorders: A Review". In: *Science and Technology of Advanced Materials* 19.1 (2018), pp. 613–648. DOI: 10.1080/14686996.2018.1494493 (cit. on p. 70).

[155] Dieter M. Herlach, Ina Klassen, Patrick Wette, and Dirk Holland-Moritz. "Colloids as Model Systems for Metals and Alloys: A Case Study of Crystallization". In: *Journal of Physics: Condensed Matter* 22.15 (2010), p. 153101. DOI: 10.1088/0953-8984/22/15/153101 (cit. on p. 70).

[156] Paul A. Gabrys, Leonardo Z. Zornberg, and Robert J. Macfarlane. "Programmable Atom Equivalents: Atomic Crystallization as a Framework for Synthesizing Nanoparticle Superlattices". In: *Small* 15.26 (2019), p. 1805424. DOI: 10.1002/smll.201805424 (cit. on p. 70).

[157] Yu Wang, Yufeng Wang, Xiaolong Zheng, Étienne Ducrot, Jeremy S. Yodh, Marcus Weck, and David J. Pine. "Crystallization of DNA-coated Colloids". In: *Nature Communications* 6.1 (1 2015), p. 7253. DOI: 10.1038/ncomms8253 (cit. on p. 70).

[158] Peter Schall, Itai Cohen, David A. Weitz, and Frans Spaepen. "Visualization of Dislocation Dynamics in Colloidal Crystals". In: *Science* 305.5692 (2004), p. 1944. DOI: 10.1126/science.1102186 (cit. on p. 70).

[159] S. Sacanna, W. T. M. Irvine, P. M. Chaikin, and D. J. Pine. "Lock and Key Colloids". In: *Nature* 464.7288 (7288 2010), pp. 575–578. DOI: 10.1038/nature08906 (cit. on p. 70).

[160] Seung Hyun Kim, Andrew D. Hollingsworth, Stefano Sacanna, Sung Jin Chang, Gaehang Lee, David J. Pine, and Gi Ra Yi. "Synthesis and Assembly of Colloidal Particles with Sticky Dimples". In: *Journal of the American Chemical Society* 134.39 (2012), pp. 16115–16118. DOI: 10.1021/ja305865w (cit. on p. 70).

[161] Daniela J. Kraft, Wessel S. Vlug, Carlos M. van Kats, Alfons van Blaaderen, Arnout Imhof, and Willem K. Kegel. "Self-Assembly of Colloids with Liquid Protrusions". In: *Journal of the American Chemical Society* 131.3 (2009), pp. 1182–1186. DOI: 10.1021/ja8079803 (cit. on p. 70).

[162] P. J. M. Swinkels, S. G. Stuij, Z. Gong, H. Jonas, N. Ruffino, B. van der Linden, P. G. Bolhuis, S. Sacanna, S. Woutersen, and P. Schall. "Revealing Pseudorotation and Ring-Opening Reactions in Colloidal Organic Molecules". In: *Nature Communications* 12.1 (1 2021), p. 2810. DOI: 10.1038/s41467-021-23144-6 (cit. on pp. 70, 78).

[163] Lam Van Nang and Eui-Tae Kim. "Controllable Synthesis of High-Quality Graphene Using Inductively-Coupled Plasma Chemical Vapor Deposition". In: *Journal of The Electrochemical Society* 159.4 (2012), K93. DOI: 10.1149/2.082204jes (cit. on p. 74).

[164] Colin Ophus, Ashivni Shekhawat, Haider Rasool, and Alex Zettl. "Large-Scale Experimental and Theoretical Study of Graphene Grain Boundary Structures". In: *Physical Review B* 92.20 (2015), p. 205402. DOI: 10.1103/PhysRevB.92.205402 (cit. on pp. 75, 78).

[165] Pinshane Y. Huang, Carlos S. Ruiz-Vargas, Arend M. van der Zande, William S. Whitney, Mark P. Levendorf, Joshua W. Kevek, Shivank Garg, Jonathan S. Alden, Caleb J. Hustedt, Ye Zhu, Jiwoong Park, Paul L. McEuen, and David A. Muller. "Grains and Grain Boundaries in Single-Layer Graphene Atomic Patchwork Quilts". In: *Nature* 469.7330 (2011), pp. 389–392. DOI: 10.1038/nature09718 (cit. on p. 74).

[166] Paulo T. Araujo, Mauricio Terrones, and Mildred S. Dresselhaus. "Defects and Impurities in Graphene-like Materials". In: *Materials Today* 15.3 (2012), p. 98. DOI: 10.1016/S1369-7021(12)70045-7 (cit. on p. 74).

[167] Ana Primo, Antonio Franconetti, Monica Magureanu, Nicolae Bogdan Mandache, Cristina Bucur, Cristina Rizescu, Bogdan Cojocaru, Vasile I. Parvulescu, and Hermenegildo Garcia. "Engineering Active Sites on Reduced Graphene Oxide by Hydrogen Plasma Irradiation: Mimicking Bifunctional Metal/Supported Catalysts in Hydrogenation Reactions". In: *Green Chemistry* 20.11 (2018), p. 2611. DOI: 10.1039/C7GC03397D (cit. on p. 76).

[168] Dini Wang, Rui Dai, Xing Zhang, Lei Liu, Houlong Zhuang, Yongfeng Lu, Yan Wang, Yiliang Liao, and Qiong Nian. "Scalable and Controlled Creation of Nanoholes in Graphene by Microwave-Assisted Chemical Etching for Improved Electrochemical Properties". In: *Carbon* 161 (2020), pp. 880–891. DOI: 10.1016/j.carbon.2020.01.076 (cit. on p. 76).

[169] Shihao Su, Xinwei Wang, and Jianming Xue. "Nanopores in Two-Dimensional Materials: Accurate Fabrication". In: *Materials Horizons* 8.5 (2021), pp. 1390–1408. DOI: 10.1039/D0MH01412E (cit. on p. 76).

[170] Tianchao Niu, Miao Zhou, Jialin Zhang, Yuanping Feng, and Wei Chen. "Growth Intermediates for CVD Graphene on Cu(111): Carbon Clusters and Defective Graphene". In: *Journal of the American Chemical Society* 135.22 (2013), p. 8409. DOI: 10.1021/ja403583s (cit. on p. 76).

[171] Qu Chen, Alex W. Robertson, Kuang He, Chuncheng Gong, Euijoon Yoon, Gun-Do Lee, and Jamie H. Warner. "Atomic Level Distributed Strain within Graphene Divacancies from BondRotations". In: *ACS Nano* 9.8 (2015), p. 8599. DOI: 10.1021/acsnano.5b03801 (cit. on pp. 76, 94).

[172] Youngkuk Kim, Jisoon Ihm, Euijoon Yoon, and Gun-Do Lee. "Dynamics and Stability of Divacancy Defects in Graphene". In: *Physical Review B* 84.7 (2011), p. 075445. DOI: 10.1103/PhysRevB.84.075445 (cit. on p. 76).

[173] Alex W. Robertson, Gun-Do Lee, Kuang He, Euijoon Yoon, Angus I. Kirkland, and Jamie H. Warner. "Stability and Dynamics of the Tetravacancy in Graphene". In: *Nano Letters* 14.3 (2014), pp. 1634–1642. DOI: 10.1021/nl500119p (cit. on p. 76).

[174] Qinghong Yuan, Junfeng Gao, Haibo Shu, Jijun Zhao, Xiaoshuang Chen, and Feng Ding. "Magic Carbon Clusters in the Chemical Vapor Deposition Growth ofGraphene". In: *Journal of the American ChemicalSociety* 134.6 (2012), p. 2970. DOI: 10.1021/ja2050875 (cit. on p. 78).

[175] Haoyuan Wang, Hai-Bei Li, Na Lin, Jingjing Wang, Ran Xu, and Xian Zhao. "Morphology Effects of Graphene Seeds on the Quality of Graphene Nucleation: Quantum Chemical Molecular Dynamics Simulations". In: *The Journal of Physical Chemistry C* 125.9 (2021), pp. 5056–5065. DOI: 10.1021/acs.jpcc.0c10749 (cit. on p. 78).

[176] Ashley L. Gibb, Nasim Alem, Jian-Hao Chen, Kristopher J. Erickson, Jim Ciston, Abhay Gautam, Martin Linck, and Alex Zettl. "Atomic Resolution Imaging of Grain Boundary Defects in Monolayer Chemical Vapor Deposition-Grown Hexagonal Boron Nitride". In: *Journal of the American Chemical Society* 135.18 (2013), pp. 6758–6761. DOI: 10.1021/ja400637n (cit. on p. 78).

[177] Çağlar Ö Girit, Jannik C. Meyer, Rolf Erni, Marta D. Rossell, C. Kisielowski, Li Yang, Cheol-Hwan Park, M. F. Crommie, Marvin L. Cohen, Steven G. Louie, and A. Zettl. "Graphene at the Edge: Stability and Dynamics". In: *Science* 323.5922 (2009), pp. 1705–1708. DOI: 10.1126/science.1166999 (cit. on p. 80).

[178] Jincan Zhang, Li Lin, Kaicheng Jia, Luzhao Sun, Hailin Peng, and Zhongfan Liu. "Controlled Growth of Single-Crystal Graphene Films". In: *Advanced Materials* 32.1 (2020), p. 1903266. DOI: 10.1002/adma.201903266 (cit. on p. 81).

[179] Mengqi Zeng, Lingxiang Wang, Jinxin Liu, Tao Zhang, Haifeng Xue, Yao Xiao, Zhihui Qin, and Lei Fu. "Self-Assembly of Graphene Single Crystals with Uniform Size and Orientation: The First 2D Super-Ordered Structure". In: *Journal of the American Chemical Society* 138.25 (2016), pp. 7812–7815. DOI: 10.1021/jacs.6b03208 (cit. on p. 81).

[180] Alex W. Robertson, Barbara Montanari, Kuang He, Christopher S. Allen, Yimin A. Wu, Nicholas M. Harrison, Angus I. Kirkland, and Jamie H. Warner. "Structural Reconstruction of the Graphene Monovacancy". In: *ACS Nano* 7.5 (2013), pp. 4495–4502. DOI: 10.1021/nn401113r (cit. on p. 92).

[181] Jack D. Wadey, Alexander Markevich, Alex Robertson, Jamie Warner, Angus Kirkland, and Elena Besley. "Mechanisms of Monovacancy Diffusion in Graphene". In: *Chemical Physics Letters* 648 (2016), pp. 161–165. DOI: 10.1016/j.cplett.2016.02.005 (cit. on pp. 92, 94).

[182] Jani Kotakoski, Clemens Mangler, and Jannik C. Meyer. "Imaging Atomic-Level Random Walk of a Point Defect in Graphene". In: *Nature Communications* 5.1 (1 2014), p. 3991. DOI: 10.1038/ncomms4991 (cit. on p. 92).

[183] L. Li, S. Reich, and J. Robertson. "Defect Energies of Graphite: Density-functional Calculations". In: *Physical Review B* 72.18 (2005), p. 184109. DOI: 10.1103/PhysRevB.72.184109 (cit. on p. 94).

[184] Esmaeil Zaminpayma, Mohsen Emami Razavi, and Payman Nayebi. "Electronic Properties of Graphene with Single Vacancy and Stone-Wales Defects". In: *Applied Surface Science* 414 (2017), pp. 101–106. DOI: 10.1016/j.apsusc.2017.04.065 (cit. on p. 94).

[185] A. A. El-Barbary, R. H. Telling, C. P. Ewels, M. I. Heggie, and P. R. Briddon. "Structure and Energetics of the Vacancy in Graphite". In: *Physical Review B* 68.14 (2003), p. 144107. DOI: 10.1103/PhysRevB.68.144107 (cit. on p. 94).

[186] Gun-Do Lee, C. Z. Wang, Euijoon Yoon, Nong-Moon Hwang, Doh-Yeon Kim, and K. M. Ho. "Diffusion, Coalescence, and Reconstruction of Vacancy Defects in Graphene Layers". In: *Physical Review Letters* 95.20 (2005), p. 205501. DOI: 10.1103/PhysRevLett.95.205501 (cit. on p. 94).

[187] Zhang Luo and Bing Liu. "Shape-Tunable Colloids from Structured Liquid Droplet Templates". In: *Angewandte Chemie* 130.18 (2018), pp. 5034–5039. DOI: 10.1002/ange.201800587 (cit. on p. 98).

[188] Chunhong Chen, Lei Xie, and Yong Wang. "Recent Advances in the Synthesis and Applications of Anisotropic Carbon and Silica-Based Nanoparticles". In: *Nano Research* 12.6 (2019), pp. 1267–1278. DOI: 10.1007/s12274-019-2324-9 (cit. on p. 98).

[189] D. Zeb Rocklin and Xiaoming Mao. "Self-Assembly of Three-Dimensional Open Structures Using Patchy Colloidal Particles". In: *Soft Matter* 10.38 (2014), p. 7569. DOI: 10.1039/C4SM00587B (cit. on p. 98).

[190] Etienne Duguet, Etienne Ducrot, and Serge Ravaine. "Colloidal Molecules and Colloidal Polymers". In: *Functional Materials from Colloidal Self-Assembly*. John Wiley & Sons, Ltd, 2022, pp. 1–36. DOI: 10.1002/9783527828722.ch1 (cit. on pp. 98, 123).

[191] Ji-Hyeok Huh, Kwangjin Kim, Eunji Im, Jaewon Lee, YongDeok Cho, and Seungwoo Lee. "Exploiting Colloidal Metamaterials for Achieving Unnatural Optical Refractions". In: *Advanced Materials* 32.51 (2020), p. 2001806. DOI: 10.1002/adma.202001806 (cit. on p. 98).

[192] T. A. Nguyen, Arthur C. Newton, Sandra J. Veen, Daniela J. Kraft, Peter G. Bolhuis, and Peter Schall. "Switching Colloidal Superstructures by Critical Casimir Forces". In: *Advanced Materials* 29.34 (2017), pp. 1–6. DOI: 10.1002/adma.201700819 (cit. on p. 98).

[193] Hossein Eslami, Neda Khanjari, and Florian Müller-Plathe. "Self-Assembly Mechanisms of Triblock Janus Particles". In: *Journal of Chemical Theory and Computation* (2019). DOI: 10.1021/acs.jctc.8b00713 (cit. on p. 98).

[194] J. P. K. Doye, A. A. Louis, I.-C. Lin, L. R. Allen, E. G. Noya, A. W. Wilber, H. C. Kok, and R. Lyus. "Controlling Crystallization and Its Absence: Proteins, Colloids and Patchy Models". In: *Physical Chemistry Chemical Physics* 9 (2007), pp. 2197–2205. DOI: 10.1039/b614955c (cit. on pp. 100, 113).

[195] E. G. Noya, C. Vega, J. P. K. Doye, and A. A. Louis. "The Stability of a Crystal with Diamond Structure for Patchy Particles with Tetrahedral Symmetry". In: *Journal of Chemical Physics* 132 (2010), p. 234511. DOI: 10.1063/1.3454907 (cit. on pp. 100, 113).

[196] Qiancheng Zhang, Xiaohu Yang, Peng Li, Guoyou Huang, Shangsheng Feng, Cheng Shen, Bin Han, Xiaohui Zhang, Feng Jin, Feng Xu, and Tian Jian Lu. "Bioinspired Engineering of Honeycomb Structure – Using Nature to Inspire Human Innovation". In: *Progress in Materials Science* 74 (2015), pp. 332–400. DOI: 10.1016/j.pmatsci.2015.05.001 (cit. on p. 102).

[197] U Gasser. "Crystallization in Three- and Two-Dimensional Colloidal Suspensions". In: *Journal of Physics: Condensed Matter* 21.20 (2009), p. 203101. DOI: 10.1088/0953-8984/21/20/203101 (cit. on pp. 105, 110).

[198] Christin Büchner, Philomena Schlexer, Leonid Lichtenstein, Stefanie Stuckenholz, Markus Heyde, and Hans-Joachim Freund. "Topological Investigation of Two-Dimensional Amorphous Materials". In: *Zeitschrift für Physikalische Chemie* 228.4-5 (2014), pp. 587–607. DOI: 10.1515/zpch-2014-0438 (cit. on p. 106).

[199] B. Chen and J. I. Siepmann. "Optimized Monte Carlo Data Analysis". In: *Journal of Physical Chemistry B* 105 (2001), p. 11275. DOI: 10.1103/PhysRevLett.63.1195 (cit. on p. 114).

[200] Christin Büchner, Liwei Liu, Stefanie Stuckenholz, Kristen M. Burson, Leonid Lichtenstein, Markus Heyde, Hong-Jun Gao, and Hans-Joachim Freund. "Building Block Analysis of 2D Amorphous Networks Reveals Medium Range Correlation". In: *Journal of Non-Crystalline Solids* 435 (2016), pp. 40–47. DOI: 10.1016/j.jnoncrysol.2015.12.020 (cit. on pp. 117, 118).

[201] Christiaan Huygens. *Treatise on Light In Which Are Explained the Causes of That Which Occurs in Reflexion, & in Refraction and Particularly In the Strange Refraction of Iceland Crystal*. Trans. by Silvanus P. Thompson. London: MacMillan and Co., Limited, 1912. URL: https://archive.org/details/treatiseonlight031310mbp (cit. on p. 121).

[202] Emiliano Carretti, Massimo Bonini, Luigi Dei, Barbara H. Berrie, Lora V. Angelova, Piero Baglioni, and Richard G. Weiss. "New Frontiers in Materials Science for Art Conservation: Responsive Gels and Beyond". In: *Accounts of Chemical Research* 43.6 (2010), pp. 751–760. DOI: 10.1021/ar900282h (cit. on p. 122).

[203] Létitia Jean, Alex C. Foley, and David J. T. Vaux. "The Physiological and Pathological Implications of the Formation of Hydrogels, with a Specific Focus on Amyloid Polypeptides". In: *Biomolecules* 7.4 (4 2017), p. 70. DOI: 10.3390/biom7040070 (cit. on p. 122).

[204] Jing Cai, James P. Townsend, Tom C. Dodson, Paul A. Heiney, and Alison M. Sweeney. "Eye Patches: Protein Assembly of Index-Gradient Squid Lenses". In: *Science* 357.6351 (2017), pp. 564–569. DOI: 10.1126/science.aal2674 (cit. on p. 122).

[205] Paul J. Flory. *Principles of Polymer Chemistry*. Cornell University Press, 1953. 696 pp. (cit. on pp. 122, 128–130, 136).

[206] Dietrich Stauffer and Amnon Aharony. *Introduction to Percolation Theory*. Rev. 2. ed. digital print. London: Taylor & Francis, 2003. 181 pp. DOI: 10.1201/9781315274386 (cit. on pp. 122, 130).

[207] Peter J. Lu, Emanuela Zaccarelli, Fabio Ciulla, Andrew B. Schofield, Francesco Sciortino, and David A. Weitz. "Gelation of Particles with Short-Range Attraction". In: *Nature* 453.7194 (7194 2008), pp. 499–503. DOI: 10.1038/nature06931 (cit. on p. 122).

[208] Alessio Zaccone, Hua Wu, and Emanuela Del Gado. "Elasticity of Arrested Short-Ranged Attractive Colloids: Homogeneous and Heterogeneous Glasses". In: *Physical Review Letters* 103.20 (2009), p. 208301. DOI: 10.1103/PhysRevLett.103.208301 (cit. on p. 122).

[209] Joep Rouwhorst, Christopher Ness, Simeon Stoyanov, Alessio Zaccone, and Peter Schall. "Nonequilibrium Continuous Phase Transition in Colloidal Gelation with Short-Range Attraction". In: *Nature Communications* 11.1 (1 2020), p. 3558. DOI: 10.1038/s41467-020-17353-8 (cit. on p. 122).

[210] Melissa B. Gordon, Christopher J. Kloxin, and Norman J. Wagner. "The Rheology and Microstructure of an Aging Thermoreversible Colloidal Gel". In: *Journal of Rheology* 61.1 (2017), pp. 23–34. DOI: 10.1122/1.4966039 (cit. on p. 123).

[211] John Russo, Piero Tartaglia, and Francesco Sciortino. "Association of Limited Valence Patchy Particles in Two Dimensions". In: *Soft Matter* 6.17 (2010), p. 4229. DOI: 10.1039/c0sm00091d (cit. on pp. 123, 126, 128, 129).

[212] Daniel de las Heras, José Maria Tavares, and Margarida M. Telo da Gama. "Phase Diagrams of Binary Mixtures of Patchy Colloids with Distinct Numbers of Patches: The Network Fluid Regime". In: *Soft Matter* 7.12 (2011), pp. 5615–5626. DOI: 10.1039/C0SM01493A (cit. on p. 123).

[213] Riccardo Fantoni and Giorgio Pastore. "Wertheim Perturbation Theory: Thermodynamics and Structure of Patchy Colloids". In: *Molecular Physics* 113.17-18 (2015), pp. 2593–2607. DOI: 10.1080/00268976.2015.1061150 (cit. on p. 123).

[214] P. I. C. Teixeira and J. M. Tavares. "Phase Behaviour of Pure and Mixed Patchy Colloids — Theory and Simulation". In: *Current Opinion in Colloid & Interface Science* 30 (2017), pp. 16–24. DOI: 10.1016/j.cocis.2017.03.011 (cit. on p. 123).

[215] Rodrigo Braz Teixeira, Daniel de las Heras, José Maria Tavares, and Margarida M. Telo da Gama. "Phase Behavior of a Binary Mixture of Patchy Colloids: Effect of Particle Size and Gravity". In: *The Journal of Chemical Physics* 155.4 (2021), p. 044903. DOI: 10.1063/5.0056652 (cit. on p. 123).

[216] Nikola A. Dudukovic and Charles F. Zukoski. "Evidence for Equilibrium Gels of Valence-Limited Particles". In: *Soft Matter* 10.39 (2014), pp. 7849–7856. DOI: 10.1039/C4SM01389A (cit. on p. 123).

[217] Ravi Kumar Pujala and H. B. Bohidar. "Slow Dynamics and Equilibrium Gelation in Fractionated Montmorillonite Nanoplatelet Dispersions". In: *Colloid and Polymer Science* 297.7 (2019), pp. 1053–1065. DOI: 10.1007/s00396-019-04507-4 (cit. on p. 123).

[218] Silvia Biffi, Roberto Cerbino, Francesca Bomboi, Elvezia Maria Paraboschi, Rosanna Asselta, Francesco Sciortino, and Tommaso Bellini. "Phase Behavior and Critical Activated Dynamics of Limited-Valence DNA Nanostars". In: *Proceedings of the National Academy of Sciences* 110.39 (2013), pp. 15633–15637. DOI: 10.1073/pnas.1304632110 (cit. on p. 123).

[219] Silvia Biffi, Roberto Cerbino, Giovanni Nava, Francesca Bomboi, Francesco Sciortino, and Tommaso Bellini. "Equilibrium Gels of Low-Valence DNA Nanostars: A Colloidal Model for Strong Glass Formers". In: *Soft Matter* 11.16 (2015), p. 3132. DOI: 10.1039/C4SM02144D (cit. on p. 123).

[220] Dan T. Nguyen and Omar A. Saleh. "Tuning Phase and Aging of DNA Hydrogels through Molecular Design". In: *Soft Matter* 13.32 (2017), pp. 5421–5427. DOI: 10.1039/C7SM00557A (cit. on p. 123).

[221] Enrico Lattuada, Debora Caprara, Roberto Piazza, and Francesco Sciortino. "Spatially Uniform Dynamics in Equilibrium Colloidal Gels". In: *Science Advances* (2021). DOI: 10.1126/sciadv.abk2360 (cit. on p. 123).

[222] M. Muthukumar and H. Henning Winter. "Fractal Dimension of a Crosslinking Polymer at the Gel Point". In: *Macromolecules* 19.4 (1986), pp. 1284–1285. DOI: 10.1021/ma00158a064 (cit. on p. 126).

[223] M. S. Wertheim. “Fluids with Highly Directional Attractive Forces. IV. Equilibrium Polymerization”. In: *Journal of Statistical Physics* 42.3-4 (1986), pp. 477–492. DOI: 10.1007/BF01127722 (cit. on p. 128).

[224] Emanuela Bianchi, Piero Tartaglia, Emilia La Nave, and Francesco Sciortino. “Fully Solvable Equilibrium Self-Assembly Process: Fine-Tuning the Clusters Size and the Connectivity in Patchy Particle Systems”. In: *The Journal of Physical Chemistry B* 111.40 (2007), pp. 11765–11769. DOI: 10.1021/jp074281+ (cit. on p. 128).

[225] Hannah J. Jonas and Peter G. Bolhuis. “Explaining the Anomalous Chain Length Distributions of Divalent Patchy Particles in a Highly Confined Space Using Quasi-2D Wertheim Theory”. *In preparation.* (cit. on pp. 132, 136).

[226] Michael Rubinstein and Ralph H. Colby. *Polymer Physics*. Oxford ; New York: Oxford University Press, 2003. 440 pp. (cit. on p. 133).

[227] Walter G. Chapman, George Jackson, and Keith E. Gubbins. “Phase Equilibria of Associating Fluids: Chain Molecules with Multiple Bonding Sites”. In: *Molecular Physics* 65.5 (1988), pp. 1057–1079. DOI: 10.1080/00268978800101601 (cit. on p. 138).

[228] Francesco Sciortino. “Basic Concepts in Self-Assembly”. In: *Proceedings of the International School of Physics "Enrico Fermi"* 193 (Soft Matter Self-Assembly 2016), pp. 1–17. DOI: 10.3254/978-1-61499-662-0-1 (cit. on p. 138).

[229] Ilse A. van Hees, Piet J. M. Swinkels, Remco G. Fokkink, Aldrik H. Velders, Ilja K. Voets, Jasper van der Gucht, and Marleen Kamperman. “Self-Assembly of Oppositely Charged Polyelectrolyte Block Copolymers Containing Short Thermoresponsive Blocks”. In: *Polymer Chemistry* (2019). DOI: 10.1039/C9PY00250B.

[230] Bartosz Gabryelczyk, Hao Cai, Xiangyan Shi, Yue Sun, Piet J. M. Swinkels, Stefan Salentinig, Konstantin Pervushin, and Ali Miserez. “Hydrogen Bond Guidance and Aromatic Stacking Drive Liquid-Liquid Phase Separation of Intrinsically Disordered Histidine-Rich Peptides”. In: *Nature Communications* 10.1 (2019), pp. 1–12. DOI: 10.1038/s41467-019-13469-8.

Online resources

The following are references to content that can be found online.

[231] *Supplementary Movie 1 of "Revealing Pseudorotation and Ring-Opening Reactions in Colloidal Organic Molecules"*. DOI: 10.1038/s41467-021-23144-6 (cit. on pp. 47, 48).

[232] *Supplementary Movie 2 of "Revealing Pseudorotation and Ring-Opening Reactions in Colloidal Organic Molecules"*. DOI: 10.1038/s41467-021-23144-6 (cit. on p. 48).

[233] *Supplementary Movie 3 of "Revealing Pseudorotation and Ring-Opening Reactions in Colloidal Organic Molecules"*. DOI: 10.1038/s41467-021-23144-6 (cit. on p. 48).

[234] *Supplementary Movie 4 of "Revealing Pseudorotation and Ring-Opening Reactions in Colloidal Organic Molecules"*. DOI: 10.1038/s41467-021-23144-6 (cit. on p. 48).

[235] *Supplementary Movie 5 of "Revealing Pseudorotation and Ring-Opening Reactions in Colloidal Organic Molecules"*. DOI: 10.1038/s41467-021-23144-6 (cit. on p. 51).

[236] *Misaligned Flakes of Colloidal Graphene Merging*. URL: https://youtu.be/4f_m5_10Np4 (cit. on p. 78).

[237] *Evolution of a Colloidal Graphene Polycrystal*. URL: https://youtu.be/M2SVkE1DwZQ (cit. on p. 80).

[238] *Network Formation of Patchy Particles*. URL: https://youtu.be/fONDJDyXA0Y (cit. on p. 125).